NTNU

Norwegian University of
Science and Technology

Nanostructuring of Oxygen Permeable Membranes by Chemical Etching Techniques

Espen Tjønneland Wefring

Chemical Engineering and Biotechnology
Submission date: June 2011
Supervisor: Kjell Wiik, IMTE

Norwegian University of Science and Technology
Department of Materials Science and Engineering

Declaration

I declare that the work described in this Master's thesis has been performed independently and in accordance with the rules and regulations for examinations at the Norwegian University of Science and Technology, NTNU

Espen Tjønneland Wefring

Trondheim, June 28, 2011

Abstract

Mixed ionic electronic conducting ceramic oxides are being investigated for use as membranes for oxygen separation from air and as electrodes in solid oxide fuel cells [1, 2]. Oxygen surface exchange rate is an important parameter controlling the oxygen permeation rate of these membranes [3]. In this work surface structuring by wet chemical etching is investigated as a possible route to improve the surface exchange rate of $La_{0.2}Sr_{0.8}Fe_{0.8}Ta_{0.2}O_{3-\delta}$ (LSFT). Several different etchant solutions have been investigated (HCl, HNO_3, H_2SO_4, $H_2C_2O_4$, $NaHCO_3$, Na_2CO_3 and KOH) and evaluated with respect to etch rate, the resulting surface morphology, selectivity and special effects caused by the etchant or the nature of the sample being etched. The resulting surface structure after etching proved to be very dependent on microstructure, showing both elevated grain boundary and mid grain etching. The mid grain etching was unexpected, and additional experiments were done to investigate the cause of this behaviour. The effect of surface structuring using wet chemical etching was investigated using electrical conductivity relaxation at 800°C and 900°C. This showed that an increase of the specific surface area 3.6 times gave an increase of the chemical surface exchange coefficient about 3.16 times at 800°C. The influence of temperature and partial pressure of oxygen on the effect of surface structuring is discussed based on the obtained results.

LSF-based membranes ($La_{1-x}Sr_xFe_{1-y}M_yO_{3-\delta}$ where M = transition metal cation) show limited stability towards CO_2 containing atmospheres, forming surface layers of $SrCO_3$ [4, 5]. It is suggested that a subsequent removal of this layer by i.e. chemical etching could lead to a fine surface structuring. In this work, exposure of LSFT-samples to CO_2-rich atmospheres was done at 900°C and 1000°C without the formation of such a layer. Reasons for this are discussed and alternate experimental conditions are suggested.

Preface

This master thesis was written at the Department of Materials Science and Engineering at the Norwegian University of Science and Technology during the spring of 2011.

I would first of all thank my main supervisor Professor Kjell Wiik for guidance, support and the opportunity to continue working with membranes after my stay in Holland. Second I want to thank Ph.D.-candidate Ørjan Fossmark Lohne and post. doc. Jonas Gurauskis for all the help, practical advice and input they have shared with me during the last months. I also owe a big thank you to the whole materials science department in KII for maintaining such an inspiring learning environment for us students.

In addition I want to thank the population of KII-231 for all the useful and useless times we had, Jarl Erik Flatøy for many inspirational thoughts about the life after this, my family for helping me to get here and my girlfriend for always being there!

Espen Tjønneland Wefring

Contents

List of Abbreviations

ace	Acetone
AFM	Atomic force microscopy
alk	Alkaline
BSE	Backscattered electrons
brn	Brown
bz	Benzene
CN	Coordination number
col	Colourless
dil	Diluted
ECR	Electrical conductivity relaxation
eth	Ethyl ether
EtOH	Ethanol
i	Insoluble
K, K_{sp}	Equilibrium constants
LSF	$La_{1-x}Sr_xFeO_{3-\delta}$
LSFT	$La_{0.2}Sr_{0.8}Fe_{0.8}Ta_{0.2}O_{3-\delta}$
MIEC	Mixed ionic electronic conducting
oran	Orange
RDS	Rate determining step
reac	Reacts with
RT	Room temperature
s	Soluble
SE	Secondary electrons
SEM	Scanning electron microscopy
sl	Slightly soluble
SOFC	Solid oxide fuel cell
V	Lattice vacancy
viol	Violet
vs	Very soluble
WCE	Wet chemical etching
wh	White
XRD	X-ray diffraction
yel	Yellow

List of Symbols

Symbol	Notation	Unit
a	Slope of a straight line	-
$a_{"specie"}$	Activity of "specie"	-
c_o, c_{of}	Oxygen concentration before and after a change of p_{O_2}	mol dm^{-3}
D_{chem}	Chemical diffusion coefficient	cm^2 s^-1
D_a, D_b	Diffusion constants	cm^2 s^{-1}
d	Lattice plane spacing	m
F	Faradays constant	C mol^{-1}
I_{max}	Maximum ion current after surface modification	mol s^{-1} cm^{-2}
I_s	Ion current without surface modification	mol s^{-1} cm^{-2}
j_{O_2}	Oxygen permeation flux	mL cm^{-2} min^{-1}
j_0	Surface exchange flux of oxygen	mL cm^{-2} min^{-1}
k_{chem}	Chemical surface exchange coefficient	cm s^{-1}
k^f_{chem}	Fundamental chemical surface exchange coefficient	cm s^{-1}
L	Membrane thickness	m
L_c	Characteristic length / thickness	m
L_p	Thickness of porous layer	m
l_x $l_{x'}$, l_y, l_z	ECR-sample dimensions	m
M	Concentration	mol dm^{-3}
$p_{"specie"}$	Partial pressure of "specie"	atm
p_{tot}	Total pressure	atm
R	Universal gas constant	J $mol^{-1}K^{-1}$
S	Solubility	mol dm^{-3}
$\bar{S}$	Arithmetic mean (average)	-
S_a	Surface roughness	nm
S_{pa}	Projected surface area	nm^2
S_{pw}	Pore wall surface area	nm^2
S_{sa}	Specific surface area	nm^2
T	Temperature	K or °C
x	Mole fraction	-
α	Oxygen permeation improvement factor	-
γ	Surface energy	J m^{-2}
δ_0 and δ_∞	Oxygen non-stoich. before and after a change of p_{O_2}	-
θ	Diffraction angle for XRD	°
λ	Wave length	m
μ_{O_2}	Chemical potential of oxygen	J mol^{-1}
σ	Standard deviation	-
σ_{el}	Electrical conductivity	S/cm
σ_{ion}	Ionic conductivity	S/cm
σ_T	Tensile stress	MPa
τ	Flush time	seconds
τ_s	Tortuosity	-
ϕ	Dihedral angle	°
ω	Porosity	%
$\varnothing$	Diameter	m

List of Figures

List of Tables

1 Introduction

Mixed ionic electronic conducting (MIEC) materials have attracted attention amongst scientists for use as oxygen membranes and as electrodes in solid oxide fuel cells (SOFC). The goal of the research is to develop membranes that can separate oxygen from air in a cost efficient way [1, 6]. These membranes can provide an environmentally friendly way to produce large amounts of pure oxygen that subsequently may be utilized as i.e. feed air to industrial combustion processes [2].

Production of syngas is one of the proposed applications for the MIEC oxygen membranes. Syngas is a gas which can be produced by partial oxidation of methane and is utilized to produce methanol and for the Fischer-Tropsch synthesis [7]. Equation 1.1 shows the traditional way to produce syngas.

$$CH_4 + H_2O \rightleftharpoons CO + 3H_2 \quad \Delta H_{800^\circ C} = 225kJ/mol \tag{1.1}$$

Another way is to react methane (CH_4) with pure oxygen as shown in Equation 1.2

$$CH_4 + \frac{1}{2}O_2 \rightleftharpoons CO + 2H_2 \quad \Delta H_{800^\circ C} = -23kJ/mol \tag{1.2}$$

Combining these two processes may be advantageous since the exothermic reaction (Equation 1.2) produces heat that can be utilized to run the endothermic reaction (Equation 1.1) [8]. In many cases a nitrogen free syngas is desired. In the case of the process of Equation 1.2, to meet this requirement, a large amount of nitrogen free oxygen is needed [9]. This is where MIEC oxygen membranes may play an important role.

A sketch of a MIEC oxygen membrane utilized for partial oxidation of methane is shown in Figure 1.1. The air-side of this membrane will have a high p_{O_2} compared to the methane-side. Because of this p_{O_2}-difference there will be a gradient in the chemical potential of oxygen between the two sides of the membrane. Oxygen will because of this diffuse towards the low p_{O_2}-side [2]. Because this potential gradient is the sole driving force for oxygen transport through the membrane, the system can be made very simple and it will not need i.e. electrical wiring to force oxygen through [1].

The oxygen permeation flux through the membrane (j_{O_2}) is governed by the bulk oxygen ion diffusion and the surface exchange of oxygen. The chemical diffusion coefficient, D_{chem}, and the chemical surface exchange coefficient, k_{chem}, can describe these processes. Depending on the thickness of the membrane the permeation is either limited by diffusion or by surface exchange. The permeation through a very thick membrane will normally be limited by the diffusion processes, while a very thin membrane will be limited by surface exchange [3]. From this it is apparent that the highest j_{O_2} is achieved

by a thin membrane with a high surface exchange rate. As the science of producing thin films propagates the resulting membranes are to an increasing extent limited by surface exchange [10]. It is hence important to develop methods to increase the surface exchange rate of MIEC oxygen membranes to accompany these better thin films. The

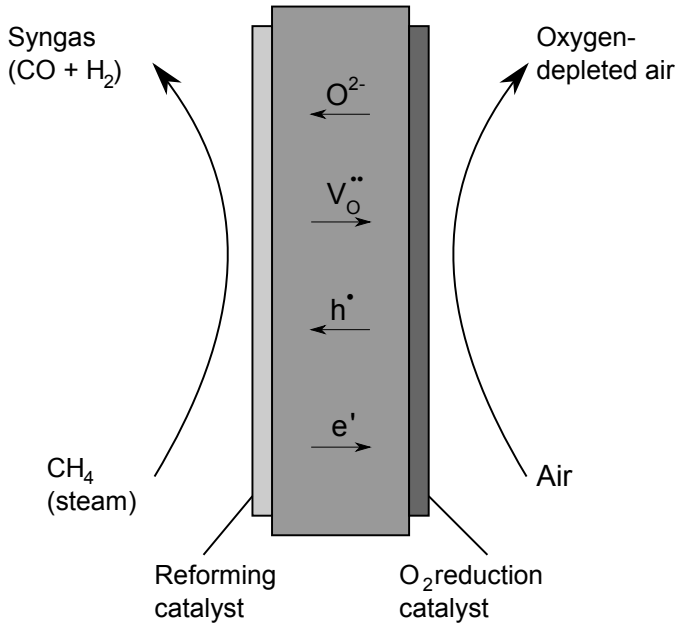

Figure 1.1: Operating pronciple for a MIEC ceramic membrane for partial oxidation of methane. Redrawn from [2]

mechanism for the oxygen surface exchange is not fully determined, but in general it involves an oxygen adsorption step on the high p_{O_2}-side, diffusion of oxygen through the bulk and oxygen desorption on the low p_{O_2}-side [6]. For the oxygen to adsorb it requires an active surface site [11]. The number of these sites available is hence very important for the surface exchange rate. By increasing the area "seen" by the gas surrounding the sample, the specific surface area (S_{sa}) of the membrane, the number of available sites is increased and the oxygen surface exchange rate increases [12].

In this work surface structuring of $La_{0.2}Sr_{0.8}Fe_{0.8}Ta_{0.2}O_{3-\delta}$ (LSFT) membranes by chemical etching is described. The aim is to increase S_{sa}, and by that the apparent k_{chem}, facilitating the production of thinner MIEC-membranes and increased oxygen permeation flux. The structuring will be done by wet chemical etching in aqueous solution and by high temperature exposure of LSFT membranes to CO_2-rich atmospheres. Scanning electron microscopy (SEM), X-ray diffraction (XRD) and atomic force microscopy (AFM) are used to characterize the surface after structuring and electrical conductivity relaxation (ECR) is used to study the effect of surface structuring on k_{chem}.

2 Theory

2.1 Oxygen Transport

The oxygen transport rate through a MIEC perovskite membrane depends on both bulk and surface properties of the membrane. Bulk transport of oxygen is controlled by solid-state diffusion, while the incorporation of oxygen at the surface is governed by the oxygen surface exchange kinetics. Equation 2.1 shows the Wagner equation describing the flux of oxygen through a MIEC-membrane [1].

$$j_{O_2} = -\frac{RT}{4^2F^2L}\int_{lnp'_{O_2}}^{lnp''_{O_2}} \frac{\sigma_{el}\sigma_{ion}}{\sigma_{el}+\sigma_{ion}}\,\mathrm{d}\,lnp_{O_2} \tag{2.1}$$

Here R is the universal gas constant, F is Faradays constant, L is the membrane thickness, p'_{O_2} and p''_{O_2} are the oxygen partial pressures on the high and low p_{O_2}-side of the membrane respectively, and σ_{el} and σ_{ion} are the electronic and ionic conductivity, respectively.

It is apparent from Equation 2.1 that j_{O_2} can be increased by decreasing the thickness of the membrane. This has also been shown experimentally elsewhere [13, 14]. It can be assumed for a thick membrane that j_{O_2} is limited solely by bulk diffusion of oxygen through the membrane. The limiting effect of bulk diffusion will decrease and the oxygen surface exchange rate will become increasingly important as the thickness of the membrane is reduced. The oxygen surface exchange kinetics will be the main limiting factor for j_{O_2} after a sufficient decrease of the thickness. The switch between these two control regimes has been defined as the characteristic thickness, L_c [3].

$$L_c = \frac{D_{chem}}{k_{chem}} \tag{2.2}$$

When $L > L_c$; j_{O_2} is limited by diffusion. When $L < L_c$; j_{O_2} is surface exchange limited and no significant increase of j_{O_2} can be obtained by a further reduction of L.

2.1.1 Oxygen Surface Exchange

The overall goal for the research done on MIEC-membranes for use as oxygen separation membranes is to improve j_{O_2}. Several different material compositions have been investigated for this purpose throughout the years since first suggested many years ago [1, 15]. Oxygen surface exchange is one of the key parameters describing the materials ability to act as an oxygen membrane as denoted in Section 1.

The oxygen surface exchange reaction consists of several steps. The O_2-molecules must

adsorb on the surface, dissociate to O^{2-}-ions, there is a charge transfer step and the O^{2-}-ions must be incorporated into the lattice (into oxygen vacancies) [16]. Several suggestions have been put forth with respect to the reactions for each step, but no definite mechanism has been accepted as entirely correct. Neither is it completely determined which of the steps above is the rate-determining step (RDS). It has been suggested that the RDS is the one where O_2 molecules are dissociated to O^{2-} [12]. The adsorption of oxygen onto the surface has been suggested to be the first step regardless of the overall mechanism and the RDS. This adsorption has been seen to happen on an oxygen vacancy making the oxygen surface exchange rate dependent on the vacancy concentration, p_{O_2}, temperature and doping level of vacancy inducing elements [12, 16]. The mechanism for oxygen surface exchange is relevant with respect to surface structuring because it can give an indication of how effective the surface structuring will be on increasing the surface exchange rate. This is further discussed in Section 2.2.

2.2 Surface Structuring

2.2.1 Earlier Work

Some work has been done earlier to investigate the effect of surface structuring on j_{O_2}. The focus has been on two different methods. One is to cover a dense membrane with a porous layer of the same or similar material. The porous layer may be applied on either the feed side, the permeate side or both sides of the membrane. The other method is to mechanically alter the surface i.e. by using emery paper. Recently a route using chemical etching has also been investigated. These are described below.

Porous Layer Coating Table 2.1 denotes some published results for surface modification of dense oxygen permeable membranes by deposition of porous layers. The improvements of j_{O_2} shown in the table denote the largest improvement reported by the authors of the respective publication. The basis for comparison is an unmodified membrane in all cases. A comparison between the different publications with respect to membrane thickness, gas flow rates, deposition method or other experimental variables has not been emphasized. In Table 2.1, Table 2.3 and Table 2.4, α denotes the permeation improvement factor, meaning the improvement of j_{O_2} with surface modification compared to no modification. Table 2.1 show that the effect of surface modification on j_{O_2} may be significant. It shows that the largest effect comes from modification of the permeate side. It would be expected for MIEC-membranes to observe a decreasing α when increasing temperature. The oxygen permeation will at lower temperatures to a large extent be limited by surface exchange [20]. As the temperature increases, the larger activation energy for surface exchange sees to that the surface exchange rate increases faster than the diffusion rate. When reaching higher temperatures the diffusion rate becomes more and more limiting, hence surface structuring will have less impact

Table 2.1: Reported improvements of j_{O_2} due to porous layer deposition on dense MIEC oxygen membrane discs. FS=feed side, PS=permeate side, F+P=both feed and permeate side coating. α = permeation improvement factor

Membrane material	Porous material	Temp.	α(FS)	α(PS)	α(F+P)	Ref.
$CaTi_{0.8}Fe_{0.2}O_{3-\delta}$	The same	900°C	-	-	1.55	[14]
$CaTi_{0.8}Fe_{0.2}O_{3-\delta}$	The same	950°C	1.13	1.55	1.70	[14]
$SrCo_{0.8}Fe_{0.2}O_{3-\delta}$	The same	772°C	1.24	1.68	2.35	[17]
$SrCo_{0.8}Fe_{0.2}O_{3-\delta}$	The same	870°C	1.1	1.41	1.74	[17]
$La_{0.3}Sr_{0.7}CoO_{3-\delta}$	The same	600°C	-	1.58	-	[18]
$La_{0.3}Sr_{0.7}CoO_{3-\delta}$	The same	750°C	-	1.32	-	[18]
$La_{0.6}Sr_{0.4}Co_{0.2}Fe_{0.8}O_{3-\delta}$	$La_{0.6}Sr_{0.4}CoO_{3-\delta}$	950°C	-	~0	-	[19]
$La_{0.7}Sr_{0.3}Ga_{0.6}Fe_{0.4}O_{3-\delta}$	$La_{0.6}Sr_{0.4}CoO_{3-\delta}$	950°C	-	6.0	-	[19]

on j_{O_2}. The same reasoning can be used for the decreasing effect of surface structuring when increasing the thickness of the dense layer [6]. The limitation of oxygen permeation due to surface exchange decreases relative to the limitation due to diffusion with increasing thickness. Table 2.1 shows that both increase and decrease of structuring effects with temperature is observed in literature. It is not clear why this is and the authors experiencing this temperature dependency deviating from the expected one gave no explanation.

There will exist an optimum thickness of a porous layer covering the dense layer as seen elsewhere, both experimentally [13] and theoretically [21]. The surface exchange rate will start to increase as the thickness of the porous layer (L_p) increases from zero. At some point L_p will become so large that gas transport becomes important and the inner most parts of the porous layer will not be exposed to oxygen rich gas (on the high p_{O_2}-side). On the permeate side (low p_{O_2}-side) the gas released closest to the dense layer will have a long path to go before "released" into the gas flow. The optimum L_p will be just before the gas transport becomes a problem.

Mechanical Abrasion Surface structuring by mechanical abrasion with emery paper has recently been reported in literature [13]. Table 2.2 shows the normalized surface area as a result of mechanical abrasion using different emery papers (increasing number for finer abrasive). The normalized surface area N_{sa} = specific surface area / scanned surface area (projected). Table 2.3 shows the reported improvements of j_{O_2} due to mechanical abrasion of membrane discs. Also here it is evident that the surface structuring of the permeate side is the most effective. The results also confirm the expected trend with decreasing effect of surface structuring with increasing temperature.

Table 2.2: Normalized surface area obtained with different emery paper coarseness. N_{sa} = normalized surface area [13]

Emery paper	N_{sa}
#80	3.19
#1000	2.26
#3000	1.44

Table 2.3: Reported improvements of j_{O_2} due to mechanical abrasion of dense MIEC oxygen membranes. FS=feed side, PS=permeate side, F+P=both feed and permeate side coating. α = permeation improvement factor

Emery paper	Material	Temp.	α(FS)	α(PS)	α(F+P)	Ref.
#3000 vs. #80	$La_{0.1}Sr_{0.9}Co_{0.9}Fe_{0.1}O_{3-\delta}$	700°C	-	-	1.81	[13]
#3000 vs. #80	$La_{0.1}Sr_{0.9}Co_{0.9}Fe_{0.1}O_{3-\delta}$	900°C	-	-	1.59	[13]
$\frac{\text{\#80(FS)\#1000(PS)}}{\text{\#1000(FS)\#80(PS)}}$	$La_{0.1}Sr_{0.9}Co_{0.9}Fe_{0.1}O_{3-\delta}$	900°C	-	-	0.93	[13]
As sintered vs. #80	$Ba_{0.95}La_{0.05}FeO_{3-\delta}$	700°C	1.15	1.6	2.17	[6]
As sintered vs. #80	$Ba_{0.95}La_{0.05}FeO_{3-\delta}$	900°C	1.02	1.2	1.37	[6]

Chemical Etching Some work has been done on improving j_{O_2} of perovskite hollow fibers using chemical etching [20]. Table 2.4 denotes some of the results from these experiments. The method used for etching was to submerge the hollow fiber into an etchant solution, hence both the high and low p_{O_2}-sides of the membrane will be structured. It should be noted that the hollow fibres used to obtain the results in Table 2.4 have radially aligned closed pores in an outer and inner layer covering a dense middle layer. During etching, these pores are opened. This means that some of the contribution to α stems from this extra pore surface area. Regardless of this, it is obvious that chemical etching is an efficient way to improve j_{O_2}. Determining parameters for the results includes etchant concentration and exposure time.

2.2.2 Theoretical Effect of Surface Structuring

The theoretical effect of surface structuring by a porous layer has been investigated elsewhere [22]. Equation 2.3 shows the maximum theoretical ion current through a MIEC-membrane covered with a porous surface layer compared to no coating at all.

Table 2.4: Reported improvements of j_{O_2} due to chemical etching of both inner and outer surface of hollow fibres. α = permeation improvement factor [20]

Material	Etchant / concentration	Exposure time	Temp.	α
$La_{0.6}Sr_{0.4}Co_{0.2}Fe_{0.8}O_{3-\delta}$	H_2SO_4 / 19.6wt%	40 min	800°C	13
$La_{0.6}Sr_{0.4}Co_{0.2}Fe_{0.8}O_{3-\delta}$	H_2SO_4 / 98.0wt%	40 min	800°C	18.6
$La_{0.6}Sr_{0.4}Co_{0.2}Fe_{0.8}O_{3-\delta}$	H_2SO_4 / 98.0wt%	20 min	800°C	14.5
$La_{0.6}Sr_{0.4}Co_{0.2}Fe_{0.8}O_{3-\delta}$	HCl / 18.5wt%	10 min	800°C	4.5
$La_{0.6}Sr_{0.4}Co_{0.2}Fe_{0.8}O_{3-\delta}$	HCl / 37.0wt%	2 min	800°C	6.0
$La_{0.6}Sr_{0.4}Co_{0.2}Fe_{0.8}O_{3-\delta}$	H_2SO_4 / 98.0wt%	40 min	1050°C	4.5
$La_{0.6}Sr_{0.4}Co_{0.2}Fe_{0.8}O_{3-\delta}$	HCl / 37.0wt%	2 min	1050°C	1.5

$$I_{max} = I_s \cdot \xi \tag{2.3}$$

where

$$\xi = \sqrt{\frac{L_c S_{pw}(1-\omega)}{\tau_s}} + \omega \tag{2.4}$$

Here I_s is the ion current without a porous layer, S_{pw} is the pore wall surface area, ω is the porosity and τ_s is the tortuosity. These calculations were done with the limitation of a small pressure gradient and show that for a porous layer, the density, pore size and pore shape is of importance. The modeling done by the authors using Equation 2.4 shows that the maximum increase of ion current, ξ, depends on the nature of the porous layer. At $S_{pw} = 10^3$ the $\xi = 3$ while $S_{pw} = 10^6$ gives $\xi = 77$. In the context of the work described in this report, the important result is that an increased surface area available for the surface exchange reaction increases the maximum ion current through the membrane, and with this the achievable j_{O_2}.

Further work by the same authors showed that taking into account the diffusion of gas inside the porous layer may reduce ξ quite significantly [21]. They show theoretically the existence of an optimum L_p, as was discussed in Section 2.2.1. This thickness decreases with increasing S_{pw}. It further depends on parameters given in Equation 2.4, the concentration and diffusion properties of gas molecules and the tortuosity of the solid phase. The same restrictions do not apply when surface structuring is done by i.e. mechanical abrasion. With mechanical abrasion, i.e. with emery paper #80, the surface will have a variety of trenches more easily accessible for surrounding gas with a possibly much lower τ_s.

2.2.3 The Fundamental vs. Apparent k_{chem}

It is at this point important to note the difference between the fundamental surface exchange coefficient (here denoted k^f_{chem}) and the apparent k_{chem}. Most publications report only k_{chem} regardless of what the specific surface area of the sample is [1, 23–27]. This means that when comparing k_{chem}-values for different materials from different publications, the difference may not stem from the material it self, but rather specific surface area. k^f_{chem} is a material specific parameter which is determined by the material composition, temperature and pressure [12]. This should be constant when doing surface structuring, assuming no changes to the surface chemistry. This is illustrated by the mass balance given in Equation 2.5 [12].

$$k^f_{chem}(\delta_0 - \delta_\infty) = -\frac{S_{pa}}{S_{sa}} L \frac{d\delta}{dt} \tag{2.5}$$

where S_{sa} is the specific surface area of the projected area S_{pa}, δ_0 is the oxygen non-stoichiometry at thermodynamic equilibrium and δ_∞ is the non stoichiometry after re-establishment of thermodynamic equilibrium after an abrupt change of p_{O_2} (as for ECR-experiments, see Section 2.7). This mass balance is valid for a membrane with thickness $L<L_c$ so that oxygen transport is solely limited by surface exchange. The k^f_{chem} in Equation 2.5 is as stated above a constant dependent on material composition, temperature and pressure. Consequently the ratio of S_{pa} to S_{sa} is inverse proportional to $d\delta/dt$. This results states that by increasing S_{sa} it is not k^f_{chem} that increases, but rather the amount of surface reactions.

Throughout this report the term k_{chem} will be used to denote the measured (apparent) surface exchange rate coefficient.

2.3 Surface Analysis

To observe the effect of surface structuring it can be useful to characterize the surface that has been treated. Scanning electron microscopy can give a 2D-depiction of the surface facilitating a qualitative analysis. For a 3D and surface morphology analysis AFM can be used. Analysis of the surface chemistry can to some extent be done using EDS and XRD, as described below

2.3.1 Structure Analysis

Atomic force microscopes are very useful when studying surfaces in 3D at a very small scale. It measures the repulsive forces between a tip mounted on a cantilever spring and the sample surface. The instrument records the deflection of the cantilever spring due to tip-sample surface interactions as the tip is moved across the surface. Usually an optical

setup measures the deflection of the cantilever spring [28]. AFM is a suitable method for surface characterization since it does not require any special sample geometry or preparation nor does it harm the sample. A schematic depiction of an AFM is shown in Figure 2.1. The output from these measurements is a set of X-, Y- and Z-coordinates

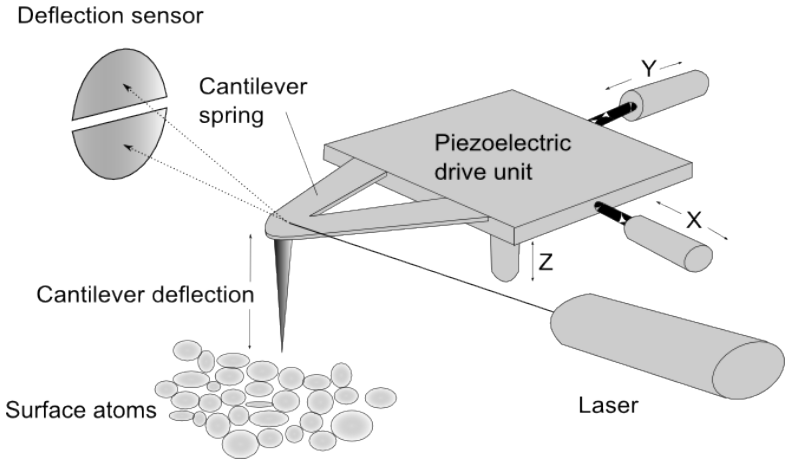

Figure 2.1: Schematic depiction of an AFM, redrawn from [29]

which can be used to plot a 3D view of the surface or i.e. calculate surface roughness (S_a) and specific surface area (S_{sa}) as described in Appendix A. When doing surface structuring it is important to obtain a value for S_{sa} to be able to compare any measured surface parameters with what is seen without surface structuring. Measuring k_{chem} or j_{O_2} before and after surface structuring, and comparing with the increase of S_{sa} leaves a good idea of the surface structuring effectiveness. If the k_{chem} measurements are done in the surface exchange limited regime, k_{chem} should for instance scale directly S_{sa} as described in Section 2.2.3. Any deviations from this scaling could indicate a change of surface composition or, in the case of very rough structuring, gas transport limitations. It could also imply that the oxygen transport is partly limited by diffusion.

2.3.2 Chemical Analysis

EDS is a technique used for quantitative chemical analysis of materials. It utilizes the electron beam of a SEM to scan and quantify the chemical composition close to the surface of a sample. Figure 2.2 shows a schematic depiction of the interaction between the electron beam of a SEM and the sample. Figure 2.2 also shows the relative interaction volume of the three signals relevant for this work, secondary electrons (SE), backscattered electrons (BSE) and characteristic X-rays. It shows that whereas secondary electrons are generated very close to the surface, the characteristic X-rays responsible for the signal used in EDS-analysis are generated much deeper into the sample. The characteristic X-rays are generated when an electron hits an atom in the sample. The electrons

of this atom may be exited to a higher energy state, and when relaxed back to its ground state, a characteristic X-ray is emitted and detected by a detector. The energy of these characteristic X-rays is different depending on what element it came from. Information about the detected signal is further sent to a computer for analysis [30]. EDS is a sim-

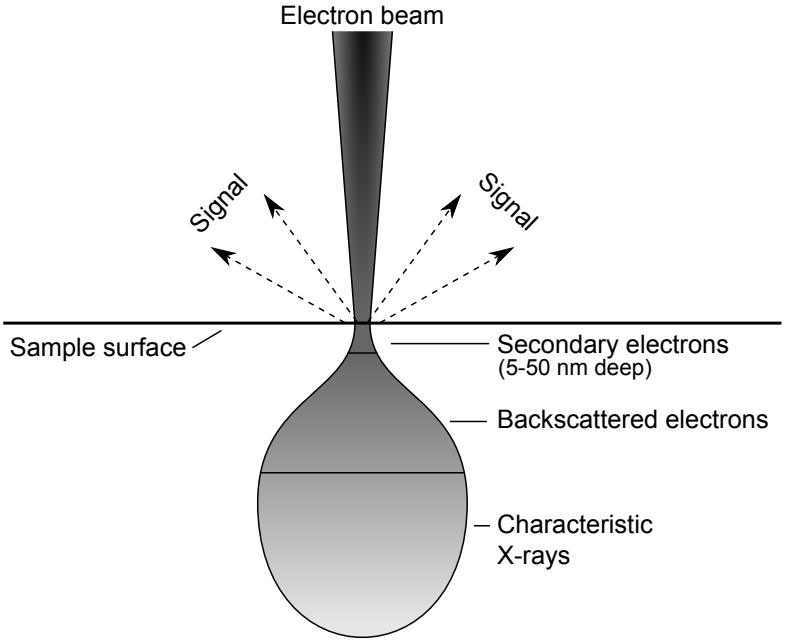

Figure 2.2: Schematic depiction of sample - electron beam interactions in a SEM, inspired by [30]

ple and quick way to gain information about the composition of the sample, but it has its limitations. The penetration depth of the electron beam depends both on the atom number of the elements being studied and the acceleration voltage the electron beam is exposed to [30]. This means that the X-rays emitted from the sample surface may have been generated a distance below the surface. The consequence of this is that the result given by EDS may not give a fully precise composition exactly at the sample surface. An example; imagine if i.e. all the Sr was etched away in a 10 nm surface layer of an LSFT-sample (arbitrary thickness, neglecting any phase changes). If the electron beam generating X-rays penetrate 1 μm into the surface, an EDS-analysis will still show an Sr content. This is because the interaction volume of the beam is deeper into the surface than the 10 nm with Sr depletion. This means that when looking for compositional changes at the surface, an EDS-result may give a hint in which direction the change goes, but the actual change at the surface may be much larger.

XRD is useful when studying the crystal structure of a material. A very simplified and short explanation follows; the technique utilizes X-rays (energy waves) that are

sent towards a sample. The way these waves are scattered when they hit the sample depends on the crystal structure of the sample. The scattering, or diffraction behaviour, is described by Braggs law (Equation 2.6) [31];

$$2d\ sin\theta = n\lambda \tag{2.6}$$

Here d is the spacing between crystal planes, θ is the incident angle of X-rays, n is an integer and λ is the wavelength of the X-rays.

2.4 Chemical Etching

Chemical etching is the process where a substance is exposed to an etchant, and because of this reacts with the etchant and the substance is dissolved from its original form. Chemical etching has many areas of application, one of the most important being patterning of i.e. silicon wafers for the semi-conductor industry [29].

Chemical etching can be done either in a dry or wet environment. Dry etching utilizes ionized gas (plasma) in a vacuum chamber. Wet etching is done by submerging a sample into a liquid, aqueous or organic. The work described in this report will make use of wet chemical etching (WCE). WCE is an isotropic etching technique meaning that it will etch at approximately the same rate in all directions, as is illustrated in Figure 2.3. Also illustrated in Figure 2.3 is the result of pores in the material bulk. As the surface is etched, the etchant will eventually reach a pore. This pore will be filled with etchant solution etching towards the next pore. In this way the etchant may reach far into the bulk of the material, much further than would be expected from the sole surface etch. Etch rate, selectivity and uniformity are three factors that are important when etching [29]. Other factors that may influence the result of etching LSFT include oxide acidity, solubility, precipitation and complexing, all which will be further discussed in the following sections.

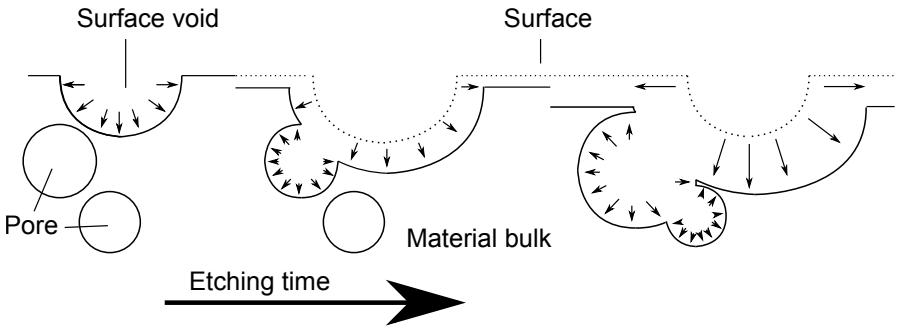

Figure 2.3: Schematic depiction of an isotropic etching process

2.4.1 Etch Rate

The etch rate may be defined as (amount of material removed) / (time elapsed during etching). Depending on the objective of the etching, the amount of material may be a mass (grams), thickness (meters) or volume. When using WCE for surface structuring, the etch rate will determine the exposure time of a sample to the etchant solution. The etch rate is usually proportional to the concentration of the etchant [29]. As etching basically is a chemical reaction the etch rate will be very dependent on temperature. The rate constant for any reaction usually follows an Arrhenius temperature dependency increasing exponentially with increasing temperature [11].

It was seen elsewhere that when etching hollow fibres, the inside tended to etch less than the outside (inner diameter = 0.093 cm). This points out the importance of mass transfer when doing chemical etching [20]. If a uniform surface structure is desired over the entire sample it is important to place the sample in the etchant so that mass transport is not an issue.

2.4.2 Selectivity

Selectivity is another important etch parameter, and can be defined as the ratio of the etch rate towards one specie to the etch rate towards another specie [29]. When etching i.e. a composite, the etchant may be designed/chosen to etch only one of the composite constituents, leaving the other unharmed. In this work it is important that the selectivity is as close to unity as possible meaning that no selectivity is desired towards any specie. This is important for the subsequent use of the etched membrane. A too high selectivity towards one specie may lead to altering of the surface composition and/or an undesirable crystal structure. A cause for this happening may be chemical expansion due to varying radii of LSFT-cations. This is further described in Section 2.5.4.

Acidity is one property that may give a certain selectivity during etching with acidic or alkaline solutions. The substance to be etched in this study is a complex metal oxide and it is important to bear in mind the acidity of the substrate oxides. A basic oxide will normally react more easily with an acidic environment. Since the oxides formed by the LSFT-cations have different acidity, some differences could be expected for the selectivity. This is further treated in Section 2.4.4.

2.4.3 Uniformity

Etch uniformity is a third etch parameter important for this work. It is a measure of how evenly the surface is etched. When surface structuring a membrane for oxygen separation it is important to obtain a surface without features that may create turbulence

or stagnation of the gas flow at certain points, as this could hinder the flow of fresh gas to the surface and decrease the efficiency of the membrane. The etching "short cut" into the material through pores as described in Figure 2.3 may create such stagnation points and deep trenches. As the etchant penetrates far into the material it is expected that mass transport will limit further etching, but the control over surface roughness will nevertheless be limited [20, 29]. The etch uniformity will also differ because of differences in the surface energy associated with different areas of a surface. This is further treated in Section 2.5.2.

2.4.4 Acidity of Oxides

The general trend of acidity of oxides is that s-block elements form basic oxides with increasing basicity going down a group. For p-block elements, the trend is to form acidic oxides with increasing acidity across a period. The acidity of p-block elements also increases with the number of d-electrons and the oxidation state of the transition metal [32].

The primary method of surface structuring in this work is chemical etching using acids and bases. The acidity of the oxide to be etched is hence important. Combined acidity data for the complex LSFT-oxide is not available, but based on the general trends given above, a ranking of the acidity of the individual LSFT-cation oxides will be as follows; SrO < La_2O_3 < Ta_2O_5 < Iron oxides. In an acidic environment, this could lead to a more selective etching of strontium oxides compared to the iron oxides. It would also imply that if the etchant attacks LSFT specifically at an A- or B-site, Sr and Ta are the most vulnerable.

2.4.5 Solubility

Solubility is in a close relationship with etchant selectivity. Solubility data for the complex oxide $La_{0.2}Sr_{0.8}Fe_{0.8}Ta_{0.2}O_{3-\delta}$ is not readily available, but some assumptions can be made based on the individual properties of the LSFT-cation oxides. Table 2.5 gives solubility data for the most common LSFT-cation oxides. It is evident that all the individual oxides are soluble in an acidic environment except SrO and Ta_2O_5. SrO will react with water forming $Sr(OH)_2$ according to Equation 2.7 [34].

$$SrO + H_2O \rightleftharpoons Sr(OH)_2 \tag{2.7}$$

Tantalum oxide is generally a very stable compound, only soluble in HF and other strong acids mixed with HF [34].

Table 2.5: Solubility of oxides and hydroxide from cations in LSFT. Abbreviations; i=insoluble, s=soluble, dil=dilute, reac=reacts with, alk=alkaline solutions, EtOH=ethanol, HF=hydroflouric acid [33]

Name	Formula	Qualitative solubility	Solubility [g/100g H_2O]
Lanthanum oxide	La_2O_3	i H_2O; s dil acid	-
Strontium oxide	SrO	reac H_2O	-
Strontium hydroxide	$Sr(OH)_2$	s H_2O	2.25 (25°C)
Iron(II) oxide	FeO	i H_2O, alk; s acid	-
Iron(II,III) oxide	Fe_3O_4	i H_2O; s acid	-
Iron(III) oxide	Fe_2O_3	i H_2O; s acid	-
Tantalum(V) oxide	Ta_2O_5	i H_2O, EtOH, acid; s HF	-

2.4.6 Precipitation

As mentioned earlier it is desirable to retain the surface chemistry also after etching. In addition to avoiding selective etching it is important to avoid precipitation of new compounds onto the membrane surface during the etching procedure. It is hence important to have control over the type of precipitates that may form. Throughout the work treated in this report, the LSFT-material has been exposed to several different solutions. Most have been acids, and common for all is that they are a combination of an acidic cation (H^+) and a basic anion. Table 2.6 shows possible precipitates combining LSFT-cations with anions introduced by the etchant solutions.

A minimum concentration of cations and anions is required for precipitation to occur. Equation 2.8 gives the general chemical reaction between a solid precipitate (A_aB_b) and its dissolved species;

$$A_aB_b \rightleftharpoons aA^{n+} + bB^{m-} \tag{2.8}$$

If S denotes the solubility, the solubility constant K_{sp} may be calculated as follows;

$$K_{sp} = (aS)^a \cdot (bS)^b \tag{2.9}$$

Here, aS = concentration of cations and bS = concentration of anions. Using data from Table 2.6 it is possible to calculate K_{sp} for each individual precipitate. When a value for K_{sp} for a given compound is calculated Equation 2.9 may be re-arranged so that

$$bS = \left(\frac{K_{sp}}{(aS)^a}\right)^{1/b} \tag{2.10}$$

Table 2.6: Solubility of relevant precipitates from LSFT-cations. Abbreviations; vs=very soluble; s=soluble; sl=slightly soluble; i=insoluble; dil=dilute; reac=reacts with; alk=alkaline solutions; EtOH=ethanol; ace=acetone; bz=benzene; eth=ethyl ether; wh=white; col=colourless; yel=yellow; brn=brown; oran=orange; viol=violet; grn=green. Unless stated otherwise, data taken from [33]

Formula	Colour	Solubility [g/100g H_2O]	T [°C]	Qualitative solubility
$LaCl_3$	wh	95.7	25	
$LaCl_3 \cdot 7H_2O$	wh	95.7	25	s EtOH
$La(OH)_3$	wh	0.00002	20	
$La(NO_3)_3 \cdot 6H_2O$	wh	200	25	vs EtOH; s ace
$La_2(SO_4)_3$				sl H_2O
$La_2(SO_4)_3 \cdot 9H_2O$		2.7	20	i EtOH
$La_2(SO_4)_3 \cdot 8H_2O$	col			sl H_2O
$La_2(CO3)_3 \cdot 8H_2O$	wh			i H_2O; s dil acid
$SrCl_2$	wh	54.7	25	
$SrCl_2 \cdot 6H_2O$	col	54.7	25	s EtOH
$SrCO_3$	wh	0.00034	20	s dil acid
$Sr(OH)_2$	col	2.25	25	
$Sr(NO_3)_2$	wh	80.2	25	sl EtOH, ace
$Sr(NO_2)_2$	wh-yel	72.1	30	s H_2O
$SrC_2O_4 \cdot H_2O$		0.00005	20	sl dil acid
$SrSO_4$	wh	0.0135	25	i EtOH; sl acid
$Fe_2(C_2O_4)_3$	yel			s H_2O, acid; i alk
$FeC_2O_4 \cdot 2H_2O$	yel	0.078	25	s acid
$Fe(OH)_3$	yel		25	i H_2O [35]
$FeCO_3$	gray-brn	0.000062	20	
$Fe(TaO_3)_2$	brn			
FeO(OH)	red-brn			i H_2O; s acid
$FeCl_2$	wh	65	25	vs EtOH, ace; sl bz
$FeCl_2 \cdot 2H_2O$	wh-grn	65	25	
$FeCl_2 \cdot 4H_2O$	grn	65	25	s EtOH
$FeCl_3$	grn	91.2	25	s EtOH, eth, ace
$FeCl_3 \cdot 6H_2O$	yel-oran	91.2	25	s EtOH, eth, ace
$Fe(OH)_2$	wh-grn	0.000052	20	
$Fe(NO_3)_2$	grn	87.5	25	
$Fe(NO_3)_3$		82.5	20	
$Fe(NO_3)_2 \cdot 6H_2O$	grn	87.5	25	
$Fe(NO_3)_3 \cdot 6H_2O$	viol	82.5	20	
$Fe(NO_3)_3 \cdot 9H_2O$	viol-gray	82.5	20	vs EtOH, ace
$FeSO_4$	wh	29.5	25	
$Fe_2(SO_4)_3$	gray-wh	440	20	sl EtOH; i ace
$FeSO_4 \cdot 7H_2O$	blue-grn	29.5	25	i EtOH
$FeSO_4 \cdot H_2O$	wh-yel	29.5	25	
$Fe_2(SO_4)_3 \cdot 9H_2O$	yel	440	20	
$TaCl_5$	yel-wh			reac H_2O; s EtOH

bS in Equation 2.10 will then give the lowest anion concentration needed to get precipitation with a given cation concentration, aS. If the cation concentration is known, or can be estimated from sample size and etchant volume, the risk of precipitation can be controlled. This data can also be used for determining the sample size and corresponding etchant volume that should be used during etching.

2.4.7 Complexing

Wet chemical etching of LSFT leads to dissolution of the oxide releasing metal cations. These in combination with either the water molecules of the solution or the anions introduced by the etchant may form a complex. Complexation is the reaction where a positive and negative (ligand) ions bond to form a new ion, the complex. The formation of such complexes may aid the dissolution reaction by removing the dissolved cations and hence pulling the equilibrium towards more dissolution.

There are several complexes that can arise in each etchant solution since there are four cations and at least two anions (OH^- and etchant ligand). Some complexes are shown in Table 2.7 with corresponding colour in aqueous solution. In general nitrate ions are seen as inert [36].

Table 2.7: Colour of metal ions and complex ions in aqueous solution

Complex ion	Colour
$FeCl_4^-$	Yellow [37]
La^{3+}	Colourless [34]
Sr^{2+}	Colourless [34]
Fe^{2+}	Green [34]
$HFeO_2^{2+}$	Green [34]
Fe^{3+}	Colourless [34]
$FeOH^{2+}$	Colourless [34]
$Fe(OH)_2^+$	Colourless [34]

2.5 Sample Characteristics leading to Uneven Etching

2.5.1 Composition and Secondary Phases

LSFT adopts a perovskite crystal structure with the general ideal stoichiometry ABX_3, where A and B are metal cations and for oxides, X = oxygen. The A-site cations are

normally larger than the B-site cations, in LSFT occupied by (La,Sr) and (Fe,Ta) respectively [38, 39]. $La_{0.2}Sr_{0.8}Fe_{0.8}Ta_{0.2}O_{3-\delta}$ can be seen as a mixture of the oxides La_2O_3, SrO and Fe_2O_3 with 20% of the iron sites occupied by Ta. The isothermal ternary phase diagram for the three oxides is given in Figure 2.4. For an A/B-cation ratio (La,Sr/Fe,Ta) equal to unity the composition will be along the bold *b*-line in Figure 2.4 and the perovskite structure will be retained. Moving the A/B-ratio away from unity will give rise to secondary phases. The occurrence of secondary phases may influence the surface morphology if it shows either higher or lower stability towards the etchant solution relative to the primary phase. At the interface between the primary and secondary phase there will, in most cases, be an increased lattice strain because of lattice mismatch or defects [40]. Such stains may lead to higher reactivity and the interface will hence be etched more readily than both the primary and secondary phase. See Section 2.5.4 for more on strain. An earlier investigation of LSF-based membranes ($La_{1-x}Sr_xFe_{1-y}M_yO_{3-\delta}$ where M = transition metal cation) has shown a precipitation of $Sr_{1-x}La_xFe_{12}O_{19}$ due to kinetic demixing [41]. See Section 2.5.3 for more about kinetic demixing.

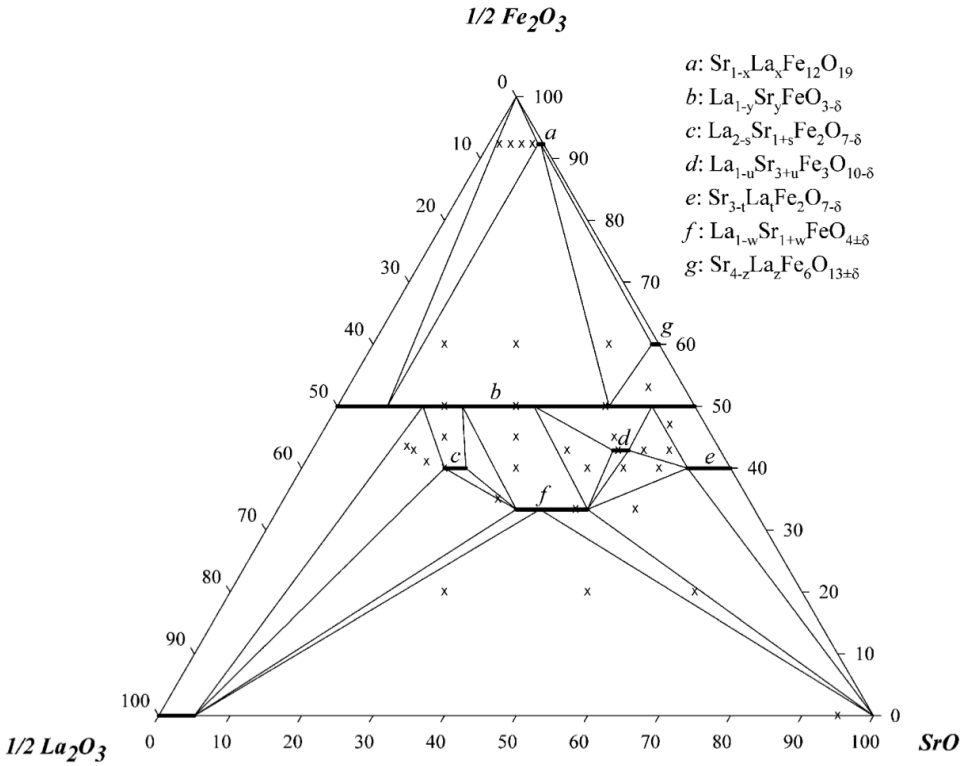

Figure 2.4: Isothermal pseudo-ternary phase diagram of La_2O_3, SrO and Fe_2O_3 at 1100°C. Solid lines correspond to alkemade triangles and bold lines denote solid solution [42]

2.5.2 Surface Activity

The surface energy of a sample is important when exposing it to an etchant solution. The surface energy of a given surface is determined by the number of bonds per unit surface area and the bond strength [32]. A high surface energy corresponds to a reactive surface, hence etching of this surface will be faster than a surface of low surface energy. Grain boundaries are known to have a higher energy than a plain surface [43].

All samples in this work are polished before etching takes place to have a controlled starting point enabling comparison of the different etchants. The 2D surface will hence consist of polished grain bulks and grain boundaries. Figure 2.5 shows a schematic depiction of the interface between two grains and a liquid. Each interface will be subject to a surface energy, γ, with $\gamma^{1,2}$, $\gamma^{1,liq}$ and $\gamma^{2,liq}$ being the interface energy between grain 1 and 2, grain 1 and the liquid, and grain 2 and the liquid, respectively. Assuming $\gamma^{1,liq} = \gamma^{2,liq}$ gives the following equilibrium condition for the three phase interface between grain 1, grain 2 and the liquid [32];

$$\gamma^{1,2} - 2\gamma^{1,liq}\, cos\left(\frac{\phi}{2}\right) = 0 \tag{2.11}$$

Here ϕ is the dihedral angle as defined in Figure 2.5 at equilibrium. If $\phi = 0°$ the liquid will at equilibrium completely separate the two grains, and if $\phi = 180°$ the surface will at equilibrium resemble that seen in Figure 2.5a. Prior to polishing, the sample may be

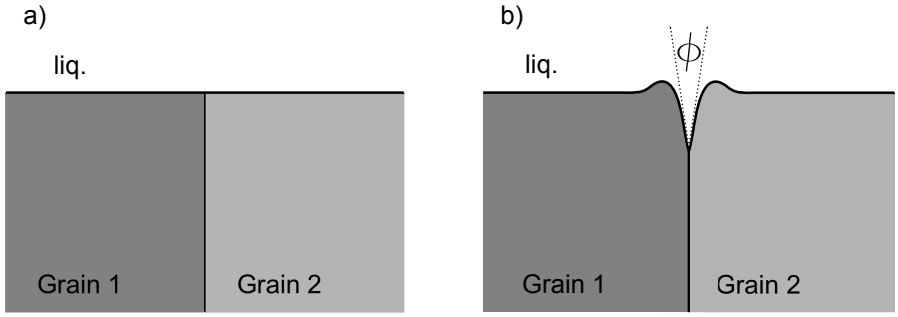

Figure 2.5: Grain boundaries after polishing (a) and after surface relaxation to equilibrium (b). Redrawn from [32]

assumed to be as seen in Figure 2.5a, though $\phi \neq 180°$. This is not the equilibrium case, as illustrated by Figure 2.6, where a polished surface has been thermally etched letting the surface relax to a more thermodynamically favourable state. It is apparent that the non-equilibrium dihedral angle is significantly lowered by thermal etching, moving towards an equilibrium ϕ. The grain boundaries of a polished ceramic sample should when exposed to an etchant solution show enhanced reactivity at the grain boundaries compared to the bulk grain surface also because of the dihedral angle.

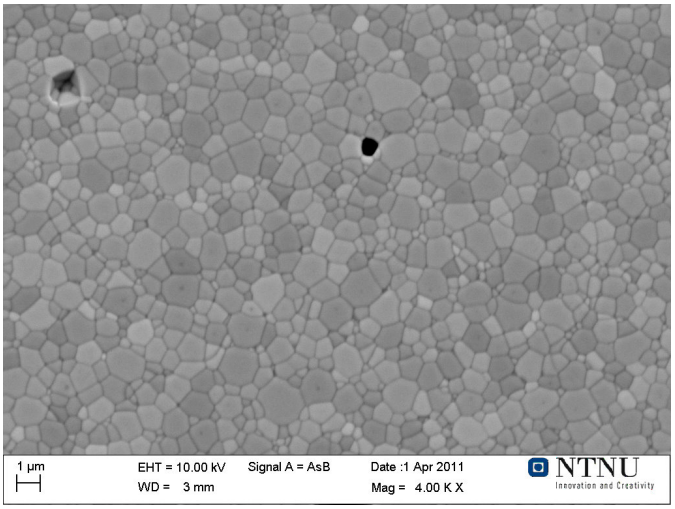

Figure 2.6: Thermally etched surface of LSFT. Ref: [This work]

Surface energy may also be influenced by stresses in the lattice close to the sample surface. An increased stress felt by the surface will increase the surface energy, hence increasing its reactivity [32]. This stress can be caused by chemical expansion, further described in Section 2.5.4.

2.5.3 Kinetic Demixing

Kinetic demixing is a phenomenon that occurs when a material is exposed to a thermodynamic potential gradient. This gradient may be a gradient of temperature, chemical potential, electrical potential or uniaxial pressure [44]. In this work, the relevant gradient is the gradient in chemical potential. The gradients in chemical potential are induced as a consequence of the Gibbs-Duhem relation in Equation 2.12

$$\sum_i (x_i d\mu_i) + x_O d\mu_O = 0 \tag{2.12}$$

where x is the mole fraction of cations i (for LSFT i = La^{3+}, Sr^{2+}, $Fe^{2/3/4+}$ and Ta^{5+}) and μ is the chemical potential of each individual specie. Subscript O represents oxygen. For the system $A_{1-x}B_xO$, steady state demixing can be described by Equation 2.13 [44];

$$\left(\frac{1}{1-x_A} + \frac{D_A}{D_B}\frac{1}{x_A}\right) RT \ln \nabla x_A = \left(\frac{D_A}{D_B} - 1\right)\frac{1}{2} \nabla \mu_{O_2} \tag{2.13}$$

Here D_A and D_B are the diffusion constants for specie A and B, respectively, R is the universal gas constant and T is the absolute temperature. It is apparent from Equation

2.13 that for this two-cation system the D_A/D_B-ratio is decisive for the degree of kinetic demixing and in which direction the cations will diffuse (along or against the oxygen gradient). A large difference between D_A and D_B leads to a high degree of demixing. A large $\nabla\mu_{O_2}$ (thinner materials) will also facilitate a large degree of demixing. Calculations have shown that for a 1 mm thick sample with the slowest D = 10^{-14}, it will take 15 000 years to reach the steady state governed by Equation 2.12 and Equation 2.13, whereas for a 10μm sample it will take only 1.5 years [44]. As the goal of this work is to structure MIEC-membrane surfaces to facilitate thinner membranes in the future, kinetic demixing is important to consider.

In practice, the gradient in oxygen chemical potential stems from the ability of perovskites to cope with large oxygen deficiencies, and still retain the perovskite crystal structure. The oxygen content in oxygen deficient perovskites is significantly lower at high temperatures than at room temperature [1]. This means that when sintering a sample of LSFT, oxygen will leave the lattice upon heating and re-enter upon cooling. It can be expected that oxygen transport back into the sample is significantly faster along grain boundaries than in the grain bulk [45]. Hence, the oxygen transport into the lattice when cooling from sintering temperature will happen along grain boundaries, and then from the grain boundaries into each grain. If the oxygen transport from grain boundaries into grains is too slow, it might lead to an oxygen deficiency in the grain centre relative to the grain boundary. If this oxygen gradient is maintained the chemical potential of

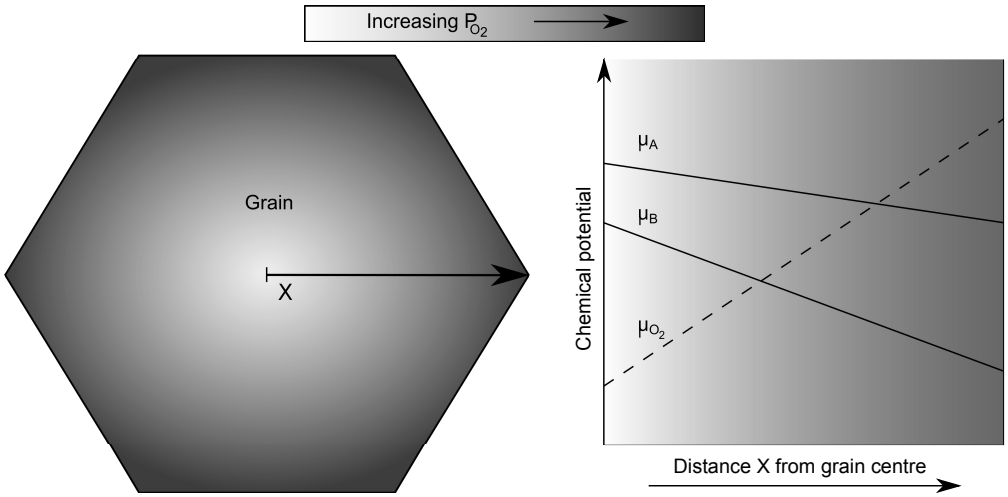

Figure 2.7: Schematic depiction of the varying chemical potential of oxygen for a single bulk grain

the cations in the material will adjust according to Equation 2.13 and Equation 2.16. Whether the cations diffuse towards the middle of the grain or the grain boundary is determined by the relative diffusion coefficients for the different cations [44]. In LSFT,

it would be expected that Fe and Sr are the most mobile cations and that they would diffuse towards the high oxygen potential (Fe more than Sr) [41]. This leaves an oxygen gradient inside each grain as shown in Figure 2.7.

2.5.4 Chemical Expansion

The gradient in oxygen potential discussed in Section 2.5.3 may also lead to tension gradients from the middle of the grain to the grain boundary. This is caused by chemical expansion, which arises from fluctuations in atomic radii and chemical composition [46]. It is well known that the size of ions in a lattice change with the coordination number and valence state [47]. Upon an increase of temperature, oxygen will leave the lattice which again will lead to a weakening of ionic bonds. Cations may be reduced as a consequence of the oxygen leaving, to fulfil the condition of electro neutrality. Equation 2.22 show the interaction oxygen and iron in the sample. When a cation is reduced it increases its size, and combined with the weakened internal bonds, this may cause expansion of the lattice, also called chemical expansion [46].

Investigation of chemical expansion and the stresses it may induce in a membrane has been reported elsewhere [48]. It was shown that across an oxygen membrane exposed to a $\nabla\mu_{O_2}$ there would be a stress gradient with positive tensional stress (σ_T) on the high p_{O_2}-side and a balancing negative σ_T on the low p_{O_2}-side. At some point inside the membrane $\sigma_T = 0$. This is illustrated in Figure 2.8.

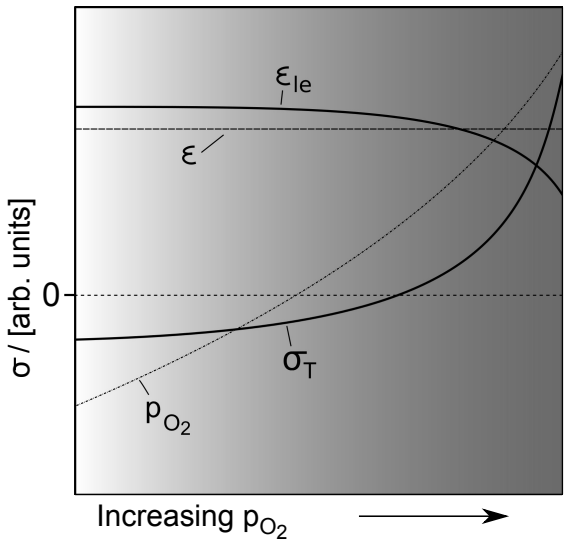

Figure 2.8: Schematic depiction of the stress variation through a membrane exposed to two different p_{O_2}. σ_T = tensile stress, ε = overall strain and ε_{le} = lattice expansion induced strain. Qualitatively based on [48]

2.6 CO_2 Stability

Long-term stability of LSFT is important to make it applicable for use as a gas separation membrane. Several studies of LSF have been done with respect to CO_2-stability [4, 5]. They show that LSF, when exposed to CO_2 at high temperatures, grow carbonate on the surface. This is normally a problem, but here attempts will be made to take advantage of this. Surface structuring will be attempted by deliberately forming carbonates on the surface of the membrane, and subsequently removing them by thermal decomposition or chemical etching.

The two metal ions in LSFT which form carbonates are Fe and Sr. The decomposition temperature of $FeCO_3$ is much lower than the application temperatures for LSFT-membranes, hence growth of $SrCO_3$ is the main issue [49, 50]. $SrCO_3$ will grow according to Equation 2.14.

$$SrO + CO_2 \rightleftharpoons SrCO_3 \tag{2.14}$$

$$K = \frac{a_{SrCO_3}}{a_{SrO} \cdot a_{CO_2}} \tag{2.15}$$

Pure $SrCO_3$-powder has been reported to decompose above 1130°C in CO_2-atmosphere [51]. A simple stability diagram for SrO relative to $SrCO_3$ can be calculated using thermodynamic data (given in Appendix B). Table B.1 shows Gibbs energy of formation, ΔG_f, for the three species in Equation 2.14. Gibbs energy of reaction, ΔG_r, may be calculated using Equation 2.16

$$\Delta G_r = \Delta G_{f,SrCO_3} - \Delta G_{f,CO_2} - \Delta G_{f,SrO} \tag{2.16}$$

from which the equilibrium constant, K, for the formation of $SrCO_3$ can be calculated (Equation 2.17).

$$\Delta G_r = -RTln(K) = \Delta H_r - T \cdot \Delta S_r \tag{2.17}$$

Equation 2.17 takes the assumption of thermodynamic equilibrium. By rearranging the middle and right part of Equation 2.17, differentiating with respect to 1/T and inserting Equation 2.15 for K, Equation 2.18 emerges.

$$\frac{\partial log(a_{CO_2})}{\partial \frac{1}{T}} = \frac{\Delta H}{0.43 \cdot R} \tag{2.18}$$

For Equation 2.18 it is assumed that a_{SrCO_3} and a_{SrO} are constants. Assuming $a_{CO_2} = p_{CO_2}$ makes it possible to plot $\log(p_{CO_2})$ vs. reciprocal temperature. Figure 2.9 shows such a plot where it is assumed that $a_{SrCO_3} = 1$ and a_{SrO} is as denoted for each graph line. For the calculations a_{SrO} must be assumed to have a constant value. One possible assumption is that $a_{SrO} = 0.4$ based solely on the cation mole fraction of Sr in LSFT. The

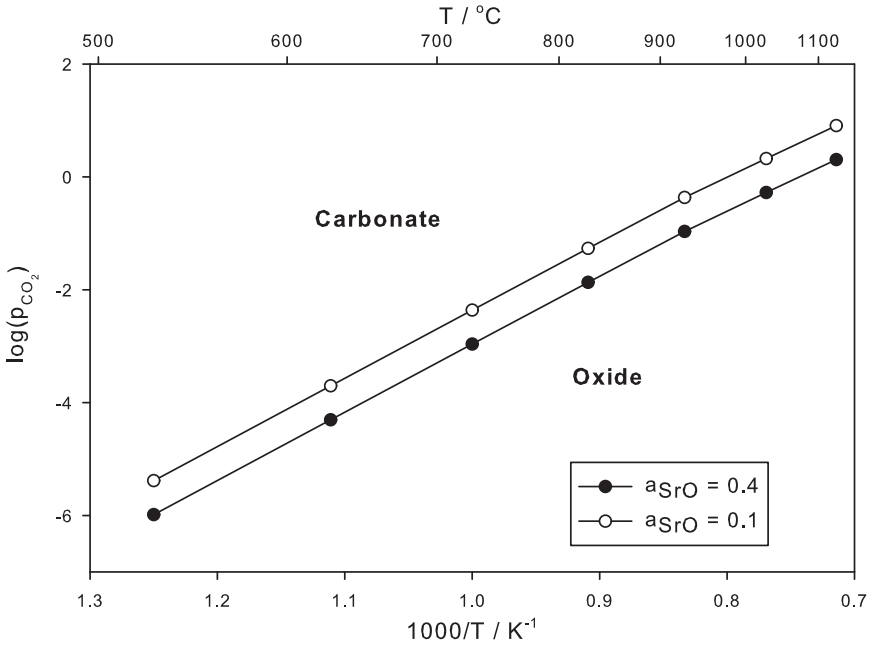

Figure 2.9: Diagram showing the stability region of $SrCO_3$ vs. SrO

fact that SrO is a more alkaline oxide than the other LSFT-metal oxides though implies that a_{SrO} should be lower [52]. Calculations for a_{SrO} = 0.1 is therefore also plotted in Figure 2.9. It shows that in a pure CO_2-atmosphere at atmospheric pressure carbonate will be thermodynamically stable at T<1074°C for a_{SrO} = 0.4 and at T<977°C for a_{SrO} = 0.1.

Because of the limited amount of cation vacancies in LSFT, the cation diffusion is much slower than the oxygen diffusion [53]. As surface strontium reacts with CO_2 forming carbonate, the surface will be depleted with strontium. Previous experiments have shown that carbonate mainly form along grain boundaries [5]. This is reasonable since reactivity is higher along the grain boundaries, as well as the diffusion, so that more strontium is brought to the gas/solid interface relative to what is seen on bulk surfaces [16].

Earlier studies of the carbonate growth have shown an increased growth rate with the presence of H_2O in addition to CO_2. Introducing H_2O makes it necessary to consider the equilibrium shown in Equation 2.19 [5].

$$SrCO_3 + H_2O \rightleftharpoons Sr(OH)_2 + CO_2 \tag{2.19}$$

The stability regions for $SrCO_3$ relative to $Sr(OH)_2$ can be calculated in a similar way to that for $SrCO_3$ vs. SrO. Combining Equation 2.17 with Equation 2.20 gives

$$K' = \frac{a_{CO_2} a_{Sr(OH)_2}}{a_{H_2O} a_{SrCO_3}} \tag{2.20}$$

and setting $a_{gas} = p_{gas}$ and $a_{Sr-species} = 1$ gives Equation 2.21.

$$log(p_{H_2O}) = \frac{\Delta G}{2.3RT} + log(p_{CO_2}) \tag{2.21}$$

Plotting equation 2.21 at given temperatures reveals the stability regions of $SrCO_3$ in humid CO_2-atmosphere relative to $Sr(OH)_2$ (Figure 2.10). The saturation point of H_2O

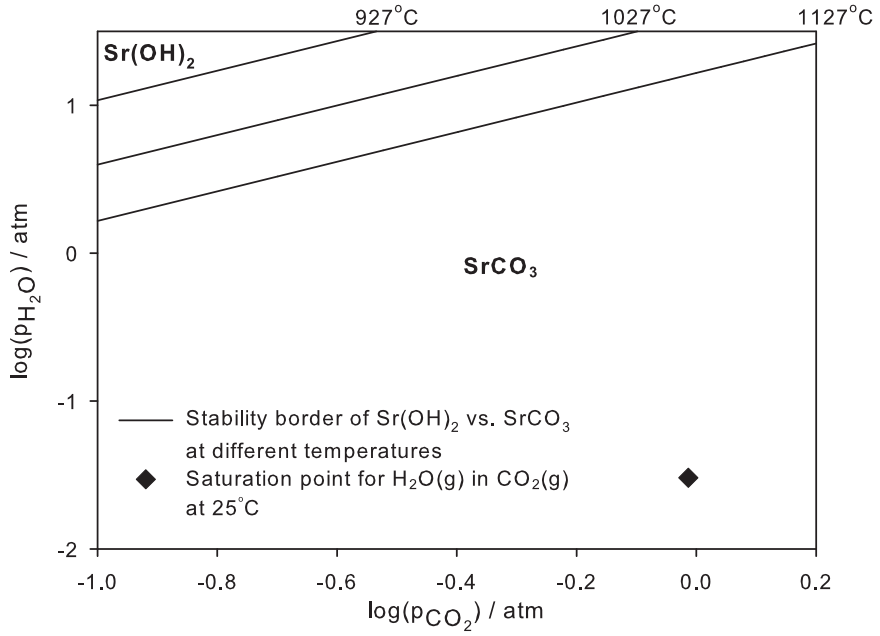

Figure 2.10: Diagram showing the stability region of $SrCO_3$ vs. $Sr(OH)_2$.
◆; Saturation point for water vapour in CO_2 at 25°C

vapour in CO_2 is 0.023 grams per liter of expanded CO_2 at standard temperature and pressure (at atmospheric pressure and 25°C) [54]. This saturation point is noted with a ◆ in Figure 2.10.

2.7 Electrical Conductivity Relaxation

Electrical conductivity relaxation is a very useful technique utilized to study the bulk diffusion and surface exchange kinetics of i.e. MIEC membranes [55, 56]. ECR is a

technique where a sample at isothermal conditions is exposed to a sudden change of a chemical potential in the system it is a part of. This will cause a sudden change to a physical parameter of the sample. The change of this physical parameter is recorded as a function of time while the sample approaches equilibrium. In this work it is the chemical potential of oxygen that is suddenly changed (change of p_{O_2}), and the physical parameter studied is the electrical conductivity. In oxygen deficient perovskites σ_{el} and the σ_{ion} depend on the oxygen non-stoichiometry, which again depends on the chemical potential of oxygen in the surroundings [57].

The reaction between LSFT and oxygen can be described by Equation 2.22;

$$V_O^{\bullet\bullet} + 2Fe_{Fe}^{x} + 1/2O_2(g) \rightleftharpoons O_O^{x} + 2Fe_{Fe}^{\bullet} \tag{2.22}$$

written with Kröger-Vink notation [16, 58]. Here V denotes a vacancy, the subscript denotes the lattice cite being occupied by a vacancy or an atom and $^{\bullet}$ and $'$ denotes a positive and negative charge relative to the normal lattice charge, respectively. The positive charge of Fe at an Fe site is due to the oxidation of Fe with the incorporation of oxygen into the lattice. This electronic defect can be seen as an electron hole (h) and [h] has great influence on σ_{el} [56]. The concentration of oxygen vacancies, $\left[V_O^{\bullet\bullet}\right]$, will increase with decreasing p_{O_2} and decrease with increasing p_{O_2}. Contrary to this σ_{el} will decrease with decreasing p_{O_2} and increase with increasing p_{O_2}. These changes of σ_{el} are recorded as p_{O_2} is changed abruptly, and then fitted to theoretical equations based on Fick's second law (Equation 2.23). It is assumed that the response of the surface exchange flux (j_0) to a sudden change of p_{O_2} is linear. This assumption gives the boundary conditions for Equation 2.23 as shown in Equation 2.24 [59].

$$\frac{\partial c_0}{\partial t} = -\frac{\partial}{\partial z}\left(D_{chem}\frac{\partial c_0}{\partial z}\right) \tag{2.23}$$

$$j_0 = -D_{chem}\frac{\partial c_0}{\partial y} = k_{chem}\left(c_0 - c_{0f}\right) \; at \; y = \pm l_y \tag{2.24}$$

Here, c_0 is the local oxygen concentration, c_{0f} is the new equilibrium oxygen concentration and z and y are dimensional parameters. Equation 2.23 can be solved by assuming

1. an approximately constant value of D_{chem} and k_{chem} during each relaxation

2. a concentration of electronic charge carriers proportional to the oxygen content of the material

3. that the measured conductivity change is assumed to only result from oxygen transport in y and z direction

The solution to Equation 2.23 is given in Equation 2.25 [56]

$$\frac{\sigma_{el,t} - \sigma_{el,0}}{\sigma_{el,\infty} - \sigma_{el,0}} = \frac{M_t}{M_\infty} = 1 - \prod_{i=y,z}\left[\sum_{n=1}^{\infty} A_{n,i} exp\left(-\beta_{n,i} t\right)\right] \tag{2.25}$$

where

$$A_{n,i} = \frac{2L_i^2}{\Gamma_{n,i}^2\left(\Gamma_{n,i}^2 + L_i^2 + L_i\right)} \tag{2.26}$$

$$\beta_{n,i} = \frac{\Gamma_{n,i}^2 D_{chem}}{l_i^2} \tag{2.27}$$

$$\Gamma_{n,i} tan\left(\Gamma_{n,i}\right) = L_i \tag{2.28}$$

and

$$L_i = \frac{k_{chem} l_i}{D_{chem}} \tag{2.29}$$

In the Equation 2.25 - Equation 2.29, $\sigma_{el,t}$, $\sigma_{el,0}$ and $\sigma_{el,\infty}$ denote the electrical conductivity at time t = t, t = 0 and t = ∞ respectively. M_t/M_∞ describe the relative mass change of the sample (with assumption #2 above) and l_i represents the sample dimensions (i = y, z)

The experimental data recorded during ECR is fitted to Equation 2.25. The fitting procedure starts with normalizing the conductivity data to set a defined σ_0 and σ_∞. A typical normalized σ_{el} vs. time plot for a given relaxation is shown in Figure 2.11. Once the fitting is done a value for D_{chem} and k_{chem} is given. The validity of these two values is evaluated with respect to two different criteria.

First Criterion [56] To evaluate if it is possible for the given relaxation run to determine both D_{chem} and k_{chem} it is important to consider which mechanism controls the oxygen transport. This is done by calculating L_i using Equation 2.29. If $L_i < 0.03$, the oxygen transport will be limited by surface exchange, and only k_{chem} can be determined. If $L_i > 30$, the oxygen transport is limited by diffusion, and only D_{chem} can be determined accurately. If $0.03 < L_i < 30$, the oxygen transport is limited by both diffusion and surface exchange, and both D_{chem} and k_{chem} may be determined from the same experiment.

Second Criterion [55] To check if D_{chem} and/or k_{chem} are converging towards a defined value the error in the least square fitting is evaluated. This is illustrated in Figure 2.12 with plots of the least square error as a function of both D_{chem} and k_{chem} for three different relaxation runs. Figure 2.12a shows the case where only D_{chem} converges. A small change of D_{chem} will lead to a relatively large increase of the least square error. A

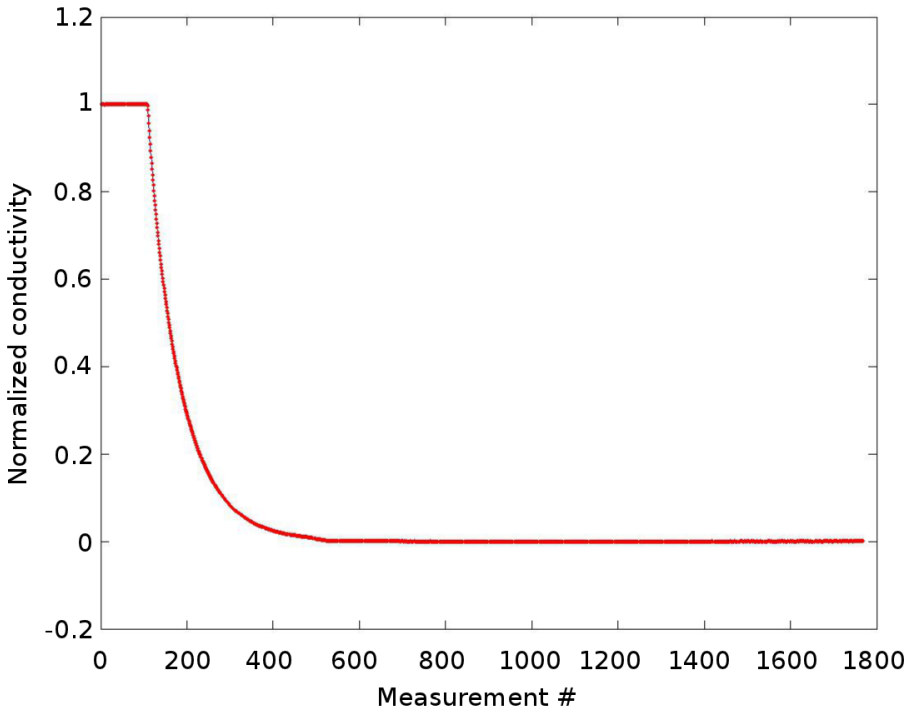

Figure 2.11: Typical normalized σ_{el} curve used as input for fitting experimental data to Equation 2.25. This graph is recorded at 800°C, p_{O_2} step 2% → 6.6%

small change of k_{chem} on the other hand will not increase the error to any large extent, making the value of k_{chem} very uncertain. Figure 2.12b is taken from another relaxation run showing the opposite case. Here, the error will increase significantly with a small change of k_{chem}, while D_{chem} can attain any value without affecting the error. Hence, the relaxation run may only be used to determine k_{chem}. Figure 2.12c shows the middle case where the error will increase significantly if either D_{chem} or k_{chem} changes a little. Although hard to see in this figure, there will be a global minimum defining the set of D_{chem}- and k_{chem}-values giving the best fit. In this case, both the fitted value of D_{chem} and k_{chem} determined from the same relaxation run.

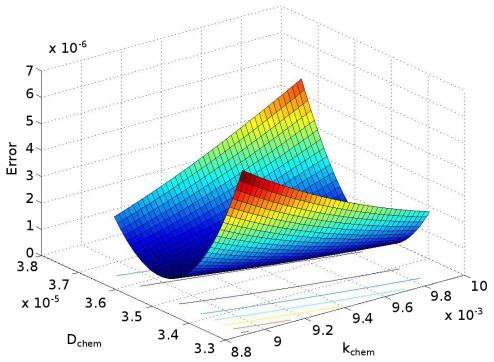

(a) Converging D_{chem}

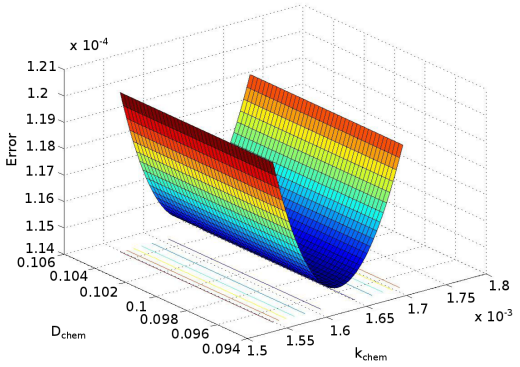

(b) Converging k_{chem}

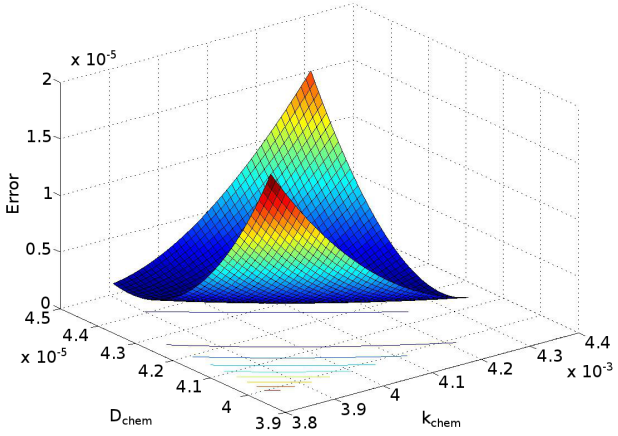

(c) Converging D_{chem} and k_{chem}

Figure 2.12: Plots of errors from the least square fitting of experimental ECR-data

3 Experimental

3.1 Chemicals and Equipment

Table 3.1 lists all chemicals used in this work and Table 3.2 lists the equipment used in this work.

Table 3.1: Chemicals used during this work

Chemical compound	Formula	State	Manufacturer	Purity
Hydrochloric acid	HCl	l	Sigma Aldrich	>37%
Nitric acid	HNO_3	l	Sigma Aldrich	>65%
Sulphuric acid	H_2SO_4	l	Merck	95-98%
Potassium hydroxide	KOH	s	Merck	>85%
Sodium carbonate	$Na_2CO_3 \cdot 10H_2O$	s	Merck	99%
Sodium bicarbonate	$NaHCO_3$	s	Merck	99%
Oxalic acid	$H_2C_2O_4 \cdot 2H_2O$	s	Fluka	>99.5%
Carbon dioxide	CO_2	g	Yara Praxair AS	5.0 Ultra
Oxygen	O_2	g	Yara Praxair AS	5.0 Ultra
Nitrogen	N_2	g	Yara Praxair AS	5.0
Synthetic air	80%N_2 / 20%O_2	g	Yara Praxair AS	5.0 Ultra
Polishing suspension	DiaPro Plan, Dur, NapB and Chem	l/s	Struers	-

Table 3.2: Equipment used during this work

Equipment	Manufacturer and type	Application
Furnaces	Entech, Sweden Entech, Sweden (tubular)	Sintering Altering atmospheres
Polishing	Struers LaboPol-21 Struers SiC-paper FEPA	Coarse grinding of samples
	Struers TegraPol-31 Struers MD polish cloths	Fine polishing of samples
SEM	Hitachi S-3400N Zeiss Supra 55VP	Study of sample surface in 2D
AFM	NanoSurf Easyscan 2	Study of sample surface in 3D
XRD	Siemens D5005 Bruker D8Focus	Study of crystal structure

3.2 Procedures

3.2.1 Preparation of Pellets

Calcined powder (CerPoTech AS, Trondheim, Norway) was pressed into pellets ($\varnothing$= 30 mm, 2 mm green thickness) using a uniaxial press (50 MPa, 2 minutes) followed by cold isostatic pressing (2 kbar, 2 minutes). Stearic acid was used to lubricate the pressing tools for the uniaxial pressing. Sintering of pressed pellets was done at atmospheric conditions with three different heating programs as shown in Table 3.3. The sintered

Table 3.3: Sintering programs used in this work. HR=heating rate, T_{max}=max temperature, $T_{max,t}$=holding time at T_{max}, CR=cooling rate, CCR=change of cooling rate, CR->RT=cooling rate to room temperature

Sintering program	HR [°C/h]	T_{max} [°C]	$T_{max,t}$ [h]	CR 1 [°C/h]	CCR [°C/h]	CR 2 [°C]	CCR [°C]	CR -> RT [°C/h]
A	200	1175	1	5	400	-	-	200
B	200	1350	2	50	850	5	400	200
C	200	1175	1	50	850	5	400	200

pellets were grinded with SiC emery paper and then polished using suspension containing diamonds with consecutive $\varnothing = 9 \rightarrow 3 \rightarrow 1$ μm. The polishing was terminated with a suspension of colloidal silica. The pellets were then cut using diamond saw to obtain pieces with polished surface area ranging from 10 to 20 mm^2. A typical piece of a pellet weighed around 0.1 grams. 96% ethanol was used as cooling liquid during cutting.

3.2.2 Wet Chemical Etching

The different etching experiments conducted are summarized in Table 3.4. It shows which concentrations and exposure times were used for the different etchant solutions. The reduced concentrations were all obtained by mixing the given strong acid with an adequate amount of deionized water. The solids were all dissolved in deionized water. The different etchant solutions were chosen on the basis of observations made during the work, a desire to try varying pH-areas and possible anion effects. Oxalic acid was chosen because a solution of $Ta_2(C_2O_4)_5$ is the source of Ta in the synthesis of LSFT [60]. All wet etch experiments were done at room temperature (RT). The pellet pieces were submerged in beakers filled with the different solutions (typically 5 mL). To ensure best possible exposure of the sample to the etchant solution, care was taken to make sure the surface of interest (usually the polished one) was not facing downwards. The pellet pieces were removed from the etchant after completion of the exposure time, flushed in deionized water and 96% ethanol for quick drying. Any changes to the etchant solution colour or transparency were determined by visual inspection.

Table 3.4: Summary of wet chemical etching experiments

Name	Formula	Conc.	Time
Hydrochloric acid	HCl	12M	1, 10, 30, 60 min, 87 hrs
		6M	1, 5, 10, 15, 20, 30 min
		3M	1, 10, 20, 30, 60 min
		1M	1, 10, 30 min
Nitric acid	HNO_3	14.6M	1, 10, 30 min, 6.5, 23 hrs , 23 d
		7.3M	23 hrs
Sulphuric acid	H_2SO_4	18M	1, 10, 30 min, 6.5 hrs, 23 d
Potassium hydroxide	KOH	20M	1, 10, 30 min, 6.5 hrs, 24 d
		1M	1, 10, 30 min
Sodium carbonate	Na_2CO_3	2.07M	1, 24 hrs
Sodium bicarbonate	$NaHCO_3$	1.23M	1, 24 hrs
Oxalic acid	$H_2C_2O_4$	1.13M	11, 60 min, 23 hrs, 21 d

3.2.3 Carbonate Growth

Polished pellets were exposed to dry and wet CO_2 using the setup seen in Figure 3.1. The figure shows the flow route for experiments using dry CO_2. The dry CO_2-gas was humidified (assumed saturated) with H_2O by rerouting the CO_2-gas flow through the bubbling bottle containing glass beads and H_2O at room temperature. The sample was heated to the maximum holding temp (T_{max}) at 200°C/h. Cooling was done at 50°C/h down to 400°C, and 200°C/h from there to room temperature. Table 3.5 shows the holding times and atmospheres at different T_{max}. The sample chamber was flushed with gas before heating began. The total pressure in the system was held at 1 atm throughout the whole heating cycle by means of the atmospheric outlet. The samples were weighed before and after exposure and characterized using SEM and XRD.

Table 3.5: Conditions for high temperature exposure to CO_2

T_{max}	Holding time, [h]	p_{CO_2}, [atm]	p_{H_2O}, [atm]
900°C	1, 25, 96	1	0
1000°C	25	1	0
1000°C	25	0.97	0.03

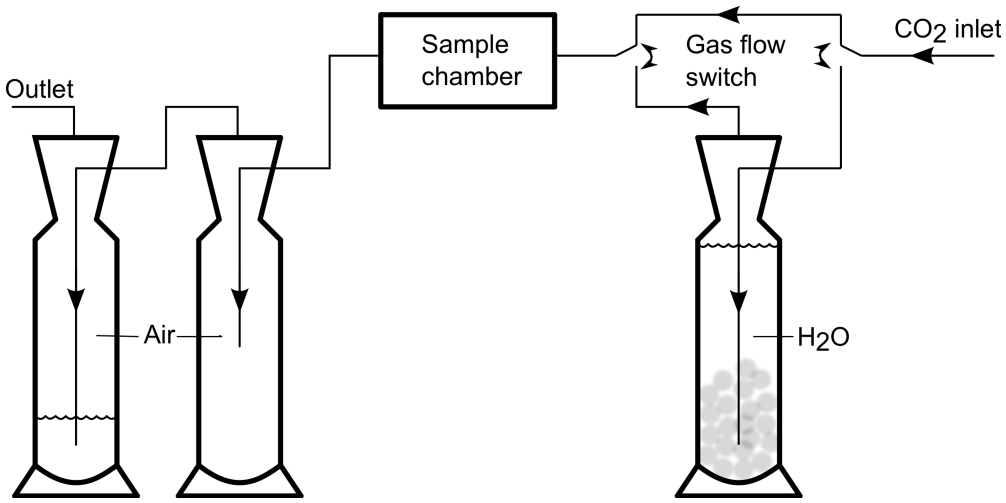

Figure 3.1: Experimental setup for high temperature exposure of LSFT-samples to dry and wet CO_2

3.2.4 Characterization

The sample surfaces were qualitatively analysed before and after the experiments using SEM. Both secondary and backscattered electrons were used. The chemical composition of phases seen was analysed using EDS. No standards were used for this, which means that the EDS-readings are suitable for indicative comparison between similar samples, but they do not necessarily give an exact composition. Quantitative properties of the sample surfaces (S_a and S_{sa}) were obtained using an AFM and the computer software SPIP [61].

The crystal structures of both unetched and etched samples were examined using XRD.

3.2.5 Electrical Conductivity Relaxation

Sample Preparation The sample used for ECR was produced as described in Section 3.2.1 with sintering program C. To ensure a surface as smooth as possible the pellet was first cut, then grinded to the correct dimensions and finally polished. The surface structuring was done by submerging the sample into a mixture of HCl (12M) and deionized H_2O (1:1 volume ratio) for 15 minutes. The sample was put on two thin glass cylinders to lift it 1-2 mm from the beaker bottom removing any mass transfer limitations and ensuring equal etching of all sides of the sample. Table 3.6 shows the sample dimensions measured by an electronic slide caliper. The dimensions in this table refer to the ones denoted in Figure 3.2a. The density of the membrane used for ECR was measured using Archimedes method, according to ISO 5017:1998(E) [62].

Table 3.6: Sample dimensions for ECR-experiments

Length, l_x	19.15 mm.
Width, $2l_y$	2.93 mm.
Thickness, $2l_z$	0.94 mm.
Electrode distance, $l_{x'}$	5 mm.

Relaxation Experiments ECR was used to measure the chemical surface exchange coefficient and the chemical diffusion coefficient for the previously described ECR-sample. Figure 3.2 shows a schematic representation of the experimental setup used for the ECR-experiment. Figure 3.2b shows the sample mounting inside the sample chamber (shown in Figure 3.2c). The sample was heated inside the chamber to 800°C at 180°C/h in a continuous gas flow (250 mL/min, 0.2/0.8 molratio of O_2/N_2). The sample was left at 800°C for several hours to equilibrate. The gas flow was then switched between two different compositions with different p_{O_2} while recording the voltage across the voltage probes seen in Figure 3.2a. The p_{O_2}-steps were as follows (atm); $0.2 \leftrightarrow 0.066 \leftrightarrow 0.02 \leftrightarrow 0.006 \leftrightarrow 0.002$. The volumetric gas flow was increased from 250 mL/min to 500 mL/min when investigating p_{O_2}-steps between 0.02 and 0.002 due to limitations of the experimental setup. After all p_{O_2}-steps were recorded at 800°C the sample was heated to 900°C at 180°C/h and the relaxations were repeated. The temperatures and p_{O_2}-steps were chosen to coincide with previous work done on the same material, but without surface structuring the sample[1]. At least two recordings were done for each p_{O_2}-step at each temperature.

Data Fitting The voltage variations recorded by the ECR-setup was recalculated to σ_{el}. These data were then fitted to Equation 2.25 using a MatLab [63] script written for this purpose by Thomassen [64]. The input to the program was a file containing data from one relaxation, sample dimensions (l_y and l_z) and the reactor flush time, τ;

$$\tau = \frac{280000}{T \cdot flow} \tag{3.1}$$

where T is the absolute temperature and flow the gas flow through the sample chamber in mL/min. The flush time represents the time it takes to completely change the atmosphere inside the sample chamber after a switch from one gas composition to another.

The validity of the fitted values for D_{chem} and k_{chem} were all evaluated against the two criteria given in Section 2.7.

[1] Previous unpublished work done by Ørjan Fossmark Lohne as a part of his PhD-thesis at the Norwegian University of Science and Technology, NTNU

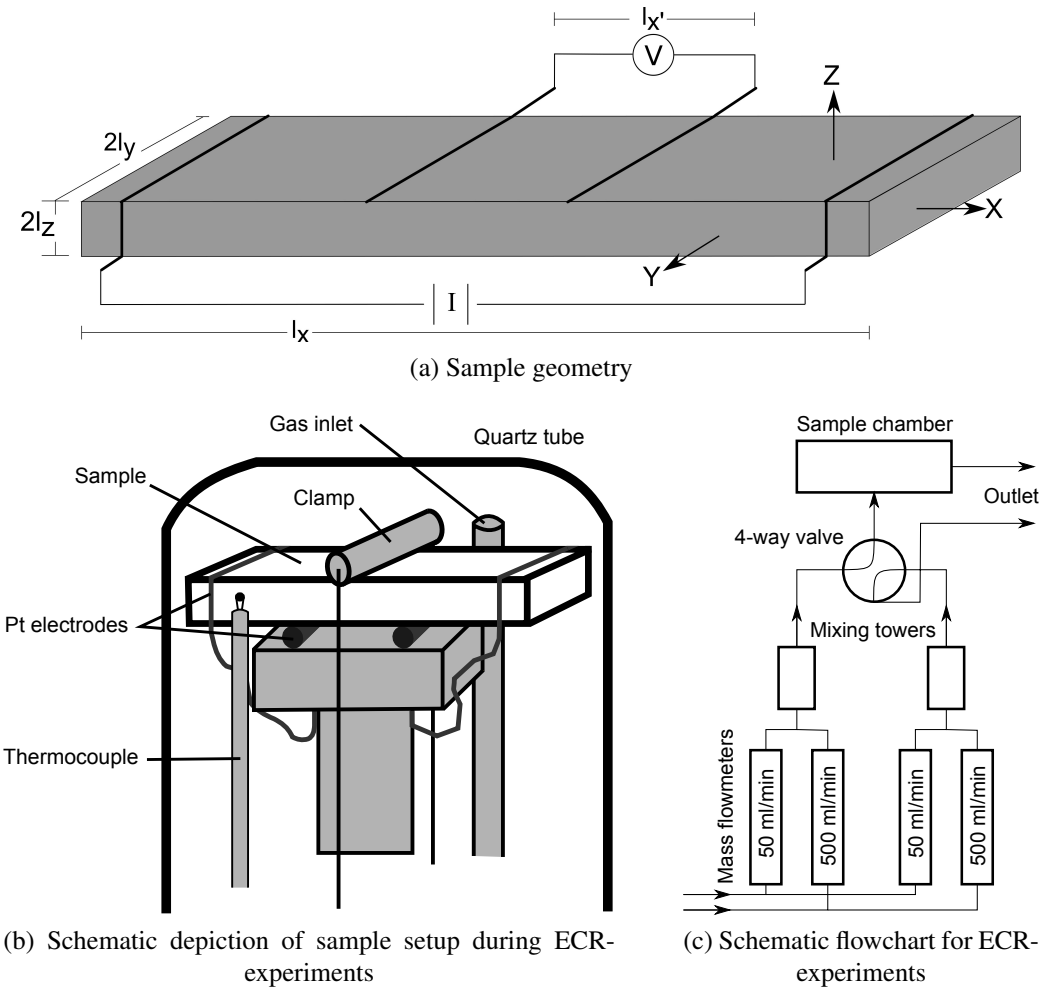

(a) Sample geometry

(b) Schematic depiction of sample setup during ECR-experiments

(c) Schematic flowchart for ECR-experiments

Figure 3.2: Experimental setup for ECR-experiments, redrawn from [59]

4 Results

4.1 Sample Characteristics before Etching

The figures in this section are given as a basis for comparison with figures given later in this report.

Figure 4.1a and Figure 4.1b show the surface grain structure of pellets that were thermally etched after polishing, while Figure 4.1c shows the surface grain structure directly after sintering.

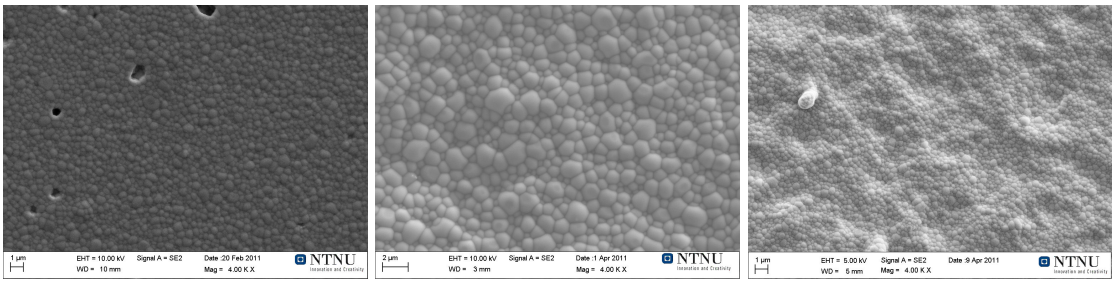

(a) Pellet sintered using sintering program A, polished and thermally etched

(b) Pellet sintered using sintering program B, polished and thermally etched

(c) Pellet sintered using sintering program C, as sintered

Figure 4.1: SEM micrographs showing surface grain structure for pellets from different sintering programs

Figure 4.2a shows a SEM micrograph of an as polished pellet surface and Figure 4.2b shows an AFM image of a similar polished surface (not the exact same sample, but same processing method).

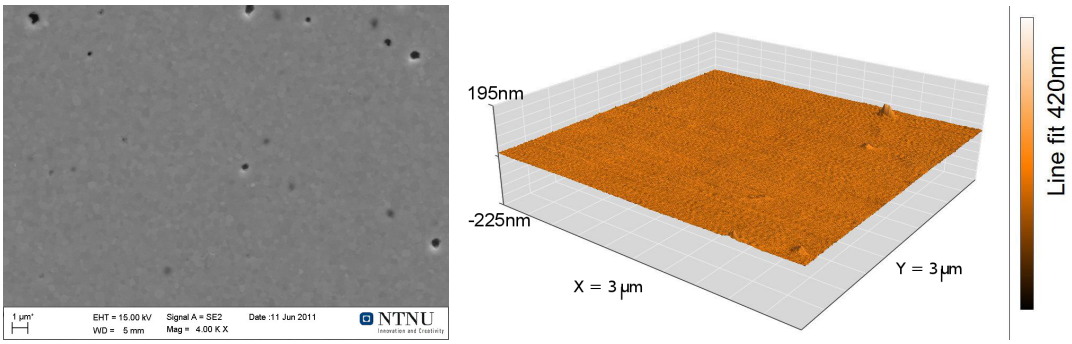

(a) SEM micrograph of a polished pellet surface

(b) AFM picture of a polished pellet surface

Figure 4.2: Polished surfaces characterized by SEM and AFM before etching

Table 4.1 shows the results from quantitative analysis of the polished surface area using data from AFM in SPIP™ [61].

Table 4.1: Surface characteristics for a polished membrane, $N_{sa} = S_{sa} / S_{pa}$

Property	Value	Unit
S_a	1.00165	nm
S_{pa}	$9.00 \cdot 10^6$	nm^2
S_{sa}	$9.87 \cdot 10^6$	nm^2
N_{sa}	1.10	-

4.2 Wet Chemical Etching - Surface Structuring

This section reports the results from the WCE-experiments listed in Table 3.4. Only experiments that showed results are reported. This is relevant in the cases where etching for i.e. 30 minutes did not show any effect. The experiments done in the same solution for shorter times are then left out.

4.2.1 HCl

Close to no etching was observed after exposing a sample to 1M HCl solution for 30 minutes, Figure 4.3.

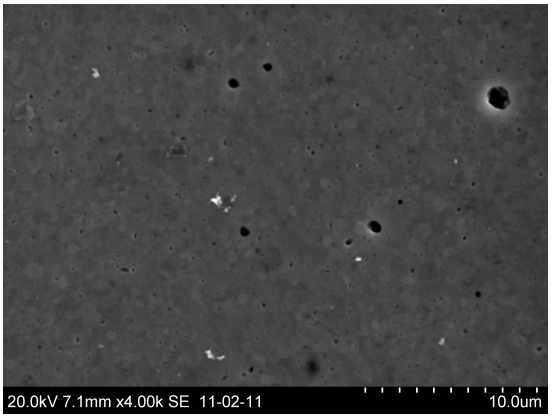

Figure 4.3: Pellet surface etched 30 min in 1M HCl solution

Figure 4.4 and Figure 4.5 show SEM-micrographs of sample surfaces after etching in 3M, 6M, and 12M HCl for various times. It is evident that etchant concentration and

sample exposure time has a great influence on the end result. Little etching was observed after etching with 3M where only small amounts of mid grain etching is visible after 1 and 10 minutes (Figure 4.4a and Figure 4.4b). A hint of grain boundary etching is visible after 20 minutes and apparent after 30 minutes of etching in 3M HCl solution (Figure 4.5a and Figure 4.5b). Etching in the middle of the grains followed by etching of grain boundaries was observed also when etching in 6M HCl-solution, but the etch rate was about twice the one seen with 3M-solutions (Figure 4.4c, Figure 4.4d, Figure 4.5c and Figure 4.5d). Very fast etching was observed when using 12M HCl-solution. The same etch mechanism was observed as for the lower concentrations with mid grain etching and grain boundary etching. The surface after 1 minute in 12M HCl resembles that after 10 minutes in 6M HCl (Figure 4.5d and Figure 4.4e). A very rough surface was observed after etching in 12M HCl for 10 minutes, 30 minutes and 87 hours (Figure 4.4f, Figure 4.5e and Figure 4.5f). It is apparent that the rough surface resulting from this etching is influenced by pores in the sample giving routes for fast penetration into the material. The surface structure remains quite constant after etching for 30 minutes as the same structure was observed after 87 hours. The experiment was aborted after 87 hours since the pellet piece was almost completely dissolved.

The mid grain etching seen in all etching experiments was further investigated on pellets sintered at higher temperatures (sintering program B). These pellets have a significantly larger grain size than the ones used for the previously mentioned experiments with HCl (cf. Figure 4.1a vs. Figure 4.1b). Very little mid grain etching was seen when etching the pellets sintered at higher temperature for a longer time. It is apparent that the etching of grain boundaries is dominating. A more even surface was obtained both when etching at reduced concentrations (Figure 4.6a and Figure 4.6b) and at concentrated HCl-solution (Figure 4.6c and Figure 4.6d). Some of the larger grains show signs of mid grain etching, but not to the extent seen for the previously described samples.

The mid grain etching was also investigated by etching a polished cross section of a sample of sintering program A and B. The result is shown in Figure 4.7. No significant difference could be observed between the etching close to the sample surface (Figure 4.7a and Figure 4.7b) and in the middle of the sample (Figure 4.7c and Figure 4.7d). Figure 4.7e shows the unpolished opposing side of the pellet seen in Figure 4.4d. It shows significantly less mid grain etching compared to the polished side of this sample.

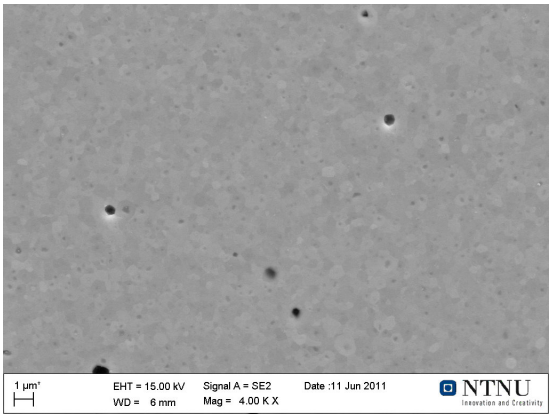

(a) Etched 1 min in 3M HCl

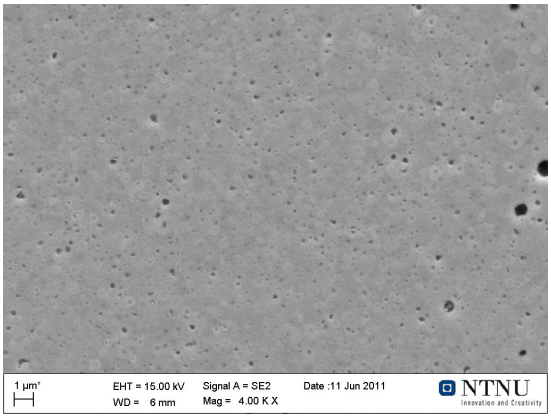

(b) Etched 10 min in 3M HCl

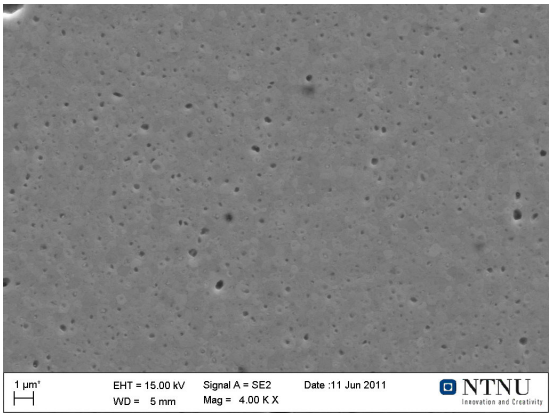

(c) Etched 1 min in 6M HCl

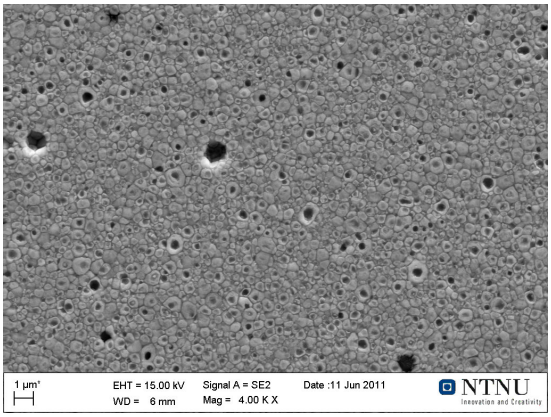

(d) Etched 10 min in 6M HCl

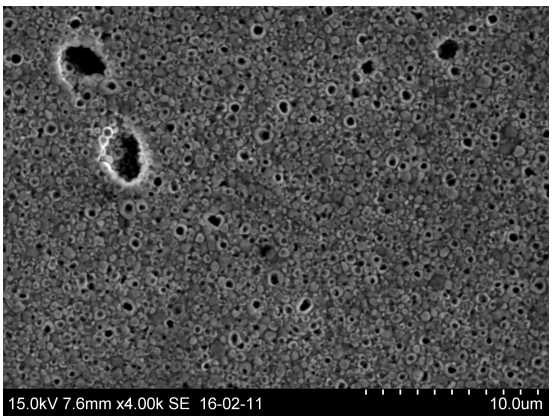

(e) Etched 1 min in 12M HCl

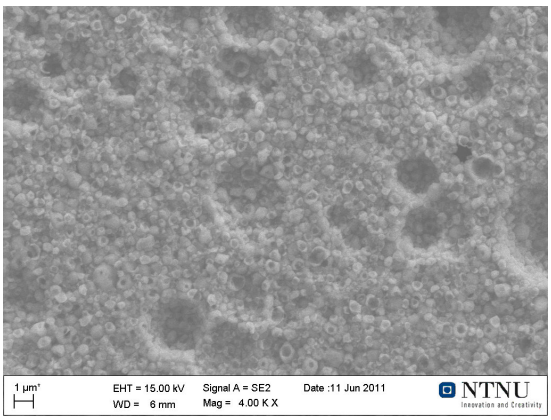

(f) Etched 10 min in 12M HCl

Figure 4.4: SEM micrographs of pellet surfaces after room temperature exposure to 3M, 6M and 12M HCl-solutions for 1 and 10 minutes. Pellets made with sintering program A

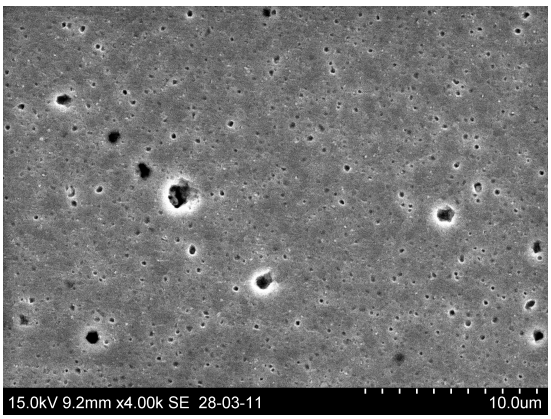

(a) Etched 20 min in 3M HCl

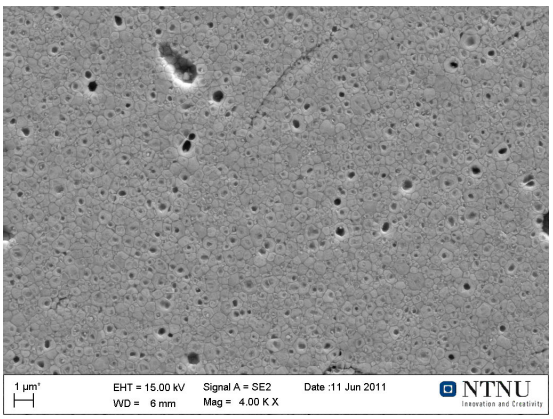

(b) Etched 30 min in 3M HCl

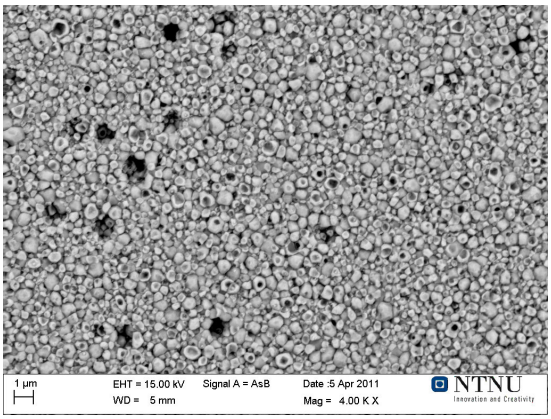

(c) Etched 20 min in 6M HCl

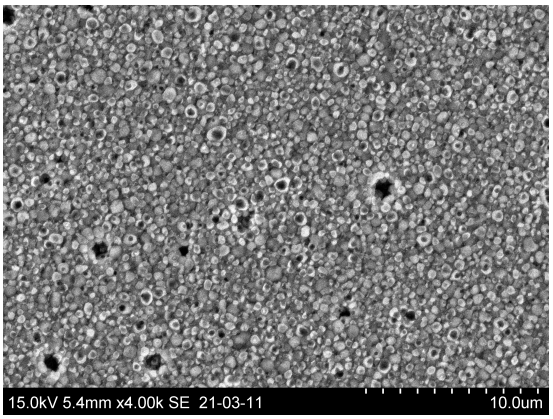

(d) Etched 30 min in 6M HCl

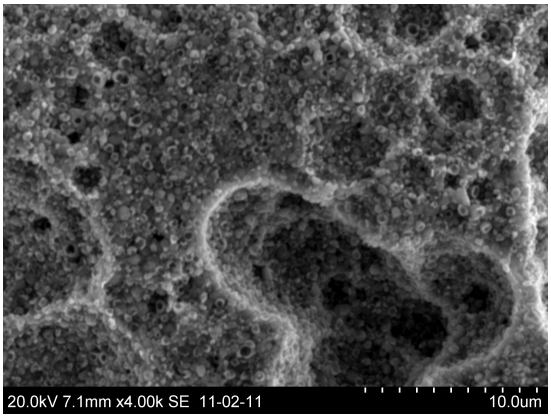

(e) Etched 30 min in 12M HCl

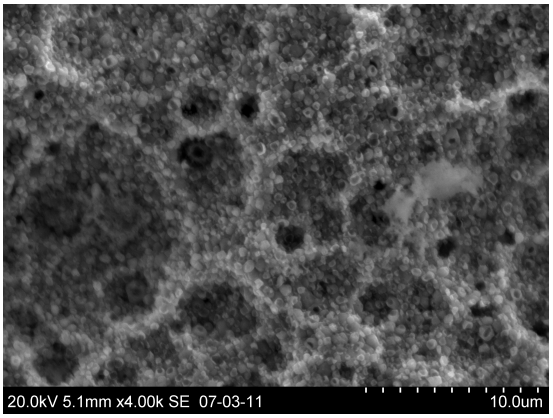

(f) Etched 87 hrs in 12M HCl

Figure 4.5: SEM micrographs of pellet surfaces after room temperature exposure to 3M, 6M and 12M HCl-solutions for varying times. Pellets made with sintering program A

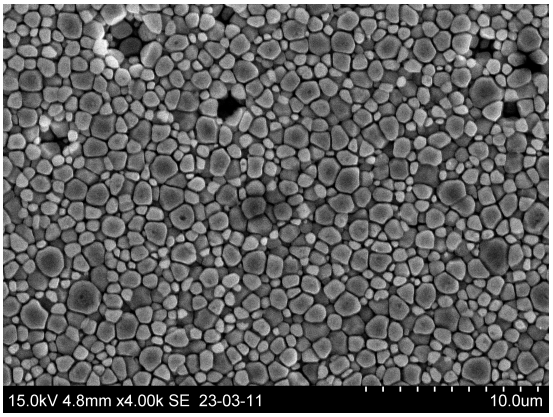

(a) Etched 60 min in 3M HCl

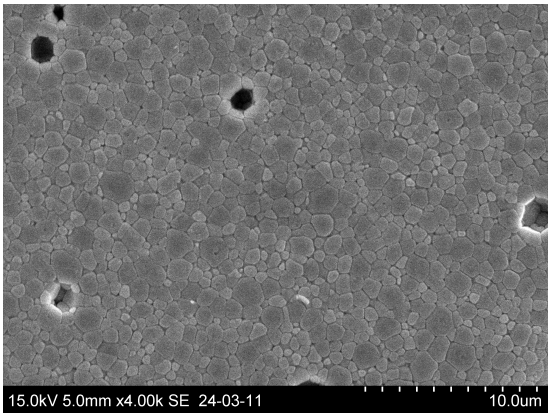

(b) Etched 5 min in 6M HCl

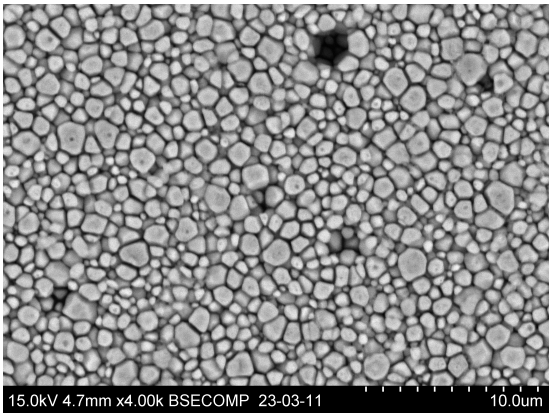

(c) Etched 1 min in 12M HCl

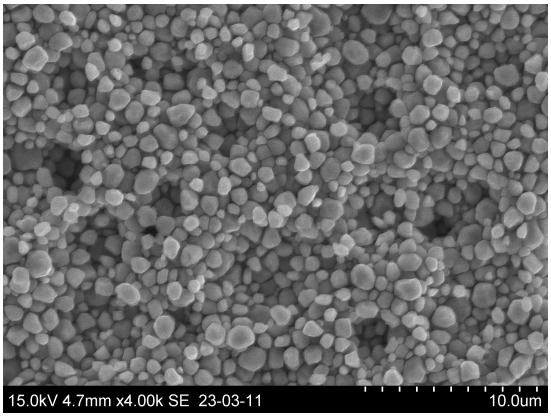

(d) Etched 10 min in 12M HCl

Figure 4.6: SEM micrographs of pellet surface after room temperature exposure to various HCl-concentrations and times. Pellets made with sintering program B

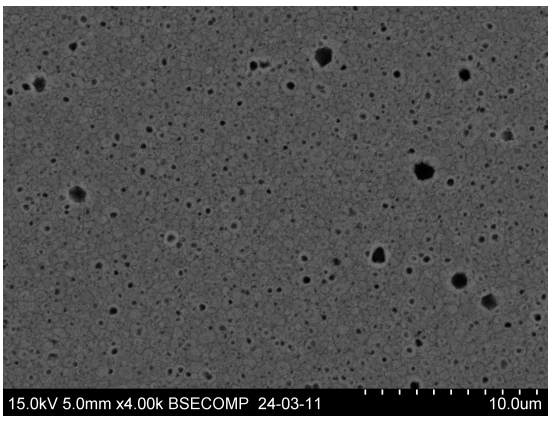

(a) Etched 5 minutes in 6M HCl. Close to pellet surface. Pellet made with sintering program A

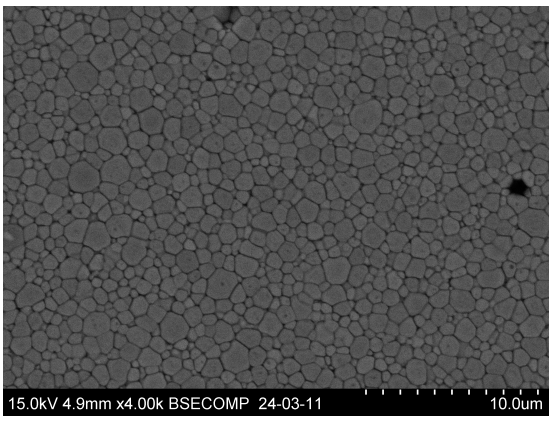

(b) Etched 5 minutes in 6M HCl. Close to pellet surface. Pellet made with sintering program B

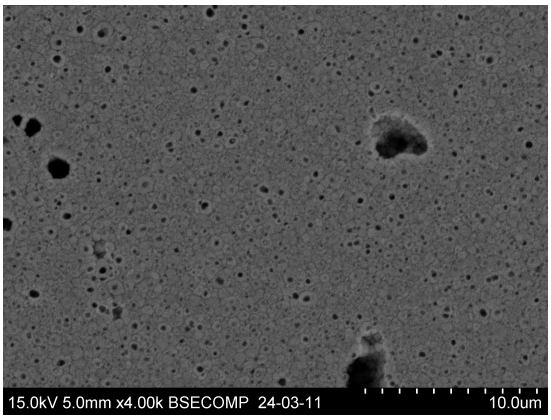

(c) Etched 5 minutes in 6M HCl. Middle of the pellet. Pellet made with sintering program A

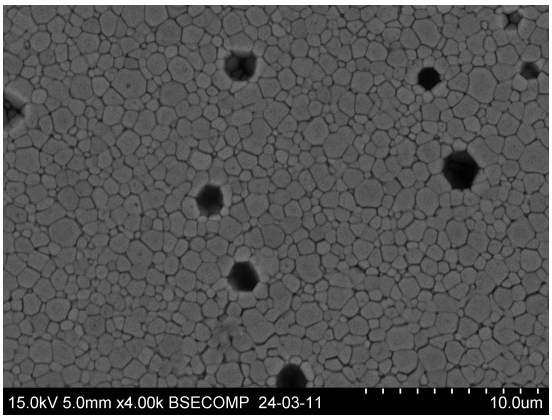

(d) Etched 5 minutes in 6M HCl. Middle of the pellet. Pellet made with sintering program B

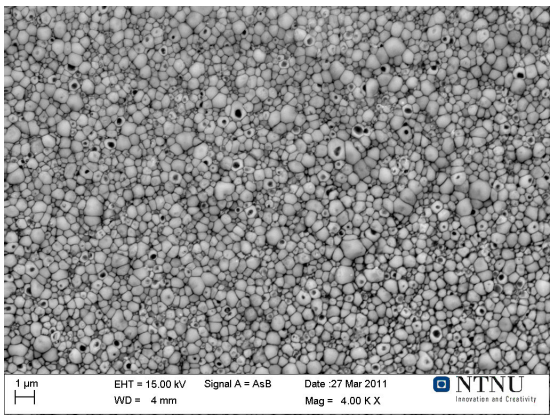

(e) Etched 10 minutes in 6M HCl. The non polished rear side of a pellet made with sintering program A

Figure 4.7: BSE-SEM micrographs of cross sectional polished samples etched for 5 minutes in 6M HCl (a-d) and the unpolished opposing side of the pellet in Figure 4.4d (e)

4.2.2 HNO_3

Figure 4.8 shows SEM micrographs of pellets etched with 14.6M HNO_3-solution for varying times. Little to no etching was observed after sample exposure to 14.6M HNO_3 for 30 minutes (Figure 4.8a). The SEM micrographs of surfaces after etching in 1M are hence not included in this report. A significantly lower etching rate was observed when etching in HNO_3 compared to etching in HCl. It took 6.5 hours to obtain the same surface structure with HNO_3 as was seen for HCl after 1 minute (Figure 4.8b and Figure 4.5e).

The same structure of the primary phase was seen for all samples etched with HNO_3. Precipitation of a secondary phase on the surface was observed after a significant increase of etching time (Figure 4.8c, Figure 4.8d and Figure 4.8e). EDS-analysis of this precipitate indicate a composition rich on tantalum and oxygen. Spectrums 5-8 in Table 4.2 show the measured mole fraction of the different species obtained by EDS. The spectra listed in this table correspond to those shown in Figure 4.8f. The morphology of the precipitate differs to some extent with differing HNO_3-concentration and exposure time, but it remains at the surface and the composition is the same. EDS-analysis of the primary phase (Spectrum 9 and 10) shows a higher Ta to other cations ratio than for the stoichiometric compound indicating a beginning tantalum oxide precipitation, see Section 4.3 for more.

Spectrum 1 and 2 in Figure 4.8f and Table 4.2 show composition of a secondary phase seen in all pellets investigated during this work. See Section 4.3.4 for more about this phase.

Table 4.2: EDS-results showing species atom% corresponding to the points noted in Figure 4.8f

Spectrum	La	Ta	Sr	Fe	O	Sum
Spectrum 1	0.00	0.71	3.09	33.10	63.11	100
Spectrum 2	0.20	0.00	2.84	31.84	65.12	100
Spectrum 3	0.00	0.00	28.53	0.00	71.47	100
Spectrum 4	0.00	0.00	12.52	0.00	87.48	100
Spectrum 5	0.00	23.24	0.00	0.00	76.76	100
Spectrum 6	0.66	22.79	0.00	3.06	73.49	100
Spectrum 7	0.00	20.55	0.00	2.62	76.82	100
Spectrum 8	0.00	25.46	0.00	2.90	71.64	100
Spectrum 9	5.54	8.72	15.64	21.88	48.22	100
Spectrum 10	5.44	7.12	0.00	20.57	66.87	100

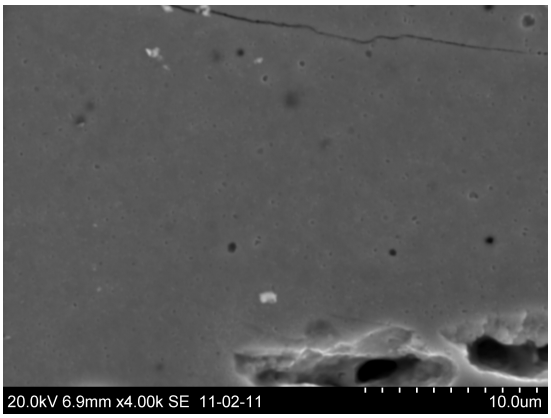

(a) Etched 30 min in 14.6M HNO_3

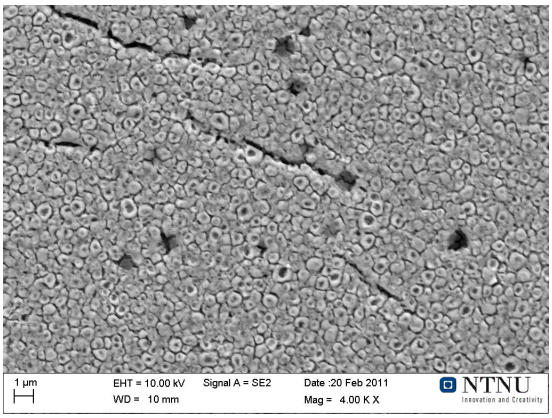

(b) Etched 6.5 hrs in 14.6M HNO_3

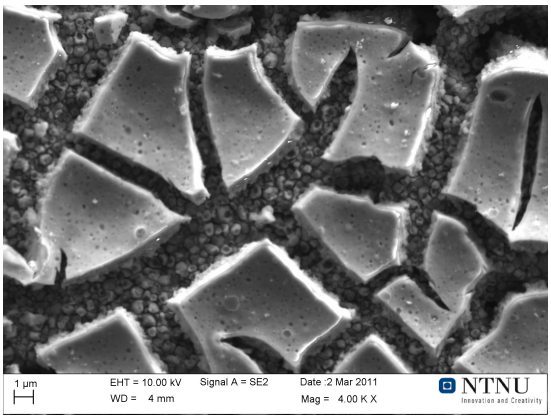

(c) Etched 23 hrs in 14.6M HNO_3

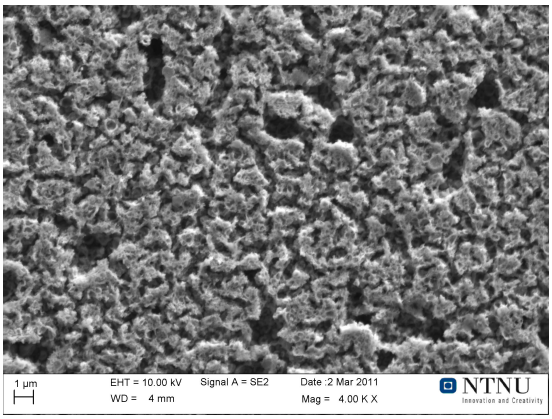

(d) Etched 23 hrs in 7.3M HNO_3

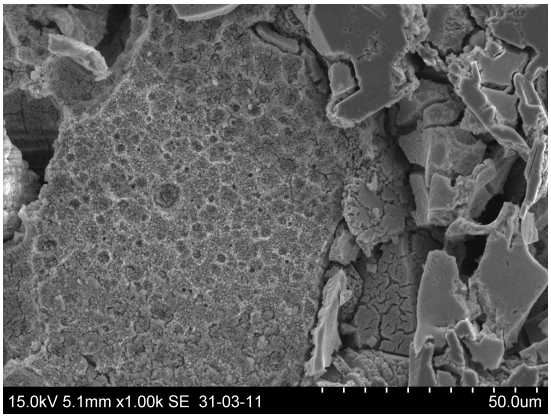

(e) Etched 23 days in 14.6M HNO_3

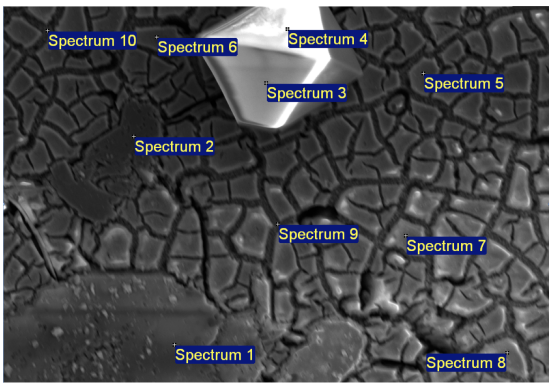

(f) Points investigated using EDS on pellet showed in Figure 4.8c

Figure 4.8: SEM micrographs of pellet surface after room temperature exposure to various HNO_3-concentrations and times. Pellets made with sintering program A

4.2.3 KOH

Figure 4.9 shows the pellet surface after exposure to alkaline 20M KOH-solution for varying exposure times. The etching effect from KOH-solution is very low as no signs of etching can be seen even after 24 days in close to saturated KOH (Figure 4.9b). Figure 4.9 shows the results from the two longest experiments with KOH. As no etching is visible on these samples, SEM micrographs of the other samples are not included.

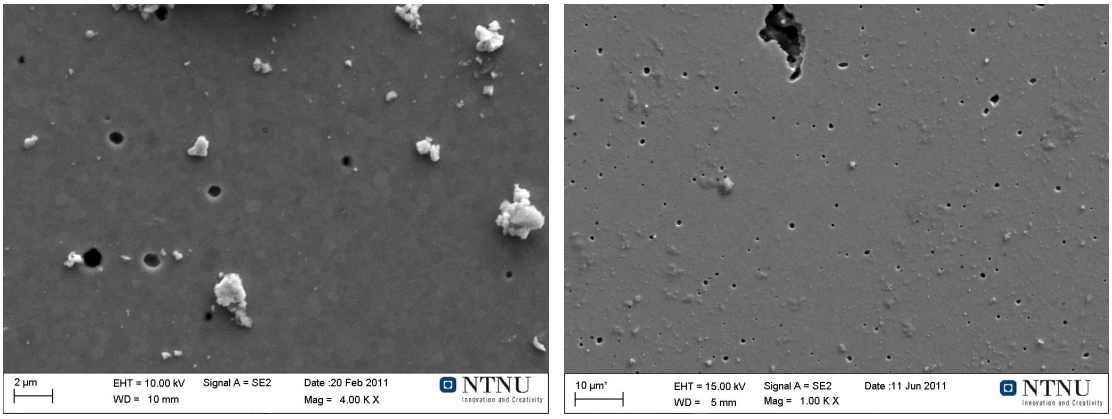

(a) Etched 6.5 hrs in 20M solution

(b) Etched 24 days in 20M solution

Figure 4.9: SEM micrographs of pellet surface after room temperature exposure to 20M KOH solutions for various times. Pellets made with sintering program A

4.2.4 H_2SO_4

Figure 4.10 shows the result of etching experiments using 18.6M H_2SO_4-solution with varying exposure time. A slower etch rate was observed compared to etching with HCl, but still faster than what was seen for HNO_3-etch (compare Figure 4.4e, Figure 4.8a and Figure 4.10a). A surface structure development comparable to the above reported surface structure for HCl was observed; starting with mid grain and grain boundary etching (Figure 4.10b and Figure 4.10c) through more aggressive etching around the grains (Figure 4.10d) ending up with a very rough surface shown in Figure 4.10e and Figure 4.10f.

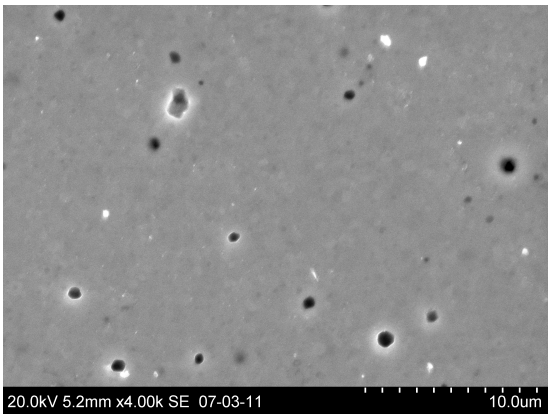

(a) Etched 1 min in 18M H_2SO_4

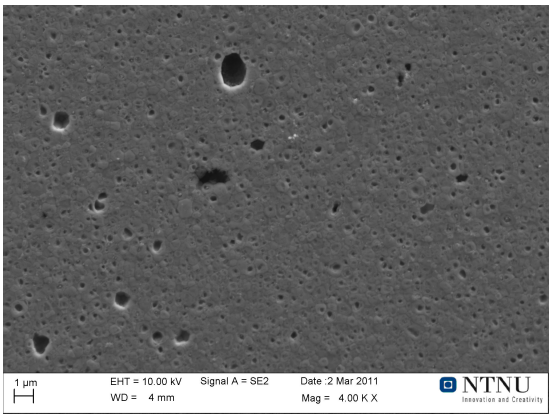

(b) Etched 10 min in 18M H_2SO_4

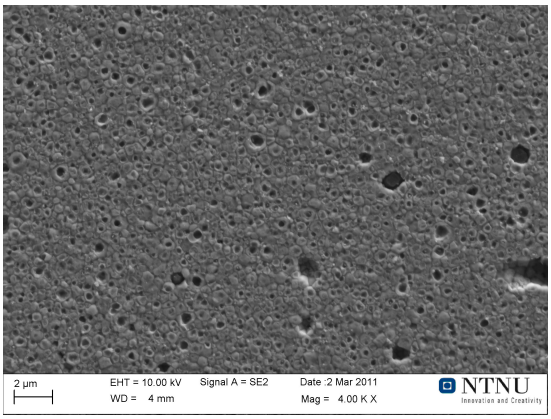

(c) Etched 30 min in 18M H_2SO_4

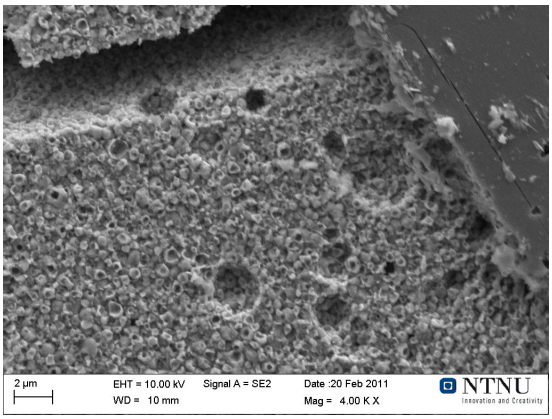

(d) Etched 6.5 hrs in 18M H_2SO_4

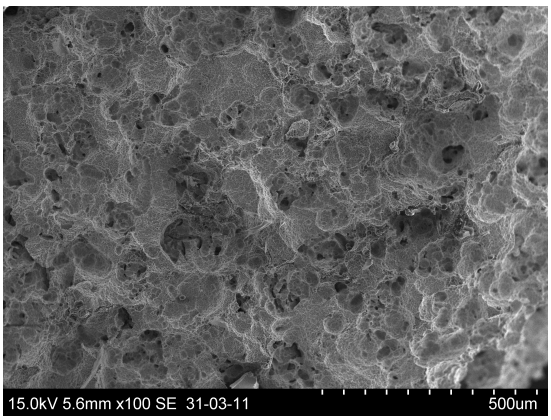

(e) Etched 23 days in 18M H_2SO_4 (note alternate scale)

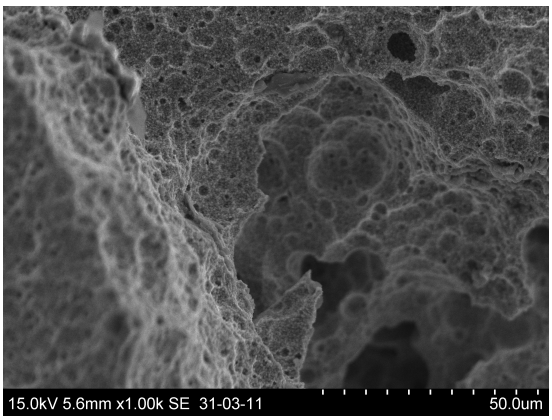

(f) Etched 23 days in 18M H_2SO_4 (note alternate scale)

Figure 4.10: SEM micrographs of pellet surface after room temperature exposure to various H_2SO_4-concentrations and times. Pellets made with sintering program A

4.2.5 $H_2C_2O_4$

Figure 4.11a and Figure 4.11b show the pellet surface after etching with $H_2C_2O_4$ for 60 minutes and 23 hours, respectively. The etching starts at the grain boundaries and in the middle of the grains as was seen for HCl, HNO_3 and H_2SO_4. Only a modest surface structuring was achieved after as long as 21 days making $H_2C_2O_4$ a very slow etchant (Figure 4.11c)

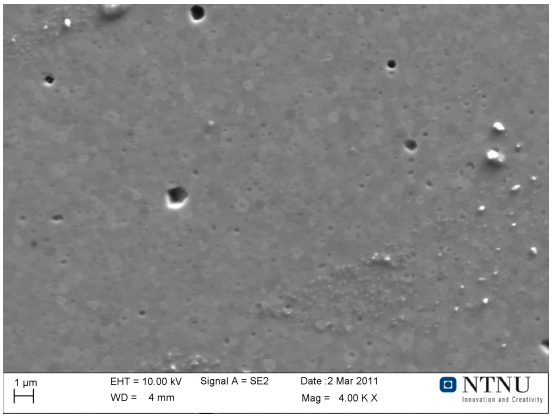

(a) Etched 60 min in 1.13M $H_2C_2O_4$

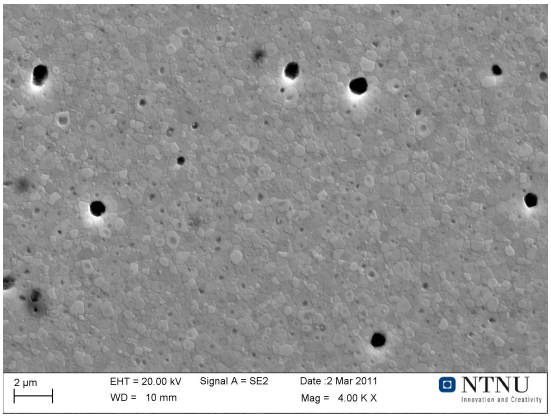

(b) Etched 23 hrs in 1.13M $H_2C_2O_4$

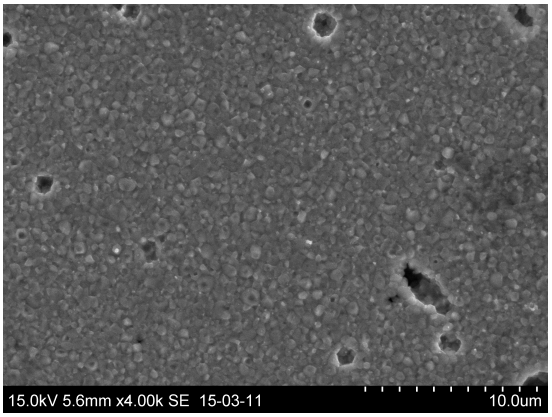

(c) Etched 21 days in 1.13M $H_2C_2O_4$

Figure 4.11: SEM micrographs of pellet surface after room temperature exposure to 1.13M $H_2C_2O_4$ solutions at various times. Pellets made with sintering program A

4.2.6 $NaHCO_3$ and Na_2CO_3

Figure 4.12 shows the sample surfaces after etching with $NaHCO_3$ and Na_2CO_3. After 26 days of exposure, some grains exposed to $NaHCO_3$ show extensive mid grain etching, while the etching of grain boundaries is almost non existing (Figure 4.12a and Figure 4.12b). No significant etching was observed after the same time in Na_2CO_3 (Figure 4.12c).

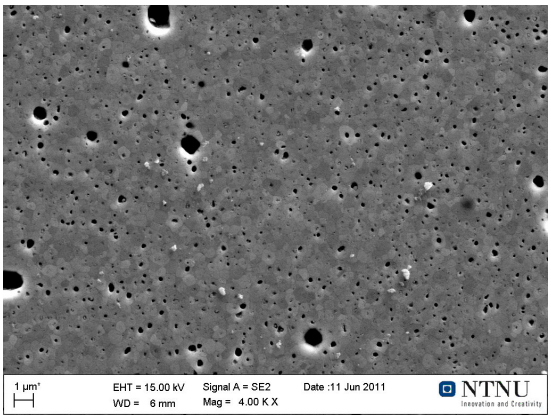

(a) Etched 26 days in 1.23M $NaHCO_3$

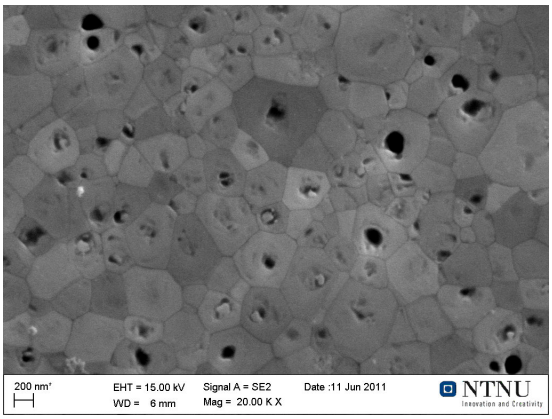

(b) Etched 26 days in 1.23M $NaHCO_3$ (note the alternate scale)

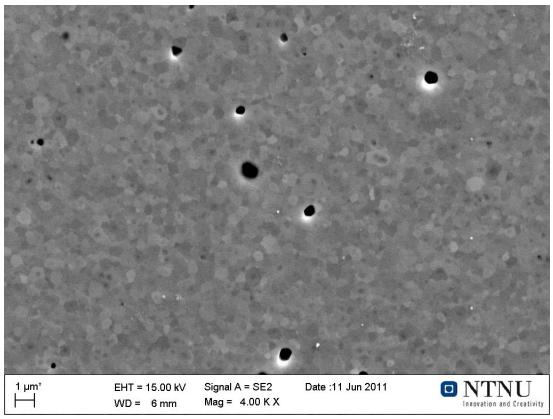

(c) Etched 26 days in 2.07M Na_2CO_3

Figure 4.12: SEM micrographs of pellet surface after room temperature exposure to $NaHCO_3$- and Na_2CO_3-solutions at various times. Pellets made with sintering program A

4.3 Wet Chemical Etching - Surface Chemistry

4.3.1 Changes to Etchant Solution

All the solutions used in the etching experiments were colourless and transparent before etching started. Below is a summary of effects observed in the etchant solutions by visual inspection during experiments.

HCl All the solutions turned yellow after a short time (except the samples exposed to the lowest concentrations for the shortest times). The colour changed to red/brown after about 1 day. A yellowish precipitate was visible at the end of the 87 hours experiment.

HNO_3 The solution changed to brown/green after three days of sample exposure. A hint of yellow was observed after two more days. No precipitates were visible.

H_2SO_4 Bubbles were observed on the pellet surface after 11 days of etching. A white precipitate had formed on the beaker bottom after additional 12 days.

KOH, $H_2C_2O_4$, $NaHCO_3$ and Na_2CO_3 No changes were observed for the KOH-, $H_2C_2O_4$-, $NaHCO_3$- and Na_2CO_3-solution during the experiments.

4.3.2 Changes to Crystal Structure

XRD-spectra of the pellets used were recorded before and after exposure to the etching solutions. All the samples retained their original cubic perovskite structure (Figure 4.13). Secondary peaks can be seen on samples etched with HNO_3 possibly originating from $Fe(OH)_2$ and paste from the sample holder (X). The secondary peaks seen after etching with $H_2C_2O_4$ remain unidentified. The tantalum oxide phase seen after etching with HNO_3 would be expected to show up on the XRD-spectrum but it is not possible to identify this phase from the XRD-spectra recorded. This could be because the tantalum oxide may exist in a hydrated amorphous form [34]. After etching with H_2SO_4 a shift to smaller θ-values was observed. This shift was of similar size for all the cubic perovskite peaks, as seen in Figure 4.13.

4.3.3 Changes to Surface Chemistry

The primary phase of the pellet pieces used in this work was analysed by EDS to study changes to surface composition after etching. The primary phase is herein used as a term for the perovskite main phase as i.e. seen in Figure 4.5e. The analysis was done for comparison between originally equal samples, not for exact quantitative analysis.

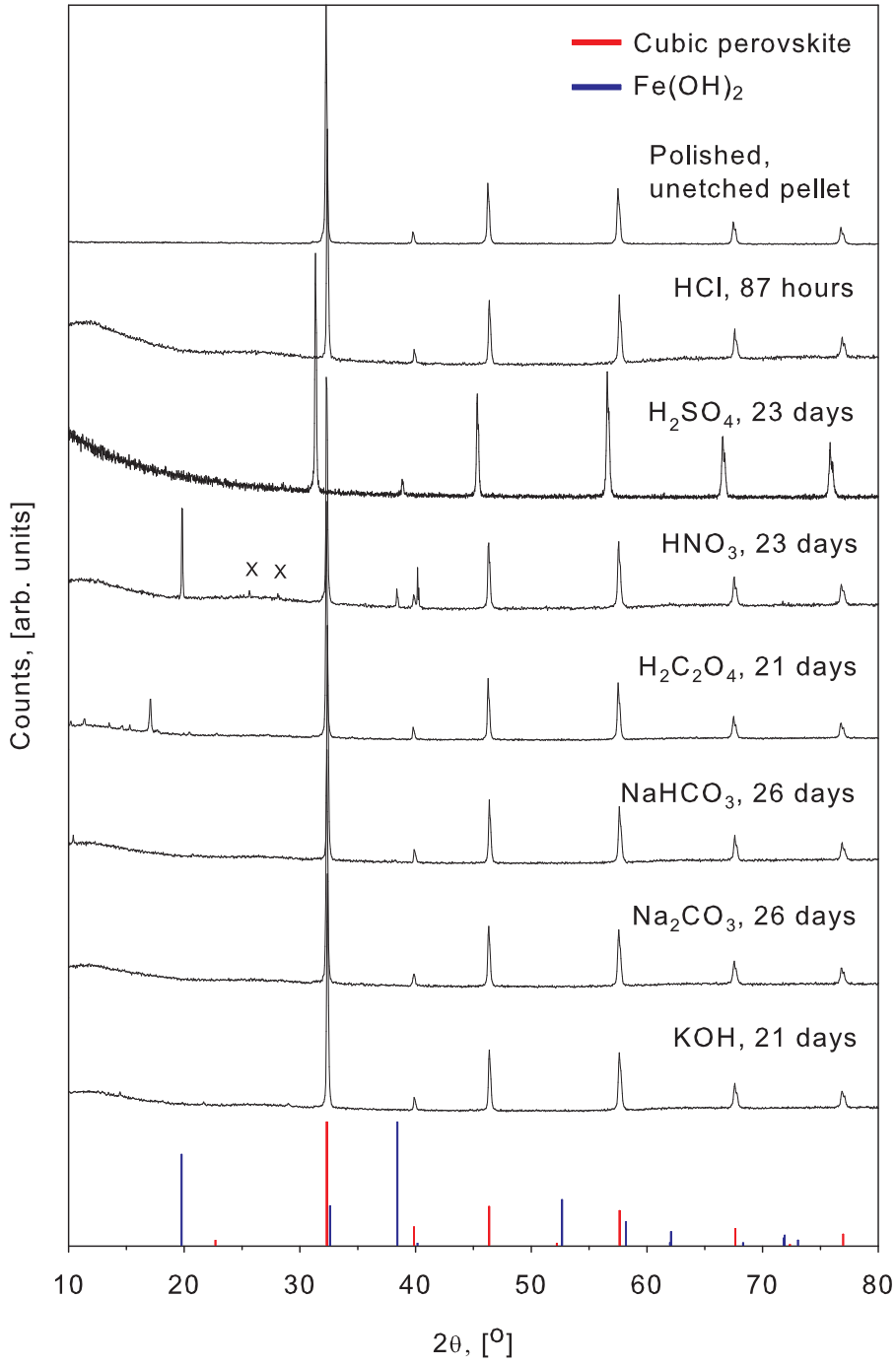

Figure 4.13: XRD-spectra of an as polished pellet and pellets after etching. Ref. $Fe(OH)_2$; [65], Cubic perovskite; [66], X=paste on sample holder

Averaged results ($\bar{S}$) with their standard deviations (σ) from this analysis and the theoretical composition of the stoichiometric LSFT are shown in Table 4.3. "Overall" shows the measured stoichiometry if all data points for the four etchants are combined.

A decrease of Sr-content relative to Fe-content was seen after sample exposure to HCl, HNO_3 and H_2SO_4. The increased tantalum content on the surface of HNO_3-etched samples coincides with the precipitation of tantalum oxide that was seen in Section 4.2.2. It is important when analysing these data to take note of the large σ associated with many of the values. The data may hence be used for comparison between each other, and not as exact stoichiometric determination.

Table 4.3: EDS-analysis of primary phase surfaces in [atom%].
$\bar{S}$ = average value, σ = standard deviation

Sample treatment	# data points	La		Ta		Sr		Fe		O	
		$\bar{S}$	σ	$\bar{S}$	σ	$\bar{S}$	σ	$\bar{S}$	σ	$\bar{S}$	σ
Stoichiometric	-	4	-	4	-	16	-	16	-	60	-
Unetched	39	4	0	3	0	16	1	15	2	62	3
HCl	22	5	2	6	4	15	6	20	8	54	12
H_2SO_4	14	6	3	3	1	12	4	33	20	46	18
$H_2C_2O_4$	12	6	5	3	2	12	7	11	6	68	11
HNO_3	29	4	2	8	9	10	8	16	6	61	8
Overall	77	5	3	6	6	12	7	29	12	57	15

4.3.4 Secondary Iron Rich Phase

A secondary phase was observed in all pellets directly after sintering. The phase was analysed by XRD and the additional peaks, which do not originate from the cubic perovskite phase, correspond to the phase $SrFe_{12}O_{19}$ (Figure 4.14) [67]. The phase was also investigated using EDS, showing the same result. Table 4.4 shows $\bar{S}$ (atom%) and σ of 36 EDS point scans of the secondary phase. The scans were done on etched and unetched samples subjected to both sintering program A and B, on surfaces and cross sections. The composition approximately corresponds to the phase $SrFe_{12}O_{19}$ (magnetoplumbite).

Figure 4.15 shows SE-SEM and BSE-SEM micrographs of the secondary phase seen in samples from all the different sintering programs described in Section 3.2.1. The secondary phase is evenly distributed both on the surface and in the bulk of the pellet. Increasing the sintering time and temperature changes the morphology of the phase

from particle/sphere like shapes to long threads/needles. Figure 4.15e shows significant etching around the secondary phase particles, but only limited etching of the secondary phase it self.

Table 4.4: EDS-analysis of secondary iron rich phase, [atom%].
$\bar{S}$ = average value, σ = standard deviation

	La	Ta	Sr	Fe	O
$\bar{S}$	0	0	3	33	64
σ	0	0	1	6	6

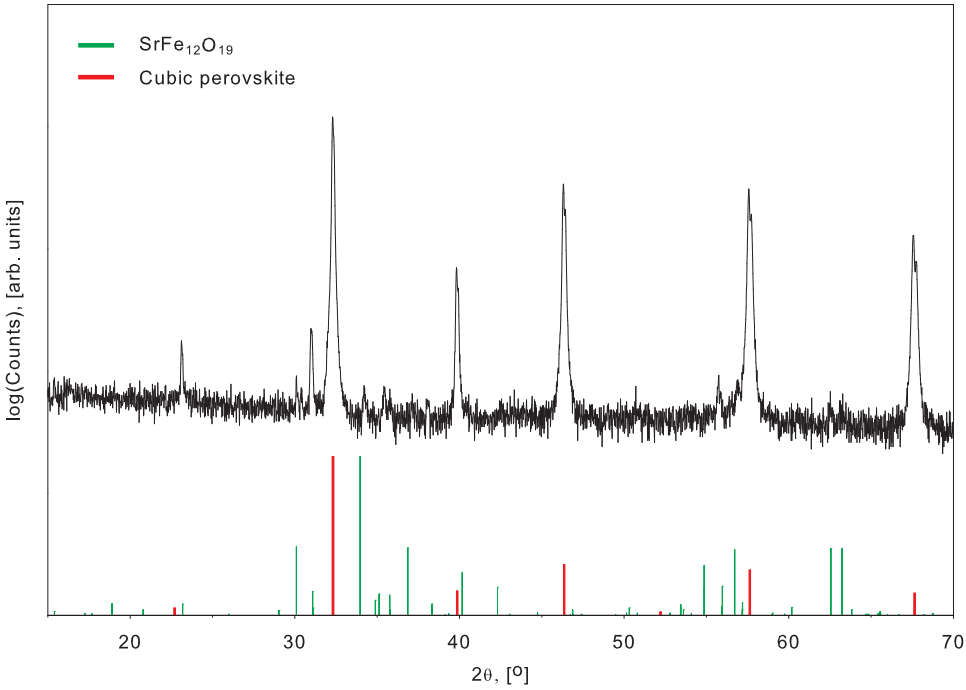

Figure 4.14: XRD-spectrum of the sample used for ECR. Note the log scale on the ordinate axis due to low secondary peak intensity. The small secondary peaks correspond to the secondary phase $SrFe_{12}O_{19}$ [67], Cubic perovskite; [66]

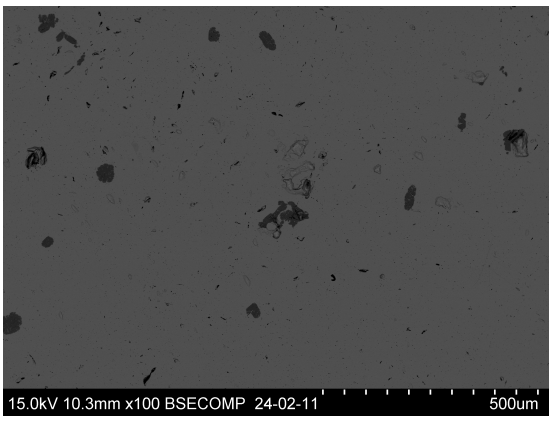

(a) Polished surface of a sintered pellet of sintering program A

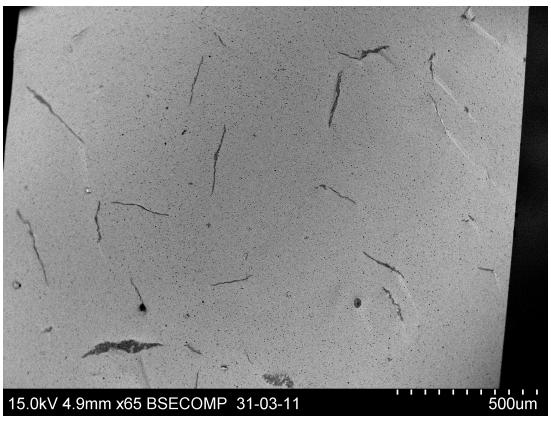

(b) Polished cross section of a sintered pellet of sintering program B

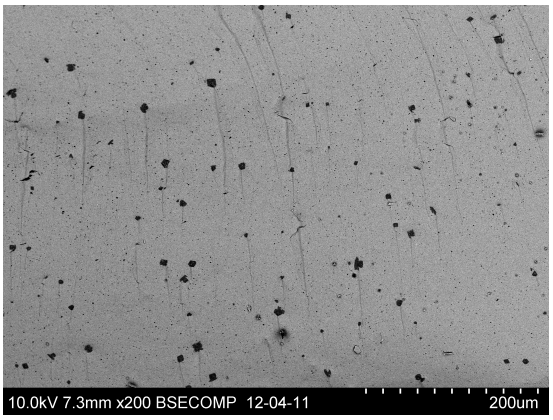

(c) Unpolished cross section of a sintered pellet of sintering program C

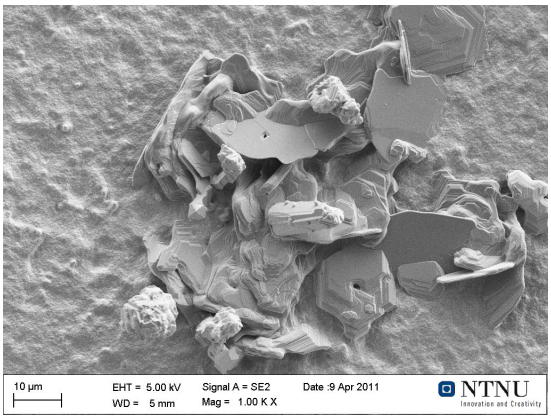

(d) Unpolished surface of a sintered pellet of sintering program C

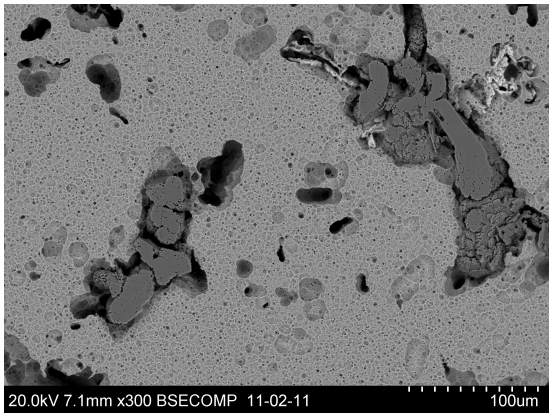

(e) Surface of pellet etched in 12M HCl for 30 minutes showing etching around the secondary phase. Sintering program A

Figure 4.15: SEM micrographs showing a secondary phase after all sintering programs

4.4 Carbonate Growth in CO_2 Atmosphere at High Temperature

Figure 4.16a and Figure 4.16b show pellet surfaces after exposing a polished sample to $p_{O_2} = p_{tot} = 1$ atm for 1 and 96 hours respectively. No significant carbonate growth was observed after 96 hours (Figure 4.16b and Figure 4.16c). Examination of the cross section confirms this, showing no signs of carbonate formation inwards in the sample (Figure 4.16d). The bright particles seen on the surfaces have been identified as surface impurities present before the experiment started. Some small carbon- and strontium-enriched spots were identified on the surface by EDS-analysis, but these were very sparsely spread out. There was a slight increase of the amount of these spots when increasing the experiment duration from 1 to 96 hours.

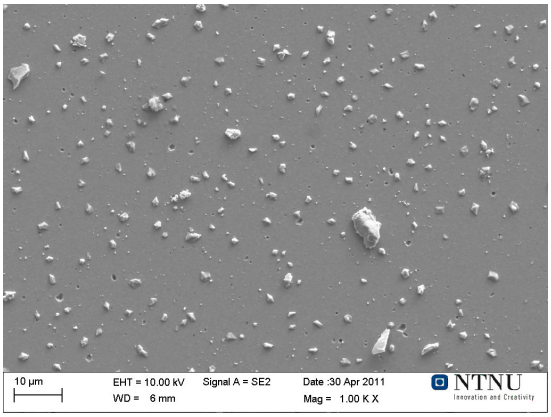

(a) Surface of pellet exposed to dry CO_2(g) 1 hour at 900°C

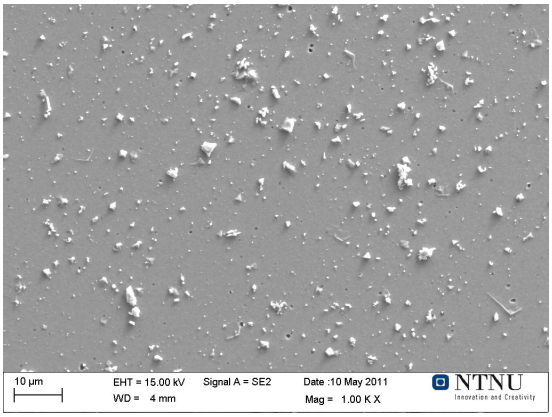

(b) Surface of pellet exposed to dry CO_2(g) 96 hours at 900°C

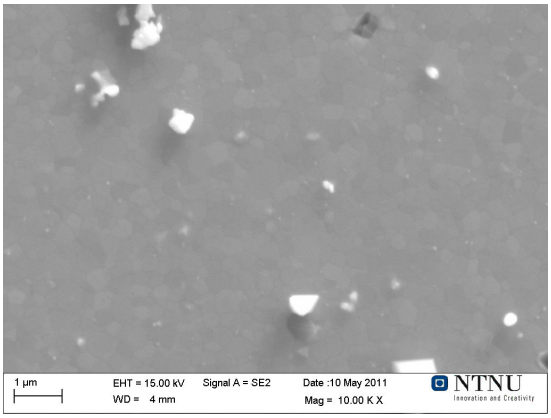

(c) Surface of pellet exposed to dry CO_2(g) 96 hours at 900°C (note alternate scale)

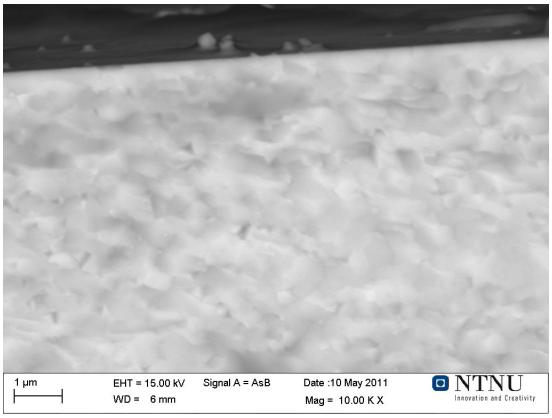

(d) Cross section of pellet exposed to dry CO_2(g) 96 hours at 900°C (note alternate scale)

Figure 4.16: SEM micrographs of pellets exposed to $p_{tot} = p_{CO_2} = 1$ atm for 1 and 96 hours at 900°C

Figure 4.17a - 4.17d show SEM micrographs of pellet surfaces after exposing a polished surface to dry and wet CO_2-atmospheres at 1000°C for 25 hours. The terms dry and wet CO_2 refer to pure CO_2 ($p_{tot} = p_{CO_2} = 1$ atm) and CO_2 saturated with water ($p_{tot} = p_{CO_2} + p_{H_2O} = 1$ atm), respectively. It is clear that limited growth of a secondary phase has taken place in the form of particle like features on the surfaces. The growth does not cover the complete sample surface, as confirmed by examination of the sample cross sections (Figure 4.17e and Figure 4.17f). The secondary phase proved to be enriched on carbon and strontium according to point scan EDS-analysis indicating the presence of $SrCO_3$ (Table 4.5). A slight increase of the carbon content on the primary surface and a doubling of the carbon content on the secondary phases was found. The difference between samples treated in dry and wet CO_2 is negligible. No secondary phase could be identified by the recorded XRD-spectra for the samples exposed to CO_2 (Figure 4.18. The experiments done at 1000°C led to thermal etching of the surface, as can be seen in Figure 4.17b and Figure 4.17d.

Table 4.5: Phase compositions found with EDS after pellet exposure to dry and wet CO_2 at 1000°C, [atom%]. $\bar{S}$ = average value, σ = standard deviation

Phase	Gas mix	# data points	La		Ta		Sr		Fe		O		C	
			$\bar{S}$	σ	$\bar{S}$	σ	$\bar{S}$	σ	$\bar{S}$	σ	$\bar{S}$	σ	$\bar{S}$	σ
Primary	None	36	4	0	3	0	15	1	14	2	59	4	6	5
	Dry	16	4	0	3	0	16	0	14	1	56	1	8	1
	Wet	14	4	0	3	0	16	0	14	1	55	1	8	1
Second.	Dry	16	3	1	3	0	15	1	11	2	53	1	16	3
	Wet	10	3	1	3	1	14	1	10	2	54	2	17	3

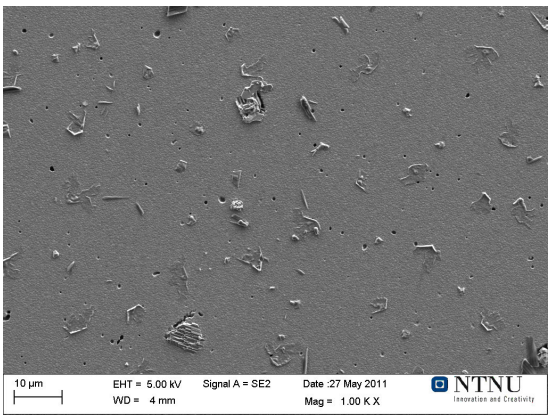

(a) Pellet exposed to dry CO_2(g)

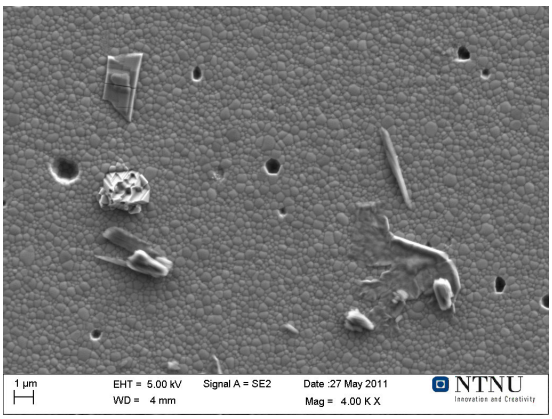

(b) Pellet exposed to dry CO_2(g)

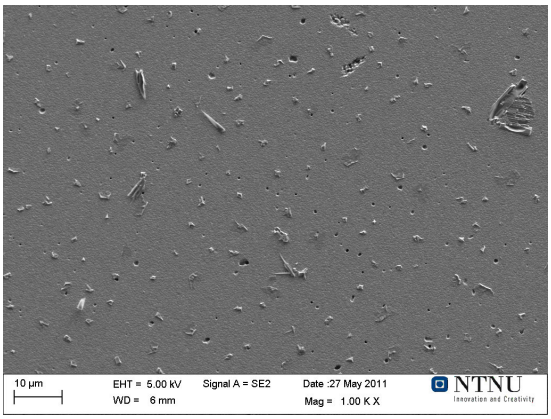

(c) Pellet exposed to wet CO_2(g)

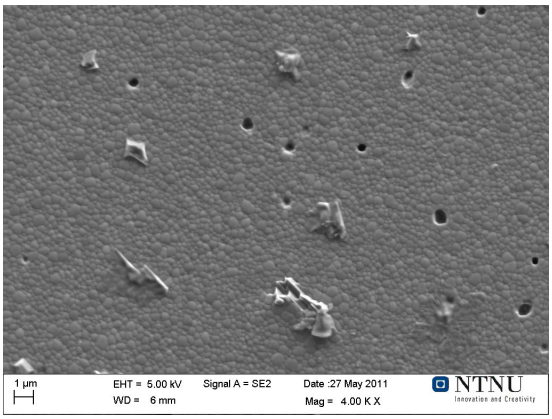

(d) Pellet exposed to wet CO_2(g)

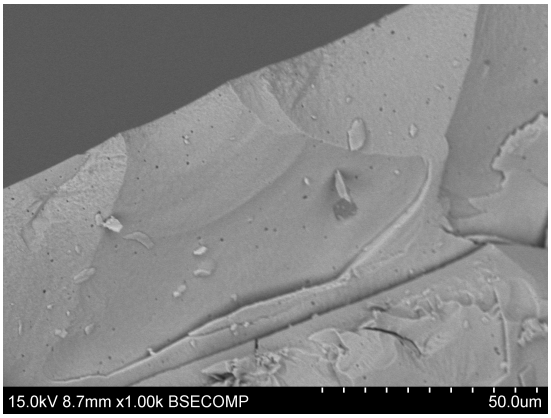

(e) Cross section of pellet exposed to dry CO_2(g)

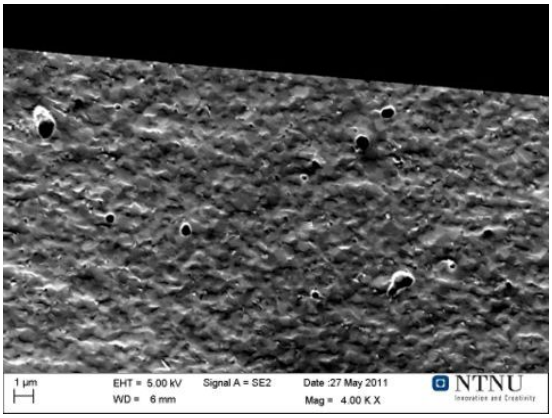

(f) Cross section of pellet exposed to wet CO_2(g)

Figure 4.17: SEM micrographs of pellets exposed to pure CO_2 atmosphere (p_{CO_2}=1 atm) and wet CO_2 atmospheres (p_{CO_2}=0.97 atm, p_{H_2O}=0.03 atm) for 25 hours at 1000°C

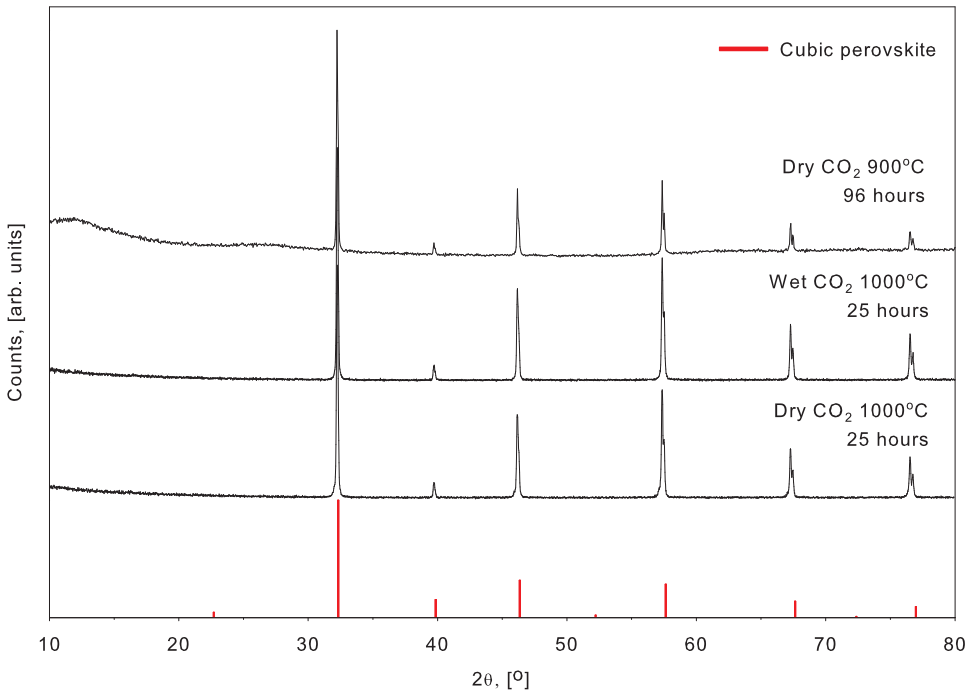

Figure 4.18: XRD-spectra recorded after CO_2-experiments showing only cubic perovskite phase [66]

As noted in Section 3.2.3 all samples were weighed before and after exposure to CO_2 as a source for the amount of carbonate formed on the surface. The masses are not reported here since all samples showed decreased weight as a result of the experiment.

4.5 Electrical Conductivity Relaxation

4.5.1 Sample Characteristics

The surface of the sample used for ECR-experiments was studied using SEM and AFM. Figure 4.19a shows a SEM micrograph of the surface representing the one used in the ECR-experiments directly after it was etched. A 2D and 3D representation of the same surface obtained by AFM imaging are shown in Figure 4.19b and Figure 4.19c respectively. The sample density was found to be >98% of theoretical density calculated as described in Section 3.2.5.

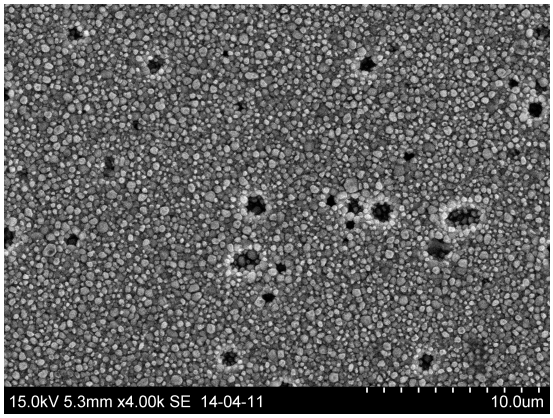

(a) SEM micrograph of the surface used for ECR-experiments

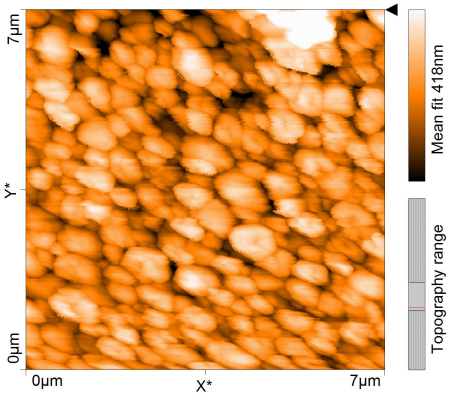

(b) 2D representation

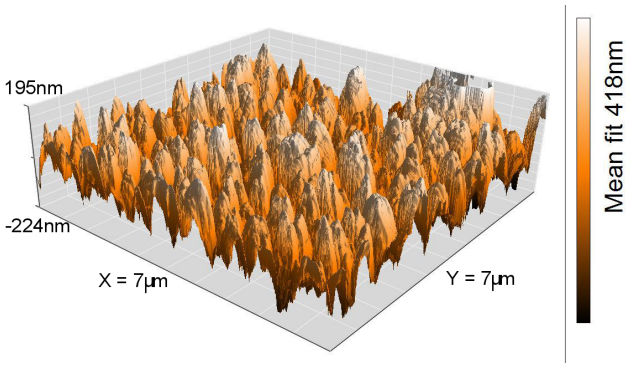

(c) 3D representation

Figure 4.19: SEM micrograph, 2D AFM and 3D AFM representation of the sample surface used for ECR-experiments

Quantitative characterization of the surface was done to compare the surface structured sample with the polished surface (reported in Section 4.1). The surface roughness and

specific surface area of the etched sample are shown in Table 4.6 together with the projected and normalized area.

Table 4.6: Surface characteristics for surface structured ECR-sample, $N_{sa} = S_{sa}/S_{pa}$

Property	Value	Unit
S_a	73.1983	nm
S_{pa}	$4.9 \cdot 10^7$	nm^2
S_{sa}	$1.9406 \cdot 10^8$	nm^2
N_{sa}	3.96041	-

Figure 4.20 shows XRD-spectra recorded before and after the ECR-experiment on the sample used. It shows a mainly pure cubic perovskite structure, with some small secondary peaks. The secondary peaks are found to correspond to an $SrFe_{12}O_{19}$ phase as described in Section 4.3.4. The increased background noise seen in the spectrum taken after ECR-experiments probably stems from the plastic sample holder and conductivity paste used to ensure good connection between the sample and the current electrodes during ECR.

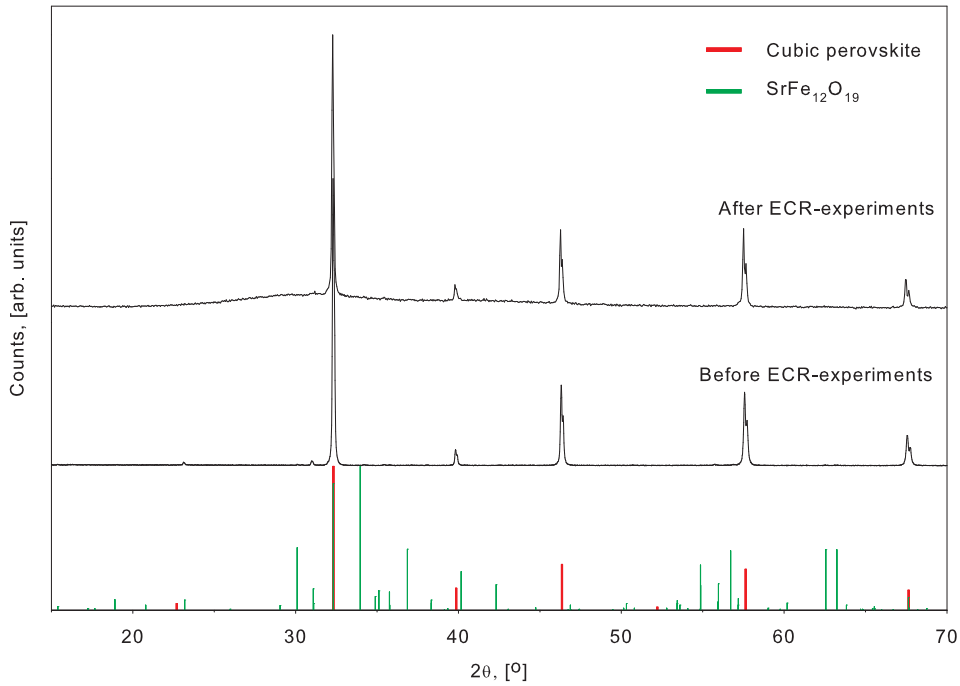

Figure 4.20: XRD-spectra recorded before and after ECR-experiments. Ref. $SrFe_{12}O_{19}$; [67], Cubic perovskite; [66]

4.5.2 Relaxation Experiments

Figure 4.21 shows $\log(D_{chem})$ and $\log(k_{chem})$ obtained from electrical conductivity relaxation experiments performed on a surface structured membrane at 800°C and 900°C (red marks). For comparison, Figure 4.21 also provides results from ECR-experiments done on a polished membrane without surface structuring (blue marks)[1]. Both the etched and polished sample have the same thermal history and similar dimensions, but they are made from two different batches of powder (both powders from CerPoTech AS, Trondheim, Norway).

The slope, a, of the trend lines drawn for each series of $\log(k_{chem})$-values in Figure 4.21 is listed in Table C.1. The slope values were obtained by linear regression as described in Appendix C. The slopes are all within each others standard deviations showing that k_{chem} depend on p_{O_2} in the same way as before the structuring was done.

Table 4.7 shows Δk_{chem}, which denotes the relative logarithmic increase of k_{chem} as a result of the surface structuring done in this work. The increase of k_{chem} at 800°C and the reduction steps at 900°C is around half an order of magnitude. Δk_{chem} is obtained using Equation 4.1 as described in Appendix C. It is clear that k_{chem} has increased for all temperatures and oxygen partial pressures, whereas the effect seem to be lower as the temperature and p_{O_2} increase.

$$\Delta k_{chem} = log\left(k^{calc}_{chem}(\text{Etched surface})\right) - log\left(k^{calc}_{chem}(\text{Polished surface})\right) \tag{4.1}$$

Table 4.7: Δk_{chem} for the different temperatures and p_{O_2} investigated. p_{O_2} refers to the end pressure for a given relaxation

$\log(p_{O_2})$		-1.18		-1.70		-2.22		-2.70	
		Δk_{chem}	σ	Δk_{chem}	σ	Δk_{chem}	σ	Δk_{chem}	σ
800°C	Red.	0.47	0.10	0.49	0.09	0.51	0.08	0.53	0.07
800°C	Ox.	0.47	0.03	0.46	0.03	0.45	0.02	0.44	-
900°C	Red.	0.41	0.14	0.49	0.12	0.58	0.11	0.66	0.09
900°C	Ox.	0.27	0.11	0.31	0.10	0.35	0.08	0.39	0.06

[1] Previous unpublished work done by Ørjan Fossmark Lohne as a part of his PhD-thesis at the Norwegian University of Science and Technology, NTNU

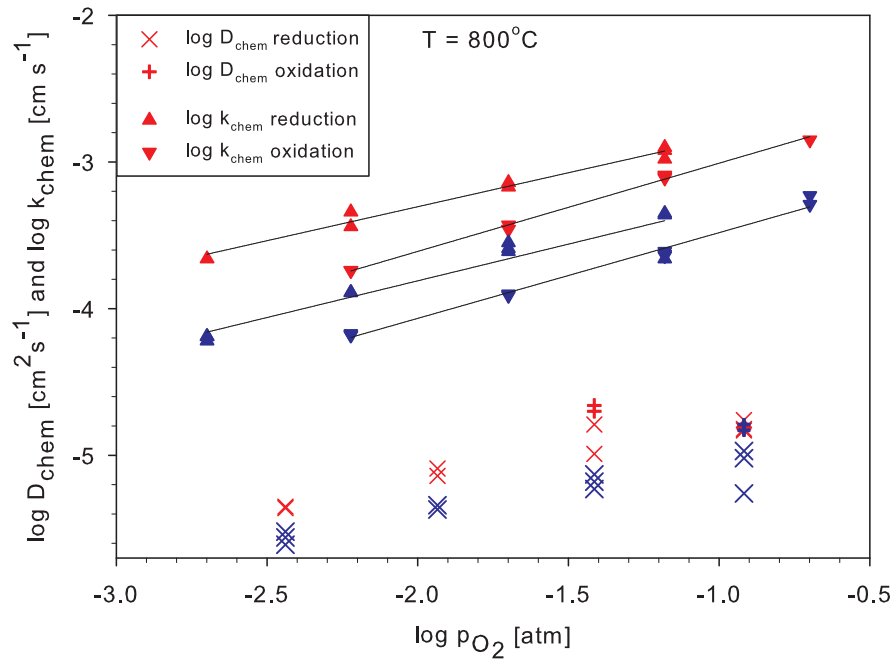

(a) Fitted results from ECR-experiments at 800°C

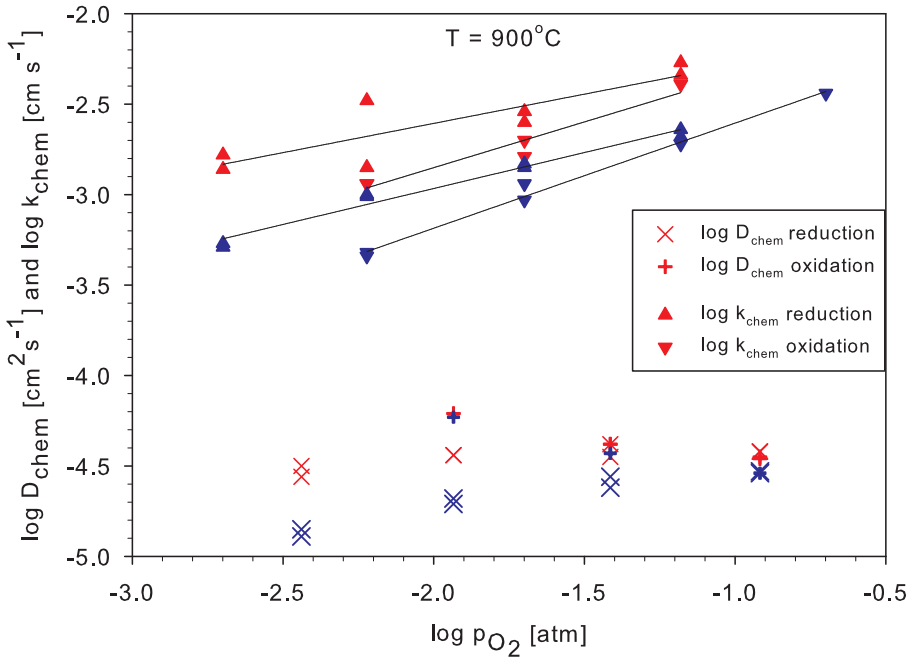

(b) Fitted results from ECR-experiments at 900°C

Figure 4.21: log(k_{chem}) and log(D_{chem}) for ECR-experiments with a surface structured sample (red) and polished sample (blue)

5 Discussion

5.1 Wet Chemical Etching

Several different etchant solutions were used during this work. The intention was to structure the surface of LSFT-membranes to obtain an improved surface exchange rate. The observations from these etching experiments are discussed in the subsequent section.

5.1.1 Etchant Characteristics

Etch Rate Large differences were observed with respect to the etch rate. This statement is based on qualitative observations from SEM micrographs and visual inspection during the course of the experiments. The highest etch rate was seen for HCl, followed by H_2SO_4 and HNO_3. The remaining etchants showed an etch rate decreasing from $H_2C_2O_4$ > $NaHCO_3$ > Na_2CO_3 ≫ KOH. KOH did not show any signs of etching behaviour at all after 24 days. No quantitative study was done to compare the etch rate of the different etchants.

The etch rate seem to roughly increase with decreasing pH, see Appendix D for pH calculations. The three strong acids that showed the highest etch rates are also the ones with the lowest pH. Etching in KOH at the other end of the pH-scale was attempted and did not show any etching at all. This is also supported by what was seen with the expanded concentration study for HCl-etching. The etch rate decreased upon reduction of etchant concentration. Ranking the three strong acid solutions by increasing pH leaves the order; H_2SO_4 <HNO_3 <HCl (assuming full dissociation). This does not fully coincide with the order seen when sorting by increasing etch rate; HNO_3 < H_2SO_4 ≪HCl. It is hence apparent that pH is not the only factor influencing the etch rate, though very important. There are several equilibria possible in an aqueous solution with four different cations and at least two different anions. This implies that equilibria involving these, such as precipitation and complexing, should be considered. This is discussed further in Section 5.1.2.

Selectivity A small degree of selectivity was observed for all etchants showing etching behaviour, judging from the EDS-results listed in Table 4.3. The numbers in this table have a large error and will hence only be used for comparison, not for exact composition evaluations. A comparison of the internal ratio between A-cations (La and Sr) and between B-cations (Fe and Ta) makes it clear that for all etchant solutions except H_2SO_4 the EDS-analysis shows depletion of the cation making the most basic oxide at the given site. This means that HCl, $H_2C_2O_4$ and HNO_3 show selectivity towards etching of Sr (SrO more basic than La_2O_3) and Ta (Ta_2O_5 more basic than iron oxides). This

coincides with the assumption that a basic compound reacts more readily with an acidic environment than an acidic compound will do (Section 2.4.4). The smallest change of internal A- and B-cation ratio was observed for HCl. In the case of H_2SO_4 the trend is that Ta is removed more readily than Fe. The reason for this is not clear.

All the etchants proved to etch all species in LSFT, although some selectivity was observed. This is based on the fact that all the surfaces were altered to such an extent that no specie could have been left without being etched. As noted in Section 2.4.3 a too high selectivity towards one specie may lead to significant altering of the surface properties. If the etching changes the (La,Sr)/(Fe,Ta)-ratio too much there are several other possible phases that may form as seen in the phase diagram in Figure 2.4. The sample etched in H_2SO_4 for 23 days was almost completely dissolved when the etching was aborted, leaving only a thin piece, much thinner than pellets from other experiments when they were aborted (Figure 4.10e and Figure 4.10f). The XRD-spectrum from this sample shows a shift of all the cubic perovskite peaks to lower angles. According to Bragg's law (Equation 2.6) this is caused by an increase of lattice plane spacing (d), hence it would be fair to assume that the atomic spacing in the material has increased. The fact that the overall crystal structure is retained show that the A/B cation ratio is maintained, but selective etching has altered the internal ratio of A-cations and B-cations. According to Table 4.3, which denotes EDS-results from primary surface point scans, etching in H_2SO_4 reduced the amount of Sr relative to La and Ta relative to Fe. Due to different cation radii (Table 5.1) this may lead to chemical expansion (Section 2.5.4), as further discussed below.

An enrichment of La at the A-site in the perovskite structure would lead to a decrease

Table 5.1: LSFT-cation radii with corresponding coordination number, CN [47]

Ion	CN	Radii, [nm]	Spin
La^{3+}	12	1.36	-
Sr^{2+}	12	1.44	-
Fe^{2+}	6	0.78	-
Fe^{3+}	6	0.645	-
Fe^{4+}	6	0.585	High
Ta^{5+}	6	0.64	High

of lattice parameters due to the lower ionic radii of La^{3+}. The percentage reduction of radii would be 5.6%. The substitution of divalent Sr with trivalent La must be accompanied by a reduction of the valence state of iron to retain the charge balance. A reduction

of iron would lead to an increase of lattice parameters as lower valence gives higher radii (Table 5.1). A reduction from 4+ → 3+ and from 3+ → 2+ gives a percentage increase of radii of 10.2% and 20.9%, respectively. From this a net increase of the lattice parameters could be expected. If oxygen stoichiometric LSFT is considered iron will have an average valence of 2.8, hence it is assumed that both reductions are possible. The relative Fe to Ta ratio on B-site is very uncertain because of the large error of Fe content from EDS. Assuming that the B sites are enriched on Fe the following considerations are relevant. When substituting Ta^{5+} with Fe there must be a mechanism in place to retain charge balance. One mechanism can be an electronic compensation by the oxidation of iron up to a maximum valence of 4+. This would lead to a decrease of lattice parameters. Another option is the formation of oxygen vacancies. These vacancies will not directly influence the lattice parameters, but may lead to the weakening of bonds as discussed in Section 2.5.4. This weakening of bonds will possibly give an increase of lattice parameters. The possible formation of oxygen vacancies as a charge compensating mechanism could explain why small gas bubbles were observed on the sample surface during etching in H_2SO_4, as O_2-gas would evolve. These bubbles were not observed for any of the other etchant solutions. In Section 2.1.1 it was mentioned that oxygen gas molecules would adsorb onto an oxygen vacancy site as part of the surface exchange reaction. If it is actually the case that etching with H_2SO_4 creates more oxygen vacancies near the surface, this would introduce an extra beneficial effect in addition to the increased surface area. More investigation would be required to determine the effect of this. The considerations discussed in this paragraph show that the etchants may induce microscopic effects in addition to the macroscopic effect of increased surface area that influence the overall effect of the surface structuring.

The secondary magnetoplumbite phase ($SrFe_{12}O_{19}$) is shown in the top right corner of Figure 4.10d and in Figure 4.15e (darker areas). In Figure 4.10d it is apparent that this phase was etched less than the primary phase. This is probably because it is very iron rich. Iron oxide is one of the more acidic oxides that can be formed from the LSFT-cations, and a lower reactivity with an acidic etchant is expected. The extensive etching around the secondary phase seen in Figure 4.15e could arise because of lattice stresses, as described in Section 2.5.2. A secondary phase will lead to strains at the interface between the primary and secondary phase giving a higher reactivity (Section 2.5.1). The presence of a secondary phase will accordingly be undesirable on the surface when doing surface structuring because it creates areas of increased or reduced etching which is hard to control.

Uniformity and Overall Surface Structure The uniformity of the sample surfaces after etching varies significantly with both etching time and concentration as shown i.e. by the experiments of differing HCl-concentrations (Figure 4.4 and Figure 4.5).

It is possible to use etching programs which leave the surface fairly uniform by using short etching times and lowered concentrations. The longer the sample is exposed to an etchant the more uneven the surface becomes because of surface voids, internal pores and secondary phases. This isotropic behaviour is a drawback for WCE as a mean for surface structuring because it limits the possibility of an even surface that still is etched fairly rough. As seen earlier, the presence of a secondary phase may leave a particle sticking out of the surface (Figure 4.10d) or the etchant may "dig" around it, causing the whole particle to fall out leaving a large hole (Figure 4.15e). Both these effects limits the control over the resulting morphology of the sample surface.

No significant differences were observed in the etching results from the different etchants with respect to macroscopic uniformity of the primary phase. The structure of the primary phase showed the same development starting with mid grain and grain boundary etching, followed by more severe etching down into the material. The grain boundary etching was as expected due to the elevated surface energy associated with grain boundaries (Section 2.5.2). The mid grain etching was on the other hand unexpected and is discussed further in Section 5.1.3. There were no signs of different etching behaviour on seemingly similar surfaces, i.e. primary surfaces were etched similarly on the whole surface of an investigated sample. The absence of morphology differences for the different etchant solutions make WCE a flexible method for surface structuring because the etchant can be chosen considering other factors than the resulting surface structure. This makes it easier to choose an etchant that does not produce precipitates or other undesirable effects. On the other hand it limits the WCE-technique's flexibility to alter the resulting surface morphology.

As pointed out in Section 2.2.1 mass transport can become an issue when doing chemical etching. Mass transport limitations were not observed (nor investigated specifically) in this work. When etching the sample used for ECR it was left on two thin glass cylinders to avoid this potential problem.

5.1.2 Effect of Anions

Differences were seen during etching with respect to changes to the etchant solutions used. This discussion is based solely on visual inspection of the solution and what was subsequently was observed with SEM, hence any colourless complexes and small amounts of precipitations may have been overlooked.

By taking into account the weight of a typical sample to be etched and the typical volume of etchant used for each experiment it is possible to calculate the maximum

concentration of cations given full dissolution of the sample;

$$C_{La} = C_{Ta} = 0.018M$$
$$C_{Sr} = C_{Fe} = 0.071M$$

Combining this with Equation 2.10 makes it possible to calculate the minimum concentration of anions needed to get precipitation. Given the information in Table 2.6 about solubility in 100g H_2O and in other solutions, the compounds listed in Table 5.2 stand out as possible precipitates (lower anion concentration needed for precipitation than what was introduced in the etchant solution). This table supports the assumption that

Table 5.2: Minimum anion concentration for precipitation of relevant species, aS = concentration of anions, i = insoluble

Formula	Mimimum bS	Formula	Mimimum bS
$La(OH)_3$	$8.5{\cdot}10^{-8}$M	$Fe(OH)_3$	i
$La_2(SO_4)_3$	$3.02{\cdot}10^{-1}$M	$FeCO_3$	$7.42{\cdot}10^{-4}$M
$La_2(CO_3)_3{\cdot}8H_2O$	i	$Fe(OH)_2$	$1.05{\cdot}10^{-7}$M
FeO(OH)	i	$SrSO_4$	$7.72{\cdot}10^{-6}$M

$SrSO_4$ precipitated during etching with H_2SO_4. The white colour of the precipitate also corresponds to $FeSO_4$, but the solubility of $FeSO_4$ is too high. Precipitation of $SrSO_4$ has also been observed in similar etching experiments elsewhere [20]. The bubbles observed on the pellet etched in H_2SO_4 could stem from oxygen evolution as discussed for selectivity in Section 5.1.1. The yellow colour formed almost immediately when etching in HCl was probably caused by the complex ion $FeCl_4^-$. It is not clear what compound produced the subsequent red/brown colour, but the final yellowish precipitate may be $Fe(OH)_3$. No likely precipitate or complex has been identified to cause the visually observed changes to the etchant solution when etching with HNO_3. Nitrates in general have a very high solubility in aqueous solutions. The main issue when etching with HNO_3 was the precipitation of tantalum oxide that covered most of the surface, observed with SEM. The composition of this tantalum oxide is hard to determine because it does not show up on XRD. There are several tantalum oxide compounds that have similar XRD-peaks as the primary cubic perovskite phase, but the composition of these does not coincide with what has been found by EDS [68, 69]. Tantalum oxide is also known to exist in an amorphous hydrated state, which may explain why it does not show up on XRD [34]. According to the EDS-measurements discussed in Section 4.2.2 the composition corresponds to $TaO_{\sim 3.24}$. Without any further investigations of this it is not possible to determine the exact composition of the precipitate. It is nor clear why the tantalum oxide precipitate was seen only after etching with HNO_3 and not after i.e. HCl and H_2SO_4 which are the two etchant that most resemble HNO_3 with respect to etch

rate. Possible explanations could be that Ta is bound up in a precipitate of complex that was not found by visual inspection when etching with HCl and H_2SO_4. This would lead to a lower Ta^{5+}-concentration in the solution making the precipitation of tantalum oxide more difficult. It is apparent that the type of anion present in the solution is important for the extent of complexing and precipitation observed during etching. The differences highlighted above show that it is important when designing an etching experiment to select an etchant that interacts as little as possible with the dissolved species from the sample.

5.1.3 Mid Grain Etching

All the etchant solutions used that showed etching capability also showed mid grain etching behaviour. Mid grain etching it self is a desirable effect when doing surface structuring of materials with WCE. Although the underlying reason causing mid grain etching possibly is undesirable, the mid grain etching does lead to an increased surface area relative to samples without mid grain etching. As observed on samples without mid grain etching it is mainly the grain boundaries that are etched. This makes the increased surface area very dependent on the grain size and microstructure of the material. The effect of WCE will hence decrease with an increasing grain size of the etched material. The reason for the mid grain etching behaviour is not clear, but some considerations follow in the subsequent paragraphs.

The mid grain etching seem to be more severe in some grains than others. This difference was apparently irrespective of grain size as is clearly shown in Figure 4.12a and Figure 4.12b. It is also apparent from the two figures that the grain centres are more reactive than the grain boundaries. This is not so obvious for the etchants with high etch rate, but hints of this can be seen when examining the samples etched in reduced HCl-concentrations for short times (Figure 4.4 and Figure 4.5). In most cases the mid grain etching was observed to be fairly symmetrical oriented around the grain centre. This implies that the effect leading to this mid grain etching is something affecting the grain in the same extent from all sides. The existence of such an effect is supported by what is seen when comparing etching of a polished surface with a non-polished surface. The surface of a polycrystalline pellet prior to polishing will consist of some grains that are abraded only a little and some that are abraded all the way to the grain centre. Because of this the part of the grain exposed to the etchant solution will differ and the apparent reactivity of each grain will be different. This is illustrated by comparing Figure 4.4d, which shows a polished and etched surface and Figure 4.7e, which shows the unpolished backside of the same pellet. In the latter micrograph the amount of mid grain etching is much less pronounced and it looks like the etching is mainly along grain boundaries and evenly distributed over each grain. The observed even etching of each grain may be because of i.e. a stress gradient in the grain (see subsequent paragraph). The grain

surface exposed to the etchant solution would then be subject to the same stress all over the surface. Such an even stress distribution does not allow for any difference in etch rate on different parts of the grain.

Oxygen content is an effect that could influence each grain in a similar extent from all sides. As discussed in Section 2.5 the oxygen diffusion along a grain boundary is faster than in the lattice. If the cooling from T_{max} during sintering is done too fast, the lattice may be unable to absorb an equilibrium amount oxygen compared to what it would have absorbed if cooling had been done at an "equilibrium rate". The result of such a cooling regime could be an oxygen-enriched region along the grain boundary and an oxygen deficiency in the grain centre. The size of this oxygen gradient has not been estimated and would depend on the degree of oxygen transport into the bulk along grain boundaries compared to lattice diffusion from grain boundaries into the grains. The $\nabla\mu_{O_2}$ may explain some of the observations made during this work such as the reduced mid grain etching seen after increasing sintering time and temperature (Sintering program A; 1175°C, 1 hour → Sintering program B; 1350°C, 2 hours). Larger grains would lead to a lower $\nabla\mu_{O_2}$ due to the increased distance from the oxygen deficient grain centre to the grain boundary. A grain boundary diffusion of oxygen assumed to be very fast compared to lattice diffusion would imply that the grain boundaries are at equilibrium at all times, while the slow lattice diffusion sets the grain centres at non-equilibrium state. This supports the observation of no significant difference between mid grain etching in the middle of the sample and close to the surface (Figure 4.7). Both grains near the surface and in the middle of the sample will have the same access to oxygen along the grain boundaries and subsequently the same $\nabla\mu_{O_2}$ in each grain.

Exploring the effect of such an oxygen potential gradient presents two options;

Kinetic Demixing (Section 2.5.3) If the gradient leads to kinetic demixing it is expected that the grain boundary region is enriched on selected species with a corresponding depletion in the grain centre. According to Section 2.5.3 Sr and Fe will diffuse towards a high oxygen potential faster than La and Ta leaving the grain boundaries enriched on Sr and Fe. This does not coincide very well with the etchant selectivity discussed earlier (Section 5.1.1). It was seen for nearly all etchants that the Sr-content found with EDS-analysis decreased because of the etching. If kinetic demixing led to an Sr- and Fe-enrichment of the grain boundary region, the grain boundary region would have been etched even more readily than without kinetic demixing. A corresponding stabilisation of the grain centre should then also be observed, contrary to what was observed from the herein described experiments.

For kinetic demixing to occur the oxygen potential gradient would have to withstand

for a long time. Earlier experiments on LSF have shown that kinetic demixing is a slow process, even at temperatures above 1000°C [46]. The pellets showing mid grain etching in this work was held at T_{max} for 1 hour, and then cooled down to room temperature in about 6 days. The oxygen diffusion may at some point be seen as frozen, hence the oxygen potential gradient will withstand. Cation diffusion is generally much slower than oxygen diffusion in MIEC-materials and will be frozen long before the oxygen diffusion. This implies that only little demixing is possible due to mass transport limitations and that kinetic demixing is probably not the cause of the mid grain etching.

Chemical Expansion (Section 2.5.4) Chemical expansion is another possible explanation for the observed mid grain etching caused by an oxygen potential gradient. This chemical expansion, caused by an elevated oxygen content, would lead to a lattice expansion in the grain boundary region of a grain. If the grain is pictured as a sphere, the expansion would impose a tensile stress in a "shell" around the grain centre. This tensile stress would decrease inwards, and in the grain centre be balanced by a compressive stress (negative tensile stress). The transition between tensile and compressive stress would be at a certain distance from the grain centre forming a sphere where the lattice is completely relaxed and tensile stresses are zero. The radius of this "sphere of zero stress" does not have to be exactly half the radius of the whole grain, as seen in Figure 2.8. This may explain why the observed mid grain etching varies with respect to how far it etches from the grain centre in radial direction. The reactivity of this relaxed sphere will be lower than the grain centre and the outer surface explaining the "cup-like" grains seen in i.e. Figure 4.5e. Chemical expansion is seen as a more likely cause for the mid grain etching than the kinetic demixing discussed above.

5.2 Secondary Iron Rich Phase

A secondary phase seen in all pellets made during this work is most likely magnetoplumbite ($SrFe_{12}O_{19}$). The composition corresponds well with what was seen from EDS-analysis of the phase (Table 4.4), and XRD-data from literature (Figure 4.14)[67]. The occurrence of the phase probably stems from a slight off stoichiometry of cations in the LSFT-powder. The phase diagram in Figure 2.4 shows that a surplus of B-site cations (Fe and Ta) is needed to get precipitation of magnetoplumbite. The EDS-analysis of unetched samples used in this work show the opposite case, where both the content of Fe and Ta is lower than the stoichiometric amount. There is though a small standard deviation for Sr and Fe leaving the possibility for Fe-surplus open.

The magnetoplumbite phase change morphology with the sintering temperature and time (see Figure 4.15a and Figure 4.15b). This is probably because of a preferred directional growth direction that is easier to access at higher temperatures because of the

increased cation diffusion. This is also apparent when examining the phase at the surface on an unpolished pellet where relatively large flakes seem to grow up from the surface (Figure 4.15d). The larger particles laying horizontal on the surface grow in a layered manner perpendicular to the surface, also showing preferred growth direction.

Relative to the primary LSFT-phase magnetoplumbite seem to have a larger etch resistivity (as discussed in Section 5.1.1). Although the amount of secondary phase is limited it is not preferable to have it present. In some cases it causes large voids/pits in the surface because the etchant etches around it, making it harder to control the resulting morphology from a given etch program. The phase has also been suspected to have poorer oxygen permeability properties than the primary phase [46]. This means that the ECR-experiments done in this work may have been affected by it, although the effect is thought to be very small.

5.3 CO_2-exposure

The goal of the high temperature CO_2-exposure reported in this work was to grow a thin layer of $SrCO_3$ on the surface of a membrane, and subsequently remove it using thermal decomposition or chemical etching. Such growth has been demonstrated earlier with growth of a several μm thick layer of $SrCO_3$ on an LSF-related substrate [5]. In this work attempts were made to grow carbonate at 900°C and 1000°C. This was only partly successful.

5.3.1 Characterization

All XRD-spectra obtained prior to the CO_2-experiments appear to show purely cubic perovskite phase, hence no definite proof of carbonate formation as a consequence of the CO_2-exposure has been obtained (Figure 4.18). Indications were though found using EDS (Table 4.5). A general increase of carbonate content in the primary phase was observed with EDS. Some small areas on the surface also show the appearance of a secondary phase. This phase was found to contain elevated levels of carbon and strontium, as would be expected for an $SrCO_3$ phase. Based on these observations it is assumed that $SrCO_3$ formed on the surface, though to a very small extent.

Due to time limitations it was not possible to investigate if the elevated levels of carbon on the primary surface was due to a very thin layer of carbonate. No such layer was observed when examining the cross section of the exposed samples, but this could be because it was to thin (Figure 4.16d and Figure 4.17f). If such a layer had formed it would coincide very well with the intention of the experiment. Emphasis was put on obtaining a thin carbonate layer when choosing experimental parameters, rather than producing a layer several μm thick. In this way the surface structuring obtained when

the carbonate eventually is removed will be very fine, leaving a large increase of surface area.

5.3.2 Thermodynamic Stability

The amount of $SrCO_3$ formed during the 900°C experiments was very limited, close to nothing. The amount increased a little when the temperature was increased to 1000°C. From the thermodynamic stability considerations regarding SrO and $SrCO_3$ in Section 2.6 it is apparent that the activity of SrO is an important factor influencing the stability regions of the two compounds. It is believed that the activity of SrO is one of the factors causing the limited carbonate growth. The assumption that $a_{SrO} = 0.4$ will give a transition from $SrCO_3$ stabilization to SrO stabilization above 1074°C while $a_{SrO} = 0.1$ sets this transition at 977°C (given $p_{tot} = p_{CO_2} = 1$ atm). The more likely of the two activities will be $a_{SrO} = 0.1$ and hence the experimental conditions does not favour carbonate formation at 1000°C. This is probably one of the reasons for the limited carbonate growth seen at 1000°C. The same method that led to the above given temperature limits for thermodynamic stability of $SrCO_3$ can be used to find a_{SrO} if the transition from $SrCO_3$ to SrO were to happen at 900°C. This would happen if $a_{SrO} \approx 0.045$. The proximity of this activity to the above estimated ones in combination with the observed low carbonate growth at 900°C makes lacking thermodynamic stability of $SrCO_3$ a probable cause for the lacking growth of carbonate observed in this work.

5.3.3 Experimental Time and Atmosphere

The temperatures, times and atmospheres for the CO_2-experiments were chosen based on previous work reported elsewhere [5]. In general the exposure times of the previous work were longer and the pressures were higher than they were in this work. Due to experimental setup limitations, p_{tot} of the herein described experiments was limited to 1 atm. This limitation significantly reduces the activity of each gaseous specie in the system, indicating a need for longer reaction times to obtain the same conversion level of SrO to $SrCO_3$. A slight increase of the amount of carbonate formed on the surface when increasing the experiment duration from 1 to 96 hours at 900°C with $p_{CO_2} = 1$ atm was observed, but 96 hours was apparently not enough to cover the entire sample surface.

It has been observed earlier that adding water vapour to the CO_2 atmosphere significantly increases the rate of carbonate formation. In this work water vapour was added to the dry CO_2-gas by bubbling the gas through water at room temperature. No eminent effect was observed from this. The low thermodynamic stability discussed in the above paragraph could be one reason for this. By adding water vapour to a system of fixed $p_{tot} = 1$ atm will evidently reduce the partial pressure of CO_2. This reduction will move

the system further towards thermodynamic stability of SrO. Due to the simple setup of this experiment, p_{H_2O} is limited to the solubility of H_2O(g) in CO_2 at room temperature (as denoted in Figure 2.10). In the previously reported experiments the ratio p_{H_2O} / p_{CO_2} >3 with a total pressure (including inert gas) above 7 bar in most cases [5]. For the herein reported experiments the ratio was p_{H_2O} / p_{CO_2} ≤ 0.03 depending on the degree of saturation that was actually achieved by the bubbling, and p_{tot} = 1 atm. These pressure differences give a significantly lower activity of each gaseous specie in the herein described experiments, contributing to a lesser growth of carbonate. No formation of $Sr(OH)_2$ was observed, as would be expected from the calculations for Figure 2.10

In conclusion there were probably several factors leading to the failure of these CO_2-experiments. A combination of erroneous assumptions regarding the interplay between a_{SrO}, experiment duration and p_{CO_2} led to the limited carbonate growth observed.

5.4 Effect of Surface Structuring on k_{chem}

The effect of surface structuring in literature is mostly reported as an observed improvement of j_{O_2} relative to a membrane without surface structuring [6, 13, 14, 17, 18, 20]. This method gives a good view of the end result, but does not allow for individual study of diffusion and surface exchange separately. As noted earlier in Section 2.1 surface structuring should only alter the surface exchange rate of the membrane. If a significant change of D_{chem} is observed in addition, it may imply a more extensive structural change because of the structuring.

The specific surface area of the ECR-sample increased 3.6 times relative to a polished sample as a consequence of the surface structuring done in HCl before the ECR-measurements. This lead to an improvement of k_{chem} by a factor of about half an order of magnitude for both oxidation and reduction runs at 800°C, and for the reduction run at 900°C (see Table 4.7). It is evident that the improvement of k_{chem} almost scales with the increase of surface area. As stated in Section 2.2.3, a direct scaling is to be expected if the oxygen transport is limited solely by surface exchange, when L_c >L. Appendix E shows calculated L_c-values from this ECR-experiment. It is evident that these L_c-values are smaller than the sample dimensions in Table 3.6 (where L = l_y and l_z) meaning that the criteria for direct scaling is not present. Calculation of L_i by Equation 2.29 also shows that oxygen transport is in the mixed regime, limited by both D_{chem} and k_{chem} (the first criterion in Section 2.7). The lack of scaling could also reflect the slight altering of the chemical composition due to etching, as discussed in Section 5.1.1.

There are some different developments of the improvement of k_{chem} worth commenting. Disregarding the oxidation run at 800°C, all series of Δk_{chem} show an increasing effect of surface structuring with decreasing p_{O_2}. This is reasonable because at a lower

p_{O_2} the density of oxygen molecules in the gas phase is lower. For a given surface area, the likelihood of an oxygen molecule hitting an adsorption site on the surface decreases with decreasing p_{O_2}. By increasing the number of adsorption sites the probability of an oxygen mole hitting an adsorption site increases, and this is more effective at lower p_{O_2} as reflected by the results reported here. The temperature dependency of the k_{chem} found in this work can be assumed to follow the expected trend of decreasing effect with increasing temperature when taking into account experimental errors. While the development of Δk_{chem} at 800°C for oxidation and reduction steps are within each other's standard deviations, this is not the case at 900°C. At 900°C a significant splitting of Δk_{chem} can be observed at the lower p_{O_2}-values. It is not clear why this difference is observed.

k_{chem} was obtained using ECR at 800°C and 900°C after surface structuring of the sample with 6M HCl for 15 minutes. This treatment was chosen because it led to significant structuring of the surface, but at the same time kept a relatively plain surface without large voids or holes. Only one sample was tested so it is not experimentally determined if this was the best structuring treatment. To determine this would require a larger testing program using ECR. This is because a simple measurement of the specific surface area with varying degree of etching does not take into account any gas flow implications of extended etching, nor does it include any surface area "hidden" below grains which the gas may see, but the AFM cannot see. It is also apparent, as discussed above, that the oxygen transport is limited by both diffusion and surface exchange, hence a doubling of surface area from increased etching will not lead to a doubling of k_{chem}.

As can be seen in Figure 4.21 the D_{chem}-values of the surface structured and the polished sample coincide well at the higher p_{O_2}s and it is assumed that D_{chem} has not been changed within the experimental error as a consequence of the etching. The D_{chem}-values at lower temperatures are neglected because at low p_{O_2}s, surface exchange will dominate oxygen transport, making the D_{chem}-values less accurate.

5.5 Chemical Etching vs. other Surface Structuring Techniques

It is important to compare the WCE technique used in this work with other techniques to determine the applicability of either. WCE is a very simple technique that can be utilized without access to expensive or complicated equipment. The equipment needed for WCE only includes basic lab ware found in any chemical laboratory. The simplicity though also limits the possibilities to influence the result. As discussed in Section 5.1.3 the result is very dependent on microstructure and it is to some extent vulnerable to selectivity of the etchant. Mechanical abrasion, described in Section 2.2.1, is also a very simple technique without large equipment requirements. This method may though be limited by the mechanical stresses it exposes the membrane to. This will become an

issue as membranes become thinner and by that, increasingly fragile. Porous coating of the dense membrane is a more complex method, but it has its advantages. The effect of is determined to a large extent of the porosity and pore wall surface area, which to a large extent can be tailored.

No data have been found in the literature that are directly comparable with the results obtained in this work. This is mainly because the literature data investigate improvement of j_{O_2}, and not D_{chem} and k_{chem} as was done here [6, 13, 14, 17, 18, 20]. This being said, some comparisons are possible. The normalized surface area, N_{sa}, of the sample used for ECR was 3.96. This is about 25% higher than what has been obtained using mechanical abrasion with a #80 emery paper [13]. Increasing the etching time and/or the etchant concentration would probably increase N_{sa} further, but at the cost of uniformity. It should be remembered that the surface area observed by the gas surrounding the sample will probably be larger than what can be found by AFM due to the AFM's inability to measure beneath an overhang, i.e. a grain, as described in Section 2.3.1.

If the assumption is made that oxygen transport during the ECR-experiment was solely limited by surface exchange (though wrong, see Section 5.4) Equation 2.24 could be used to link the k_{chem} measured in this work with j_{O_2}. The same assumption dictates that j_{O_2} will scale directly with the increase of k_{chem} obtained by surface structuring. This allows for a comparison of the effectiveness of WCE for surface structuring to that of porous layers and mechanical abrasion seen in Section 2.2.1. Given the assumption above a permeation improvement factor of $\alpha \approx 3$ has been achieved in this work. This α is larger than almost all the values from literature listed in Section 2.2.1 for both porous layers and mechanical abrasion. The lowest α obtained is 1.9 (900°C, reduction, p_{O_2} = 0.066 atm), which still is a very good result. The highest α from this work is 4.6 (900°C, oxidation, p_{O_2} = 0.002 atm). These observations leave chemical etching as a very viable alternative for surface structuring of membranes for gas separation. This being said much of this result is seen because of the mid grain etching and cannot be extrapolated as the case for WCE in general. The effect of WCE is very dependent on microstructure, and would in this work be much lower if all etched surfaces had the structure of the pellets sintered at higher temperature (Figure 4.6).

No data has been found in literature describing similar etching experiments as has been done in this work. The closest is the experiments with HCl and H_2SO_4 described in Section 2.2.1. There HCl and H_2SO_4 was used to increase j_{O_2} of hollow fibres and the highest α reported was 18.6. It is though likely that much of the reported improvement stem from the opening of closed pores surrounding a dense layer, and not the etching itself.

The overall goal with this work was to achieve "nanostructuring" of a membrane surface using chemical etching. This has to some extent been achieved because of the mid grain etching which was observed. The thickness of some of the thinner walls of the "cup-like" grains observed after etching is below 100 nm. This being said, the etch result after WCE is very dependent on grain size and microstructure and cannot in general be extrapolated to give a nanostructured surface. For a surface of grains without gradients the etchant solution will mainly attack the grain boundaries, as seen in this work for the samples sintered at higher temperature (Figure 4.6). This is a major limitation of WCE as a technique for nanostructuring of surfaces.

6 Further Work

To truly investigate and find the potential of WCE, further studies should be done with respect of the optimal etching program. In this work, only one sample was tested using ECR after being etched in 6M HCl for 15 minutes. A longer etching time will yield a higher specific surface area, at the expense of increased roughness. Whether this is beneficial for the overall effect, bearing in mind the possible gas transport limitations, should be investigated. It should also be investigated if the lattice expansion observed after etching with H_2SO_4 is beneficial for the surface exchange properties.

The experiments with CO_2-exposure should also be investigated further. It is still believed that the formation and subsequent removal of $SrCO_3$ can lead to a random, but very fine surface structuring, possibly on a very small scale. More experiments should be done where the experimental parameters are tuned to ensure thermodynamic stability of $SrCO_3$. Such tuning may include lowering the temperature and / or increasing p_{CO_2} and p_{H_2O}.

To make WCE applicable for nanostructuring of surfaces, the elevated reactivity of grain boundaries must be dealt with. Lithography was investigated as a possibility during this work but it was not tested experimentally due to equipment limitations. If lithography is used the surface can be covered with a resist in a given pattern limiting the etchant solutions access to the grain boundaries, and forcing the etching of bulk grain surfaces. Another option is to combine WCE with i.e. mechanical abrasion. Pre-structuring a surface using emery paper and subsequently etching it may give an extra effect as chemical etching is seen to give higher increase of specific surface area than mechanical abrasion alone.

7 Conclusions

The surface of a $La_{0.2}Sr_{0.8}Fe_{0.8}Ta_{0.2}O_{3-\delta}$ membrane has successfully been structured using wet chemical etching. Factors found to be important when choosing etchant for WCE were;

- etch rate - to ensure a fast procedure, favoured by low pH
- etchant anion - to prevent re-precipitation on the surface
- etchant selectivity - to prevent i.e. chemical expansion near the surface

HCl was found to be the best etchant for LSFT with the highest etch rate, the lowest degree of selectivity and no undesirable anion effects. All the seven etchant solutions investigated (HCl, HNO_3, H_2SO_4, $H_2C_2O_4$, $NaHCO_3$, Na_2CO_3 and KOH) gave the same type of surface morphology given enough time except KOH, which did not etch at all. Etching of grain boundaries was observed, as expected, but also mid grain etching was seen, leaving "cup-like" grains after etching. This is thought to be because of an oxygen potential gradient inside each grain causing chemical expansion. The mid grain etching was severely reduced by a higher sintering temperature for the sample. The mid grain etching it self is a positive effect with respect to increasing surface area, though it is not known whether the underlying cause for this behaviour is beneficial for the overall oxygen transport through the material. As it cannot be assumed that all materials possess this internal gradient in each grain, grain boundary etching will dominate and the overall effect of WCE will depend much on the microstructure of the specific material to be etched. An increase of lattice parameters was observed after etching in H_2SO_4, probably caused by selective etching leading to chemical expansion. The subsequent effect of this expansion on oxygen surface exchange kinetics has not been determined.

ECR was used to investigate the effect of the surface structuring by WCE. An increase of specific surface area 3.6 times gave an increase of k_{chem} about 3.16 times at 800°C. The lack of direct scaling between k_{chem} and the increase of surface area is probably due to oxygen transport being controlled by both surface exchange and bulk diffusion. The effect of surface structuring decreased as expected with increasing temperature and increasing p_{O_2}. The change of D_{chem} was negligible. The results obtained by ECR cannot be directly compared with results in the literature because the literature data found measures j_{O_2}. This being said WCE stands out as a very simple and effective method. The modest etching of the ECR sample gave a 25% higher increase of specific surface area than what can be obtained by mechanical abrasion (#80 emery paper). This can easily be increased further by increasing the etching time, leaving WCE as a flexible technique for surface structuring.

Attempts were made to grow $SrCO_3$ on the membrane surface by exposing it to CO_2 at 900°C and 1000°C. The objective was to cover the whole surface with $SrCO_3$ before subsequently removing it, and in this way obtaining a structured surface. The amount formed, of what is assumed to be $SrCO_3$, was very small and did only cover small spots of the surface. The low amount is probably due to low activity of SrO and CO_2 combined with a too high temperature favouring the thermodynamic stability of SrO.

References

[1] H. J. M. Bouwmeester and P. J. Gellings. *The CRC handbook of solid state electrochemistry*. CRC Press, Boca Raton, Fla., 1997.

[2] H. J. M. Bouwmeester. Dense ceramic membranes for methane conversion. *Catalysis Today*, 82(1-4):141, 2003.

[3] H. J. M. Bouwmeester, H. Kruidhof, and A. J. Burggraaf. Importance of the Surface Exchange Kinetics as Rate-Limiting Step in Oxygen Permeation through Mixed-Conducting Oxides. *Solid State Ionics*, 72:185–194, 1994.

[4] J. E. tenElshof, H. J. M. Bouwmeester, and H. Verweij. Oxygen transport through $La_{1-x}Sr_xFeO_{3-\delta}$ membranes .2. Permeation in air/CO, CO_2 gradients. *Solid State Ionics*, 89(1-2):81–92, 1996.

[5] I. Kaus, K. Wiik, B. Krogh, M. Dahle, K. H. Hofstad, and S. Aasland. Stability of $SrFeO_3$-based materials in H_2O/CO_2-containing atmospheres at high temperatures and pressures. *Journal of the American Ceramic Society*, 90(7):2226–2230, 2007.

[6] T. Kida, S. Ninomiya, K. Watanabe, N. Yamazoe, and K. Shimanoe. High Oxygen Permeation in $Ba_{0.95}La_{0.05}FeO_{3-\delta}$ Membranes with Surface Modification. *Acs Applied Materials & Interfaces*, 2(10):2849, 2010.

[7] H. H. Wang, H. Q. Jiang, S. Werth, T. Schiestel, and J. Caro. Simultaneous Production of Hydrogen and Synthesis Gas by Combining Water Splitting with Partial Oxidation of Methane in a Hollow-Fiber Membrane Reactor. *Angewandte Chemie-International Edition*, 47(48):9341, 2008.

[8] R. Bredesen and J. Sogge. Paper presented at: The United Nations economic commission for Europe seminar on Ecological applixations of innovative membrane technology in chemical industry. Chem/Sem. 21/R.12, Cetaro, Calabria, Italy, 1-4 May 1996 .

[9] H. H. Wang, H. X. Luo, Y. Y. Wei, H. Q. Jiang, W. H. Yuan, Y. X. Lv, and J. Caro. Performance of a ceramic membrane reactor with high oxygen flux Ta-containing perovskite for the partial oxidation of methane to syngas. *Journal of Membrane Science*, 350(1-2):154, 2010.

[10] J. Santiso and M. Burriel. Deposition and characterisation of epitaxial oxide thin films for SOFCs. *Journal of Solid State Electrochemistry*, 15(5):985, 2011.

[11] H. Scott Fogler. *Elements of chemical reaction engineering*. Prentice-Hall PTR, Upper Saddle River, N.J., 2005.

[12] M. Mosleh, M. Sogaard, and P. V. Hendriksen. Kinetics and Mechanisms of Oxygen Surface Exchange on $La_{0.6}Sr_{0.4}FeO_{3-\delta}$ Thin Films. *Journal of the Electrochemical Society*, 156(4):B441, 2009.

[13] H. Kusaba, Y. Shibata, K. Sasaki, and Y. Teraoka. Surface effect on oxygen permeation through dense membrane of mixed-conductive LSCF perovskite-type oxide. *Solid State Ionics*, 177(26-32):2249, 2006.

[14] F. M. Figueiredo, V. V. Kharton, A. P. Viskup, and J. R. Frade. Surface enhanced oxygen permeation in $CaTi_{1-x}Fe_xO_{3-\delta}$ ceramic membranes. *Journal of Membrane Science*, 236(1):73, 2004.

[15] Y. Teraoka, H. M. Zhang, S. Furukawa, and N. Yamazoe. Oxygen Permeation through Perovskite-Type Oxides. *Chemistry Letters*, (11):1743, 1985.

[16] Ivar Wærnhus. *Defect Chemistry, Conductivity and Mass Transport Properties of $La_{1-x}Sr_xFeO_{3-\delta}$ (x = 0 and 0.1)*. PhD thesis, Norwegian University of Science and Technology, 2003.

[17] T. H. Lee, Y. L. Yang, A. J. Jacobson, B. Abeles, and S. Milner. Oxygen permeation in $SrCo_{0.8}Fe_{0.2}O_{3-\delta}$ membranes with porous electrodes. *Solid State Ionics*, 100(1-2):87, 1997.

[18] V. V. Kharton, A. Kovalevsky, A. A. Yaremchenko, F. M. Figueiredo, E. N. Naumovich, A. L. Shaulo, and F. M. B. Marques. Surface modification of $La_{0.3}Sr_{0.7}CoO_{3-\delta}$ ceramic membranes. *Journal of Membrane Science*, 195(2):277, 2002.

[19] S. Lee, K. S. Lee, S. K. Woo, J. W. Kim, T. Ishihara, and D. K. Kim. Oxygen-permeating property of $LaSrBFeO_3$ (B=Co, Ga) perovskite membrane surface-modified by $LaSrCoO_3$. *Solid State Ionics*, 158(3-4):287, 2003.

[20] Z. G. Wang, H. Liu, X. Y. Tan, Y. G. Jin, and S. M. Liu. Improvement of the oxygen permeation through perovskite hollow fibre membranes by surface acid-modification. *Journal of Membrane Science*, 345(1-2):65, 2009.

[21] H. M. Deng, M. Y. Zhou, and B. Abeles. Transport in Solid Oxide Porous-Electrodes - Effect of Gas-Diffusion. *Solid State Ionics*, 80(3-4):213, 1995.

[22] H. M. Deng, M. Y. Zhou, and B. Abeles. Diffusion-Reaction in Mixed Ionic-Electronic Solid Oxide Membranes with Porous-Electrodes. *Solid State Ionics*, 74 (1-2):75, 1994.

[23] S. Yakovlev, C. Y. Yoo, S. Fang, and H. J. M. Bouwmeester. Phase transformation and oxygen equilibration kinetics of pure and Zr-doped $Ba_{0.5}Sr_{0.5}Co_{0.8}Fe_{0.2}O_{3-\delta}$ perovskite oxide probed by electrical conductivity relaxation. *Applied Physics Letters*, 96(25), 2010.

[24] E. Girdauskaite, H. Ullmann, V. V. Vashook, U. Guth, G. B. Caraman, E. Bucher, and W. Sitte. Oxygen transport properties of $Ba_{0.5}Sr_{0.5}Co_{0.8}Fe_{0.2}O_{3-x}$ and $Ca_{0.5}Sr_{0.5}Mn_{0.8}Fe_{0.2}O_{3-x}$ obtained from permeation and conductivity relaxation experiments. *Solid State Ionics*, 179(11-12):385–392, 2008.

[25] E. Bucher, A. Egger, P. Ried, W. Sitte, and P. Holtappels. Oxygen nonstoichiometry and exchange kinetics of $Ba_{0.5}Sr_{0.5}Co_{0.8}Fe_{0.2}O_{3-\delta}$. *Solid State Ionics*, 179 (21-26):1032–1035, 2008.

[26] P. Ried, E. Bucher, W. Preis, W. Sitte, and P. Holtappels. Characterisation of $La_{0.6}Sr_{0.4}Co_{0.2}Fe_{0.8}O_{3-\delta}$ and $Ba_{0.5}Sr_{0.5}Co_{0.8}Fe_{0.2}O_{3-\delta}$ as Cathode Materials for the Application in Intermediate Temperature Fuel Cells. *ECS Transactions*, 7(1): 1217–1224, 2007.

[27] M. Burriel, C. Niedrig, W. Menesklou, S. F. Wagner, J. Santiso, and E. Ivers-Tiffée. BSCF epitaxial thin films: Electrical transport and oxygen surface exchange. *Solid State Ionics*, 181(13-14):602 – 608, 2010.

[28] Philippe. Marcus and Florian B. Mansfeld. *Analytical methods in corrosion science and engineering*. CRC Press, Boca Raton, 2006.

[29] Michael Quirk and Julian Serda. *Semiconductor manufacturing technology*. Prentice Hall, Upper Saddle River, N.J., 2001.

[30] Jarle Hjelen. *Scanning elektron-mikroskopi*. SINTEF, Trondheim, 1989.

[31] Tudor E. Jenkins. *Semiconductor science : growth and characterization techniques*. Prentice Hall, New York, 1995.

[32] Svein Stølen, Tor Grande, and Neil L. Allan. *Chemical thermodynamics of materials: macroscopic and microscopic aspects*. Wiley, Chichester, 2004.

[33] William M. Haynes, editor. *CRC Handbook of Chemistry and Physics*. CRC Press, 91st edition, 2010-2011.

[34] Marcel Pourbaix. *Atlas of electrochemical equilibria in aqueous solutions*. National Association of Corrosion Engineers, Houston, Texas, 2nd english edition, 1974.

[35] Gordon H. Aylward and Tristan J. V. Findlay. *SI Chemical Data*. J. Wiley, Sydney ; New York, 6th edition, 2008.

[36] V. Diniz and B. Volesky. Effect of counterions on lanthanum biosorption by Sargassum polycystum. *Water Research*, 39(11):2229, 2005.

[37] J. F. Rabek, J. Lucki, H. Kereszti, B. Krische, B. J. Qu, and W. F. Shi. Polymerization of Pyrrole on Polyether, Polyester and Polyetherester Iron(iii) Chloride Coordination-Complexes. *Synthetic Metals*, 45(3):335, 1991.

[38] Duward F. Shiver, Peter W. Atkins, Tina Overton, Jonathan Rourke, Mark Weller, and Fraser Armstrong. *Inorganic chemistry*. Oxford university Press, Great Clarendon Street, Oxford OX2 6DP, 4th edition, 2006.

[39] H. X. Luo, Y. Y. Wei, H. Q. Jiang, W. H. Yuan, Y. X. Lv, J. Caro, and H. H. Wang. Performance of a ceramic membrane reactor with high oxygen flux Ta-containing perovskite for the partial oxidation of methane to syngas. *Journal of Membrane Science*, 350(1-2):154, 2010.

[40] William D. Callister. *Materials science and engineering : an introduction*. John Wiley & Sons, New York, 7th edition, 2007.

[41] H. L. Lein, K. Wiik, and T. Grande. Kinetic demixing and decomposition of oxygen permeable membranes. *Solid State Ionics*, 177(19-25):1587, 2006.

[42] A. Fossdal, M. A. Einarsrud, and T. Grande. Phase relations in the pseudo-ternary system La_2O_3-SrO-Fe_2O_3. *Journal of the American Ceramic Society*, 88(7):1988, 2005.

[43] I. J. McColm and N. J. Clark. *Forming, shaping, and working of high performance ceramics*. Blackie ;Chapman and Hall, Glasgow, New York, 1988.

[44] A. Martin. Materials in thermodynamic potential gradients. *Journal of Chemical Thermodynamics*, 35(8):1291, 2003.

[45] S. Royer, D. Duprez, and S. Kaliaguine. Role of bulk and grain boundary oxygen mobility in the catalytic oxidation activity of $LaCo_{1-x}Fe_xO_3$. *Journal of Catalysis*, 234(2):364, 2005.

[46] Hilde Lea Lein. *Mechanical properties and phase stability of oxygen permeable membranes* $La_{0.5}Sr_{0.5}Fe_{1-x}Co_xO_{3-\delta}$. PhD thesis, Norwegian University of Science and Technology, 2005.

[47] R. D. Shannon. Revised Effective Ionic-Radii and Systematic Studies of Interatomic Distances in Halides and Chalcogenides. *Acta Crystallographica Section A*, 32(Sep1):751–767, 1976.

[48] P. V. Hendriksen, P. H. Larsen, M. Mogensen, F. W. Poulsen, and K. Wiik. Prospects and problems of dense oxygen permeable membranes. *Catalysis Today*, 56(1-3):283, 2000.

[49] F. J. Gotor, M. Macías, A. Ortega, and J. M. Criado. Comparative study of the kinetics of the thermal decomposition of synthetic and natural siderite samples. *Physics and Chemistry of Minerals*, 27:495–503, 2000.

[50] A. P. Dhupe and A. N. Gokarn. Studies in the Thermal-Decomposition of Natural Siderites in the Presence of Air. *International Journal of Mineral Processing*, 28 (3-4):209–220, 1990.

[51] B. V. L'vov and V. L. Ugolkov. Peculiarities of $CaCO_3$, $SrCO_3$ and $BaCO_3$ decomposition in CO_2 as a proof of their primary dissociative evaporation. *Thermochimica Acta*, 410(1-2):47–55, 2004.

[52] Personal correspondence with Professor Tor Grande, NTNU, May 2011.

[53] Paul Heitjans and Jörg Kärger. *Diffusion in Condensed Matter: Methods, Materials, Models*. Springer-Verlag Berlin Heidelberg, Berlin, Heidelberg, 2005.

[54] R. Wiebe. The Binary System Carbon Dioxide-Water under Pressure. *Chemical Reviews*, 29(3):475–481, 1941.

[55] Geir Watterud. *Determination of oxygen transport coefficients in perovskites and perovskite related materials with mixed conductivity*. PhD thesis, Norwegian University of Science and Technology, 2005.

[56] Matthijs Willem den Otter. *Oxygen transport in mixed conductiong oxides using isotopic exchange and conductivity relaxation*. PhD thesis, University of Enschede, 2000.

[57] I. Yasuda and T. Hikita. Precise Determination of the Chemical Diffusion-Coefficient of Calcium-Doped Lanthanum Chromites by Means of Electrical-Conductivity Relaxation. *Journal Of The Electrochemical Society*, 141(5):1268–1273, 1994.

[58] Ferdinand A. Kröger. *The chemistry of imperfect crystals*. Nort-Holland, Amsterdam, 1973.

[59] I. Waernhus, K. Wiik, and T. Grande. Oxygen transport in $LaFeO_3$. *Euro Ceramics Vii, Pt 1-3*, 206-2:1221, 2002.

[60] Nils Wagner. Synthesis and Characterization of $La_{0.2}Sr_{0.8}Fe_{0.8}Ta_{0.2}O_{3-\delta}$ as Membrane Material for Oxygen and Syngas Production. Bachelor thesis, 2010.

[61] Scanning Probe Image Processor, SPIP™. *version 5.1.6*. Image Metrology A/S, Hørsholm, Denmark, 2011.

[62] ISO 5017:1998(E). *Dense shaped refractory products - Determination of bulk density, apparent porosity and true porosity*. ISO, Geneva, Switzerland.

[63] MATLAB®. *version 7.11.0.584 (R2010b)*. The MathWorks Inc.™, Natick, Massachusetts, 2010.

[64] M. Thomasen. *Program for calculating diffusion and sirface exchange coefficients from conductivity relaxation data*. 2005.

[65] G. Natta and E. Casazza. Crystal and atomic structure of ferrohydrate. *Atti della Accademia Nazionale dei Lincei. Classe di Scienze Fisiche, Matematiche e Naturali. Rendiconti Lincei*, 5:803, 1927.

[66] P. D. Battle, T. C. Gibb, and S. Nixon. A Study of the Ordering of Oxygen Vacancies in the Rare-Earth Perovskites $Sr_2MFe_3O_{8+y}$ by Mössbauer-Spectroscopy. *Journal of Solid State Chemistry*, 79(1):86, 1989.

[67] K. Kimura, M. Ohgaki, K. Tanaka, H. Morikawa, and F. Marumo. Study of the Bipyramidal Site in Magnetoplumbite-Like Compounds, $SrAl_{12}O_{19}$, $SrFe_{12}O_{19}$, $SrGa_{12}O_{19}$. *Journal of Solid State Chemistry*, 87(1):186, 1990.

[68] V. I. Khitrova, Klechkov.Vv, and Z. G. Pinsker. Electron-Diffraction Study of Tantalum Idoxide in Thin Films. *Soviet Physics Crystallography, Ussr*, 12(6):907, 1968.

[69] V. I. Khitrova and V. V. Klechkovskaya. Investigation by the Electron-Diffraction Method of Tetragonal Tantalum Oxides in Thin-Layers. *Kristallografiya*, 27(4): 736, 1982.

[70] ASME-B46.1-2002. *Surface Texture (Surface roughness, waviness and lay)*. The American Society of Mechanical Engineers, New York, USA.

[71] David R. Lide Jr., editor. *JANAF Thermochemical tables*. American Chemical Society and the American Institute of Physics, Michigan, USA, 3rd edition, 1985.

[72] Ihsan Barin and Gregor Platzki. *Thermochemical data of pure substances*. VCH, Weinheim, 1995.

Appendices

A Calculation of Surface Roughness and Specific Surface Area

The following calculations can be done to describe the surface roughness and specific surface area using as input the X, Y and Z coordinates obtained by an AFM.

Surface roughness Surface roughness average, S_a, can be calculated using Equation A.1 [70];

$$S_a = \sqrt{\frac{1}{MN}\sum_{k=0}^{M-1}\sum_{l=1}^{N-1}|z(x_k, y_l)|} \tag{A.1}$$

where M and N are the number of measuring points in X and Y direction. Equation A.1 is based on calculations of the "area root mean square slope" as defined elsewhere [70].

Specific surface area The specific surface area, S_{sa}, of the scanned sample can be calculated using Equation A.2 [70].

$$S_{sa} = \sum_{k=3}^{M-3}\sum_{l=3}^{N-3}\Delta^2(x_k, y_l) \tag{A.2}$$

where

$$\Delta^2(x_k, y_l) = \left(\left[\frac{A}{60\Delta x}\right]^2 + \left[\frac{B}{60\Delta x}\right]^2\right)^{1/2} \tag{A.3}$$

and

$$\begin{aligned} A = & \\ & -z(x_{k-3}, y_l) + 9z(x_{k-2}, y_l) - 45z(x_{k-1}, y_l) \\ & +45z(x_{k+1}, y_l) - 9z(x_{k+2}, y_l) + z(x_{k+3}, y_l) \\ B = & \\ & -z(x_k, y_{l-3}) + 9z(x_k, y_{l-2}) - 45z(x_k, y_{l-1}) \\ & +45z(x_k, y_{l+1}) - 9z(x_k, y_{l+2}) + z(x_k, y_{l+3}) \end{aligned}$$

B Thermodynamic Data for Phase Stability Calculations

Table B.1 shows thermodynamic data used for calculating the stability regions of SrO, $SrCO_3$ and $Sr(OH)_2$ in Section 2.6.

Table B.1: Thermodynamic data for $SrCO_3$ stability calculations

T [K]	$\delta G_{f,CO_2}$, [71] [kJ/mol]	$\delta G_{f,SrO}$, [71] [kJ/mol]	$\delta G_{f,SrCO_3}$ [72] [kJ/mol]	$\delta G_{f,H_2O}$, [71] [kJ/mol]	$\delta G_{f,Sr(OH)_2}$, [71] [kJ/mol]
800	-395.586	-511.419	-1004.753	-	-
900	-395.748	-501.664	-978.431	-	-
1000	-395.886	-491.977	-952.201	-	-
1100	-396.001	-482.006	-925.745	-	-
1200	-396.098	-471.690	-899.141	-181.425	-637.737
1300	-396.177	-461.376	-874.341	-175.774	-614.156
1400	-396.240	-451.070	-849.771	-170.089	-590.966

C Regression on k_{chem} Data Points from ECR-Experiments

Linear regression was done on $\log(k_{chem})$ data points for quantitative comparison of k_{chem}-values obtained with and without surface structuring. Table C.1 and Table C.2 show the slope, a, and intercept with y-axis, y_0, following Equation C.1, respectively.

$$y = y_0 + a \cdot x \tag{C.1}$$

Here, $x = \log(p_{O_2})$. The tables show regression values for both reduction and oxidation steps at T = 800°C and T = 900°C, including standard deviations, σ.

Table C.1: Slopes from linear regression of $\log(k_{chem})$ data points

Conditions		Etched surface		Polished surface	
T	Step	a	σ	a	σ
800°C	Red.	0.463	0.028	0.500	0.054
800°C	Ox.	0.601	0.014	0.584	0.022
900°C	Red.	0.232	0.075	0.398	0.025
900°C	Ox.	0.506	0.071	0.581	0.030

Table C.2: Y-axis intercepts from linear regression of $\log(k_{chem})$ data points

Conditions		**Etched surface**		**Polished surface**	
T	Step	y_0	σ	y_0	σ
800°C	Red.	-2.378	0.052	-2.809	0.108
800°C	Ox.	-2.407	0.023	-2.897	0.036
900°C	Red.	-1.960	0.152	-2.171	0.050
900°C	Ox.	-1.840	0.131	-2.023	0.051

Using Equation C.1 one can obtain a single value for $\log(k_{chem})$ at each p_{O_2} for the different temperatures and p_{O_2}-steps where $y = \log(k_{chem}^{calc})$. Table C.3 shows the calculated values. The improvement of k_{chem} resulting from the surface structuring is calculated using Equation 4.1.

Table C.3: Calculated values of log(k_{chem}) based on regression results

$\log(p_{O_2})$		-1.18		-1.70		-2.22		-2.70	
		$\log\left(k_{chem}^{calc}\right)$	σ	$\log\left(k_{chem}^{calc}\right)$	σ	$\log\left(k_{chem}^{calc}\right)$	σ	$\log\left(k_{chem}^{calc}\right)$	σ
Etched surface									
800°C	Red.	-2.92	0.04	-3.16	0.04	-3.41	0.03	-3.63	0.02
800°C	Ox.	-3.12	0.02	-3.43	0.01	-3.74	0.01	-4.03	0.00
900°C	Red.	-2.23	0.13	-2.35	0.12	-2.48	0.10	-2.59	0.09
900°C	Ox.	-2.44	0.11	-2.70	0.09	-2.96	0.08	-3.21	0.06
Polished surface									
800°C	Red.	-3.40	0.09	-3.66	0.08	-3.92	0.07	-4.16	0.06
800°C	Ox.	-3.59	0.03	-3.89	0.02	-4.19	0.01	-4.47	-
900°C	Red.	-2.64	0.04	-2.85	0.04	-3.06	0.03	-3.25	0.03
900°C	Ox.	-2.71	0.04	-3.01	0.03	-3.31	0.02	-3.59	0.01

The standard deviations of calculated values were estimated using Gauss rule for propagation of errors, Equation C.2,

$$\sigma^2 \approx \sum_{i=1}^{p} \left(\frac{\partial y}{\partial x_i} \cdot \sigma_{x_i} \right)^2 \tag{C.2}$$

where y denotes a function (i.e. Equation C.1), i denotes the different equation parameters (i.e. a, y_0 and x for Equation C.1) and σ_{x_i} denote the individual standard deviation of each equation parameter.

D Calculation of pH

pH is defined as the negative logarithm of the hydrogen ion concentraion [38];

$$\mathrm{pH} = -\log\left(\mathrm{C}_{\mathrm{H}^+}\right) \tag{D.1}$$

The strong acids and bases are assumed to be fully dissociated. This goes for HCl, HNO_3, H_2SO_4 and KOH. The weak acids need a more carefull approach for the calculations utilizing the equilibria conditions, mass balance (MB) of the solution and the electro neutrality condition (EN). The weak acids in question are $H_2C_2O_4$ and H_2CO_3. The approach for deciding C_{H^+} is shown below for the general diprotic acid H_2A where A^{2-} is the conjugated base.

Two equilibrium reactions need to be examined;

$$H_2A \rightleftharpoons HA^- + H^+ \tag{D.2}$$
$$HA^- \rightleftharpoons A^{2-} + H^+ \tag{D.3}$$

with their respective corresponding mass action equations;

$$K_{a1} = \frac{C_{HA^-}C_{H^+}}{C_{H_2A}} \tag{D.4}$$
$$K_{a2} = \frac{C_{A^{2-}}C_{H^+}}{C_{HA^-}} \tag{D.5}$$

This aqueous solution will have the following MB and EN;

$$MB: \quad C_a = C_{H_2A} + C_{HA^-} + C_{A^{2-}} \tag{D.6}$$
$$EN: \quad C_{HA^-} + 2C_{A^{2-}} + C_{OH^-} = C_{H^+} + C_c \tag{D.7}$$

where C_a denotes the dissolved concentration of acid, C_c denotes any additional cations introduced to the solution (as is the case for $NaHCO_3$) and $C_{OH^-} = 10^{-14}/C_{H^+}$. Rearranging Equation D.4 and Equation D.5 leaves;

$$C_{H_2A} = \frac{C_{HA^-}C_{H^+}}{K_1} \tag{D.8}$$
$$C_{A^{2-}} = \frac{K_2C_{HA^-}}{C_{H^+}} \tag{D.9}$$

These can be inserted into Equation D.6 which then can be solved to leave C_{HA^-} as a function of C_{H^+};

$$C_{HA^-} = \frac{C_a}{1 + \frac{C_{H^+}}{K_1} + \frac{K_2}{C_{H^+}}} \tag{D.10}$$

Inserting Equation D.10 into Equation D.8 and Equation D.9 makes it possible to express the electro neutrality condition with only C_{H^+} as an unknown, Equation D.11;

$$\frac{C_a}{1 + \frac{C_{H^+}}{K_1} + \frac{K_2}{C_{H^+}}} + \frac{2K_2C_a}{C_{H^+}\left(1 + \frac{C_{H^+}}{K_1} + \frac{K_2}{C_{H^+}}\right)} + \frac{10^{-14}}{C_{H^+}} = C_{H^+} + C_c \tag{D.11}$$

Equation D.11 can be used to calculate C_{H^+} and by using Equation D.1 the pH-values denoted in Table D.1 are calculated. The pK_a-values in this table is calculated using Equation D.1 by exchanging C_{H^+} with K_{a1} and K_{a2} for the respective etchants.

Table D.1: Calculated pH values for de different etchant solutions used. pKa-values taken from [33]

Etchant	pH	pK_{a1}	pK_{a2}
H_2SO_4	-1.57	-	-
HNO_3	-1.16	-	-
HCl	-1.07	-	-
$H_2C_2O_4$	0.65	1.25	3.81
$NaHCO_3$	8.34	6.35	10.33
Na_2CO_3	12.32	6.35	10.33
KOH	15.3	-	-

E Values of L_c

The values for L_c listed below in Table E.1 are calculated using Equation 2.2 at the temperatures and p_{O_2}-drops where both D_{chem} and k_{chem} could be determined. p_{O_2} I and p_{O_2} II refer to the partial pressure of oxygen before and after a relaxation is conducted, respectively. L_y and L_z is calculated using Equation 2.29. Not all relaxations are listed here, because for some it was not possible to determine both D_{chem} and k_{chem}.

Table E.1: L_c-values for surface structured ECR-sample

T, [°C]	p_{O_2} I	p_{O_2} II	L_c, [μm]	L_y	L_z
800	20.00%	6.60%	121	4	12
800	20.00%	6.60%	144	3	10
800	20.00%	6.60%	139	3	11
800	6.60%	2.00%	139	3	11
800	6.60%	2.00%	242	2	6
800	2.00%	0.60%	178	3	8
800	2.00%	0.60%	198	2	7
800	0.60%	0.20%	253	2	6
800	0.60%	0.20%	200	2	7
800	2.00%	6.60%	267	2	5
900	20.00%	6.60%	84	6	18
900	20.00%	6.60%	72	7	20
900	6.60%	2.00%	167	3	9
900	6.60%	2.00%	122	4	12
900	2.00%	6.60%	104	5	14
900	2.00%	6.60%	103	5	14
900	2.00%	0.60%	254	2	6
900	2.00%	0.60%	108	4	14
900	0.60%	0.20%	166	3	9
900	0.60%	0.20%	231	2	6
900	0.60%	2.00%	310	2	5
900	2.00%	6.60%	61	8	24